



UNIVERSITA' DEGLI STUDI DI PERUGIA

Dipartimento di Fisica e Geologia

Corso di Laurea Magistrale in Fisica

Tesi di Laurea Magistrale

**Anisotropy measurement in the
incoming direction of charged cosmic
rays with DAMPE experiment**

Candidato:

*Enrico
Catanzani*

Relatori:

*Dr. Matteo Duranti
Dr. Valerio Vagelli*

Anno Accademico 2017/2018

To my parents, always present...

Contents

Introduction	4
1 Physical background	8
1.1 General information on cosmic rays	10
1.2 Energy Density of Cosmic Rays	16
1.3 Fermi acceleration mechanisms	18
1.4 CR sources	21
1.4.1 Super Novae	21
1.4.2 Pulsar	23
1.5 Dark Matter	27
1.6 Positron fraction	31
1.6.1 Spectrum characteristics	31
2 Anisotropy of the incoming directions of charged cosmic rays	36
2.1 Confinement of cosmic rays	36
2.1.1 Electrons and positrons traveled distance	38
2.2 Isotropy and Anisotropy in cosmic rays	44
2.3 Possible sources of the positron excess	45
3 The DAMPE Detector	50
3.0.1 The Plastic Scintillation array Detector (PSD)	54
3.0.2 The Silicon-Tungsten tracKer-converter (STK)	56
3.0.3 The BGO calorimeter (BGO)	60
3.1 The NeUtron Detector (NUD)	62
3.2 Performing anisotropy measurements with DAMPE	64
4 Tools for the anisotropy study	66
4.1 Galactic and Geographic coordinate systems	67

4.2	The acceptance of the DAMPE experiment	69
4.3	Calculation of DAMPE exposure	74
4.4	Realization of reference maps	76
4.5	Multipole Analysis	79
4.6	Fit procedures	86
5	Simulation tests and detector sensitivity	92
5.1	Anisotropy injection techniques	92
5.2	Tests of the fit procedure	95
5.2.1	Flat map performances	96
5.2.2	Realistic absolute maps	104
5.2.3	Realistic relative maps	108
5.3	Sensitivity of DAMPE as function of energy and time	110
6	Conclusions	116
	Appendices	118
A	Fermi Acceleration Mechanism	120
A.0.1	Fermi Acceleration Mechanism I	120
A.0.2	Fermi Acceleration Mechanism II	122
B	Estimate of Cold Dark Matter coupling with barionic matter	128
C	GZK cutoff	134
D	BGO shower containment	136
E	ToyMC simulation of DAMPE's geometrical acceptance	138
F	Reference isotropic maps	142
F.1	<i>k-fixed</i> maps	142
F.2	<i>rate-based</i> map	145
G	Data Maps	146

Introduction

It is widely accepted that approximately 85% of the matter content of the Universe is made of non-baryonic matter, usually called Dark Matter (DM). Its existence is confirmed by the indirect effects of its gravitational interactions. Its nature, however, is not yet clear. It is probable that DM is mainly made of a form of matter that is not described by the Standard Model of particle physics as we know it, and cannot interact via the electromagnetic field. The search for DM is one of the most investigated and fields in particle physics. Physicist are searching for its production by interaction of high energy standard matter particle in accelerators, by looking for the faint signals of nuclear recoils in cryogenic underground experiments, and by searching indirect signatures of DM annihilation or decay in the flux of cosmic rays.

In cosmic rays, DM signatures could be hidden in the features of charged cosmic rays. Annihilation or decay of DM results in the production of a pair of matter-antimatter ordinary particles, resulting therefore in an excess of antimatter abundances with respect to what predicted by the standard model of cosmic ray origin, acceleration and propagation. To investigate this, cosmic ray detectors must be operated outside the atmosphere to identify the primary cosmic ray before its interaction with the atmosphere.

Among the many species of charged cosmic rays, electrons and positrons are unique, in the sense that the features in their fluxes can probe the properties of the galactic neighborhood. In the last 10 years, the cosmic ray detectors *PAMELA*, *Fermi-LAT* and *AMS-02* have discovered and precisely measured an increase in the cosmic ray positron fraction ($e^+/(e^+ + e^-)$), indicating an excess of positron with energies larger than 30 GeV with respect to what expected by the standard production of secondary positrons from the interactions of primary cosmic rays with the interstellar medium. This results clearly indicates an that an additional, primary source of electrons and positrons has to be postulated to explain this feature. Two classes of

sources have been mainly modeled by physicist as positrons sources: DM annihilation in the Galaxy and the presence of nearby astrophysical sources like localized pulsars or Super Novae Remnants can both be modeled to explain the positron excess. The analysis of the spectral properties of the positron fraction alone, however, cannot completely disentangle between the two hypotheses. An observable that could constrain the two classes of models is the anisotropy in the arrival direction of positrons and electrons. In their way from the source to the detector, the path of charged cosmic rays is randomized by the turbulent galactic magnetic field: this results in a local flux that, as of today, is measured to be isotropic for charged cosmic rays with energies below tenths of TeV. However, if few nearby, localized sources are producing primary electrons and positrons, a faint anisotropy could be measured in the arrival direction of such particles. On the contrary, production of e^+/e^- by DM annihilation or decay is not expected to induce any anisotropy, due to the homogeneous distribution of the DM particle density in the galactic neighborhood. Therefore, the measurement of any anisotropy in the arrival direction of electron and positron cosmic ray would a robust evidence that the origin of primary positrons is dominated by the production from nearby astrophysical sources. As of today, only upper limits in the anisotropy of the e^+/e^- fluxes have been set by the *PAMELA*, *Fermi-LAT* and *AMS-02*.

The cosmic ray detector *DAMPE* has been collecting cosmic rays in orbit since December 2015. *DAMPE* is a calorimetric detector whose main physics targets are the measurements of gamma rays, nuclei and of electrons and positrons. It features a thick, dense $31 X_0$ BGO calorimeter that provides excellent energy resolution and electromagnetic shower containment, resulting in powerful electron identification capabilities up to 10^5 .

DAMPE has already measured the fluxes of $(e^+ + e^-)$ up to 5 TeV with unprecedented accuracy in the direct determination of the flux features. The data collected so far may provide interesting information in the search for anisotropies in that channel. With respect to previous similar missions, in fact, *DAMPE* features an improved energy resolution and a better control of the hadronic background in the selected $(e^+ + e^-)$ sample. The result of the search for anisotropies in the *DAMPE* data, both in the form of a upper limit or a discovery, will provide fundamental information to the experimental scenario towards the identification of the source of the primary positrons in cosmic rays.

In this work, a technique based on a template-fit method to extract the anisotropy level from the *DAMPE* data has been developed.

In chapter 1, I provide an introduction to the physics of charged cosmic rays in the energy interval relevant for this topic.

In chapter 2, I discuss in detail the physics behind the propagation of charged cosmic rays and the state-of-the-art of the searches for anisotropies in the $e^+/-$ channel.

In chapter 3, I describe the *DAMPE* mission and the experiment detectors.

In chapter 4, I develop the technical tools that are needed for the measurement of the anisotropy, describing the methods to construct reference maps of isotropic and anisotropic skies using MonteCarlo methods taking into account the detector acceptance, livetime and exposure, and I introduce the mathematical framework to extract dipole components from the measured sky maps.

In chapter 5, I apply the procedure to measure the anisotropy in simulated maps with different levels of injected anisotropies to verify the methods developed in this thesis, and to confirm the reliability of the method for application on sky maps based on data collected by *DAMPE*. Finally, I provide the sensitivity limits of the *DAMPE* detector for the measurement of anisotropy in the $(e^+ + e^-)$ channel based on the statistics collected by the mission.

Chapter 1

Physical background

“ Physics is the science of all the tremendously powerful invisibilities - of magnetism, electricity, gravity, light, sound, cosmic rays. Physics is the science of the mysteries of the universe. How could anyone think it dull? ”

— Dick Francis (2004)

Universe has always been an unquenchable source of inspiration ever since man has memory, seen by some as a refuge and by many others as an intriguing and complex puzzle for which an unceasing feeling to solve it is felt. Extremely high energetic phenomena, thermonuclear reactions inside stellar cores, black holes, dark energy and matter, cosmic radiation and recently gravitational waves; all this, and much more, is part of the great, fascinating and at the same time tremendously mysterious ecosystem in which we all are trying to unravel ourselves, leading to the discovery of fascinating realities.

The study of the cosmic radiation is an incredibly powerful tool used to understand most of the mysterious phenomena; while we're here discussing, a rich and varied pull of particles with different species and energies has been released from some astrophysical source into the deep space, traveling through the interstellar medium, enriching the cosmic rays whose understanding is always a challenging activity for the astroparticle physicists. In that way we have the stunning opportunity to connect two completely opposite physics' fields: the tiny scale of elementary particles at 10^{-15} m with the gigantic realm of astrophysics up to 10^{22} m.

The history of the cosmic rays is as interesting as the information they carry;

all starts in 1912 with the famous *balloon flight* by Victor Hess, who could be considered as the pioneer for the modern space age.

In that period the real nature was completely unknown; from that moment on has been understood that the radiation measured at hearth were coming from space! Until the realization of accelerator facilities on ground, cosmic rays were the only source for particles from KeV to 10^{20} eV and this gave birth to a new field of physics; nowadays is infact known that the cosmic rays spectrum covers 13 orders of magnitude in energy and 32 in flux intensity.

The name *cosmic rays* has been assigned in 1925 by Millikan, thinking they were principally composed by gamma rays; even if our current knowledge on the argument states they represents less than 1% of the total, the name has been maintained for historical reasons.

The study of the cosmic particles allowed the discovery of many new ones, like the positron, the muon, the pion and all the iperons as Λ , Σ , Ξ , Ω and many others.

The arrival of the modern space age completely turned the situation upside down; the lunch of the *Sputnik-1* in 1957, quickly followed by many others missions, has been a milestone signing the coming a whole new era, of which we are now the heirs. At the present time our knowledge regarding the cosmic rays is far more complete, thanks to the development of new theoretical models and, principally, to the realization of amazing experiments, both on earth and in space. *AMS-01*, *AMS-02*, *PAMELA*, *Fermi* and *DAMPE* (on which we'll focus our attention) are just few stunning examples of the modern space experiments, together with enormous ground based observatory as *Pierre Auger Observatory* and *CTA* (in the next future), contributed, contribute and will contribute on the knowledge of cosmic rays.

It's necessary to remember that even though our enormous efforts and goals achieved our knowledge stops to the 4% of the whole universe, highlighting our deep ignorance and the long and winding road we still need to travel.

“ Look up at the stars and not down at your feet. Try to make sense of what you see, and wonder about what makes the universe exist. Be curious. ”

— Stephen Hawking

1.1 General information on cosmic rays

Cosmic rays fulfill the important role of messengers; they carry the information regarding astrophysical sources, crossed interstellar medium, galactic and extragalactic magnetic field, permitting to know and study what surrounds us. They're a continuous, stationary flux characterized by both particles (charged and not) and electromagnetic radiation; protons are extremely abundant representing 85% of the whole, together with Helium nuclei (12%), heavier ones (1%) and electrons (1%), while the other species are just few % of the total.

A characteristic feature of the cosmic rays is their spectrum; measured by many different experiments on both space and hearth it has the typical shape of a *broken power law*, with at least 2 slope changes:

$$\frac{dN}{dE} \propto E^{-\alpha} \quad \alpha = \begin{cases} 2.7 & \text{if } E < 10^{15} \text{ eV,} \\ 3 & \text{if } 10^{15} \text{ eV} < E < 10^{18} \text{ eV} \end{cases} \quad (1.1)$$

Slope change is a sign that something's changing, at level of the sources; until the *knee* (10^{15} eV turning point) SNRs (*Super Nova Remnants*) provide enough energy to accelerate particle but from that point on a new type of astrophysical sources should be found, like AGN (*Active Galactic Nuclei*) or pulsars. A huge amount of resources and efforts are spent to build up all the theoretic framework at the base of the particle acceleration and propagation through the interstellar medium; it so clear that the identification of the right source of cosmic rays is critical; this will affect the acceleration mechanism and, at the end, the final spectrum that should match with the experimental measurements. A description of both the sources and particles' acceleration mechanisms will be provided in the following sections of this chapters.

Another important point that may be worth raising is is the following: *have the cosmic rays the same origin of the Solar System constituents?*

The answer to this question is not as easy as it seems; a good starting might be the analysis of the elements abundances, technique that permits a direct comparison between the results. Some discrepancies and interesting behaviors have been observed:

- *Li, Be, B* are produced as transitions elements into stellar nucleosynthesis and so are not abundant in the Solar System; on the contrary they are

particularly present in the cosmic rays thanks to spallation processes of heavier nuclei;

- Iron is abundant into the cosmic rays even if its cross section for spallation processes is high, like 764 mb ; this unexpected and strange behavior is known as *Iron problem* and could be solved, as we would like to mention, introducing a *path-length* distribution for that element;
- elements with an *even* number of nucleons are principally produced by stellar nucleosynthesis, and so more present into the Solar System respect to the cosmic rays, which, at the contrary, principally generate elements with an *odd* number of nucleons.

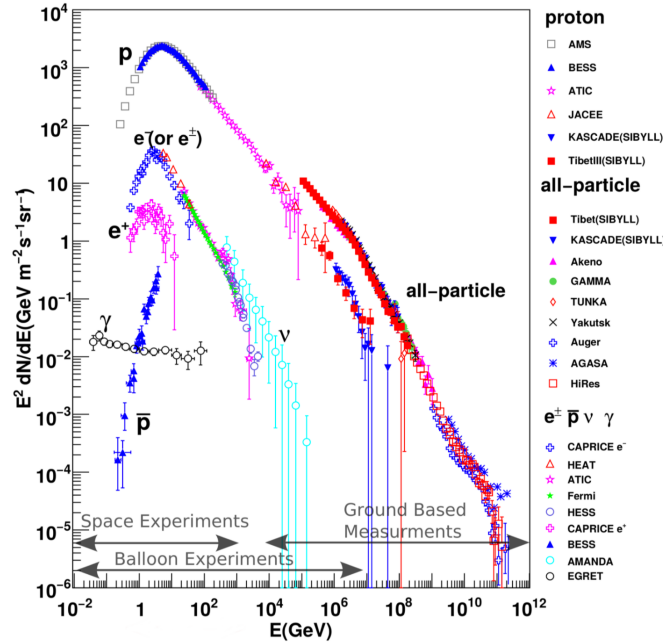


Figure 1.1: Spectrum of cosmic rays; in this picture different energy ranges for space, balloon and ground based experiments have been highlighted, together with the contribution of each experiment [1]. The spectrum has been multiplied by E^2 to make slope changes more evident. Note that, as seen before, protons are really abundant, while electrons, positrons and photons represents just few percents.

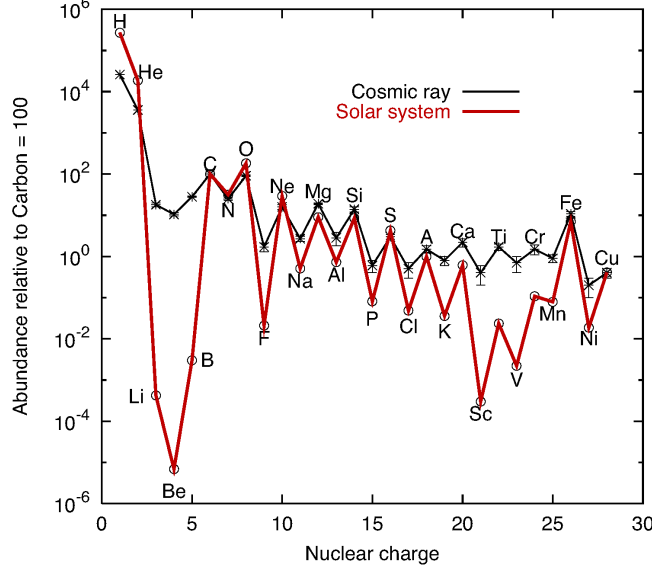


Figure 1.2: Comparison of the nuclear relative abundances between cosmic rays and Solar System.

In figure 1.2 a *zig-zag* pattern is evident; typical of nuclear physics this particular behavior is due to the higher binding energy of elements with an even number of nucleons.

As mentioned before, spallation process is fundamental to justify not only the abundances of the cosmic rays, but also the interstellar medium crossed during their propagation. All these information could be obtained considering a simple propagation model known as *Slab Model* where all the elements are supposed to go through the same quantity of material; labeling as N_M and N_L the number of heavy and light elements respectively, λ_M and λ_L the corresponding interaction lengths and P_{ML} the probability of the spallation process, is possible to evaluate how the number of elements changes respect to the grammage:

$$\begin{aligned} \frac{dN_M(\xi)}{d\xi} &= -\frac{N_M(\xi)}{\lambda_M} \\ \frac{dN_L(\xi)}{d\xi} &= \frac{P_{ML}}{\lambda_M} N_M(\xi) - \frac{N_L(\xi)}{\lambda_L} \end{aligned} \quad (1.2)$$

The equation system 1.2 states a simple but important phenomenon: heavy elements generate, by spallation processes, lighter ones, who themselves do the same. The solution is easily obtained as:

$$N_M(\xi) = N_M^0 e^{-\xi/\lambda_M}$$

$$N_L(\xi) = \left(\frac{P_{ML}}{\lambda_M} N_M^0 \right) \left(\frac{\lambda_M \lambda_L}{\lambda_L - \lambda_M} \right) (e^{-\xi/\lambda_L} - e^{-\xi/\lambda_M}) \quad (1.3)$$

Information regarding crossed grammage ξ could be easily obtained studying N_L/N_M ratio (for example a particularly interesting and useful choice for the elements could be B/C); to match with the experimental value measured on Earth cosmic rays have to travel through the galaxy for a thickness of equivalent material like 4.8 g cm^{-2} . Since our planet has not a favorite position into the Milky Way, any other observer could be able to measure the same value.

From the equation system 1.3 is obvious that bigger is the spallation cross section for a such element and less abundant it will became; in this way we would expect a strong suppression for the abundance of iron, even if this is not what has been experimentally observed (as figure 1.2 reports). The *Iron's problem* could be solved introducing a distribution of path lengths into the slab model; Fe elements, instead of crossing the same quantity of equivalent material ξ just go through a part of it, maybe a third. This modification not only permits to reproduce the observed abundance for Fe , but also to explain those of *sub-Fe* elements.

Analyzing more in detail the ratio N_L/N_M , as could be the case of B/C , a certain energy dependence has been observed; this unexpected behavior could be reproduced slightly modifying the equation system 1.2 introducing a grammage energy dependence $\xi_e(E)$:

$$\frac{N_L}{N_M} = \frac{P_{ML}/\xi_M}{1/\xi_e + 1/\xi_M}$$

$$\frac{N_L}{N_M} \approx \begin{cases} \frac{P_{ML}\xi_e(E)}{\xi_M} & \text{if } \xi_L \gg \xi_e, \\ P_{ML} \frac{\xi_L}{\xi_M} & \text{if } \xi_e \gg \xi_L \end{cases} \quad (1.4)$$

At high values of particles' rigidities, where $\xi_L \gg \xi_e$ is satisfied, the ratio N_L/N_M shown by equation 1.4 collapses to zero and the escape probability of the cosmic rays depends on their rigidity through a spectral index δ , whose

value is -0.6 (its uncertainty is high and the absolute value could range from 0.15 to 0.8 depending on the diffusion model chosen).

In case of low energy, the inequality to consider is $\xi_e \gg \xi_L$ and, in absence of other processes, we could expect a flat ratio; this does not occur in reality due to the *reacceleration of the low energy nuclei* by moving clouds of magnetized plasma present in the interstellar medium (Fermi's mechanism of the second order is at the base of this process).

Returning now on a more general description, is possible to affirm that the nature offers a very energetic beam, without providing its parameters; to get the whole picture precisely measurements of the entire cosmic rays flux (photons included) are needed. Reaching this ambitious goal could not be possible without a strong link and cohesion with the entire wide theoretical framework; for example a reliable propagation model is needed for accurate background evaluation for faint signal searches in CR, of critical importance, for example, for dark matter studies.

Many of the performed measurements, in term of ratios, could be really useful to distinguish between models:

- between primary particles (e.g. C/O) to fix source abundances;
- between primary and secondary ones (e.g. B/C) obtaining the crossed grammage, constraining the diffusion coefficient and the halo thickness;
- between radioactive isotopes (e.g. $^{10}Be/{}^9Be$) to get information on the escape times.

We will focus our attention on the electromagnetic component of the cosmic rays; these particles, even if particularly less abundant respect to the other species, are exceptionally precious due to the fact that electrons and positrons are able to provide information about the *local* sources and acceleration sites. Electrons and positrons have an extremely small mass compared to the other, which guarantees a faster and easier cooling through the emission of electromagnetic radiation. *Inverse Compton, ionization, synchrotron* and *bremsstrahlung* are the involved physical processes which all have a common characteristic: their cross section is inversely proportional to the square of the emitting particle's mass.

As we just said in the introduction, among all the carried information these light particles permit to investigate possible local sources of anisotropy in their incoming directions, revealing important details regarding our surrounding.

In the next sections of this chapter some of the characteristics of the cosmic rays met so far will be more precisely described, together with all the phenomena regarding them; we will analyse particles acceleration mechanisms and possible astrophysical sources as function of the beam energy, cosmic rays diffusion processes by *non-collisional* scattering with magnetic field irregularities and the active cooling mechanisms, especially active on lighter particles. Ample space will be dedicated to the anisotropy study of the cosmic ray incoming directions, introducing the concept on both theoretical and experimental point of view and describing the *actual state of the art* analyzing the available experimental results.

As may have emerged from this brief description, astroparticle physics is extremely wide, constantly and rapidly changing, which makes it one of the most interesting and challenging branches of the physics, on both experimental and theoretical point of view.

1.2 Energy Density of Cosmic Rays

In the previous pages the flux of the cosmic rays has been analyzed: a broken power law with, at least, two slope changes (equation 1.1). From that important physical quantity is possible to obtain the numerical density of CRs:

$$N_{CR} = 4\pi \frac{\Phi(> E_0)}{c} \text{ (cm}^{-3}\text{)} \quad (1.5)$$

In the previous equation $\Phi(> E_0)$ represents the integrated flux of the particles from a starting energy E_0 ; not considering solar wind contributions, this value is locked at 1 GeV.

$$\begin{aligned} \Phi(> 1 \text{ GeV}) &= \int_1^{10^6} \phi(E) dE = \frac{k}{\gamma - 1} \left[E^{-\gamma+1} \right]_{10^6 \text{ GeV}}^{1 \text{ GeV}} \\ &= 1 \text{ (cm}^{-2}\text{s}^{-1}\text{sr}^{-1}\text{)} \end{aligned} \quad (1.6)$$

Writing equation 1.6, k and γ are the parameters used to describe the flux of the cosmic rays: $\Phi = kE^{-\gamma}$. In the energy range considered, the values for these parameters are the following: $k = 1.8$ and $\gamma = 2.7$. Inserting the value already calculated into equation 1.5 we obtain a numerical density value or $N_{CR} = 4 \cdot 10^{-10} \text{ (cm}^{-3}\text{)}$. The energy density could be easily obtained integrating in energy the numerical one, as follows:

$$\begin{aligned} w_{CR} &= \int_0^\infty E n(E) dE = \int_0^\infty E \left(\frac{4\pi}{c} k E^{-\gamma} \right) dE \\ &= \frac{4\pi}{c} \frac{k}{\gamma - 2} \left[E^{-\gamma+2} \right]_{3 \cdot 10^6 \text{ GeV}}^{1 \text{ GeV}} \cong 1 \text{ eV/cm}^3 \end{aligned} \quad (1.7)$$

We have to compare this value with other typical energy densities, understanding how important the energetic of the cosmic ray is respect to the whole balance:

- **magnetic field**, considering a galactic magnetic field of $3 \cdot 10^{-6} \text{ G}$:

$$w_B = \frac{1}{8\pi} B^2 = 0.2 \text{ eV/cm}^3 \quad (1.8)$$

- ***Cosmic Microwave Background***, the electromagnetic radiation born together with the *Big Bang*, whose important effects on cosmic rays will be investigated later, has a density of 400 photons/cm³ and considering its black-body spectrum with a temperature of 3K we could found the corresponding energy density:

$$w_{CMB} = n_{CMB}K_B T = 0.2 \text{ eV/cm}^3 \quad (1.9)$$

- ***starlight***, obtained from photo-metric measurements:

$$w_{SL} = 10^{-2} \text{ eV/cm}^3 \quad (1.10)$$

Analyzing the previous results is thus obvious that the energy density of the cosmic rays represents an important part and should be absolutely considered into the whole galactic energetic.

1.3 Fermi acceleration mechanisms

Particle acceleration mechanism is one of the most interesting and fundamental aspect of the theory regarding cosmic rays; studying these processes we should be able to reproduce measured particle spectrum, their energy up to 10^{20} eV and chemical composition.

Due to the high temperatures of the astrophysical sources of the cosmic rays, most of the atoms are completely ionized and the whole system of particle could be described as a *plasma*; this is particularly true for H and He, which represent the most part cosmic matter, since their ionization potentials are quite low.

This matter aggregation status, commonly strongly aloof from every day life, is the most common in space representing 99% of the whole present material; is thus clear that its study and characterization is particularly important and useful. Speaking of cosmic rays, especially in case of acceleration, we have therefore to describe a plasma; while electric fields are not important over distances bigger than the Debye length due to electronic screening, only magnetic fields could be able to influence all fluid characteristics and behavior.

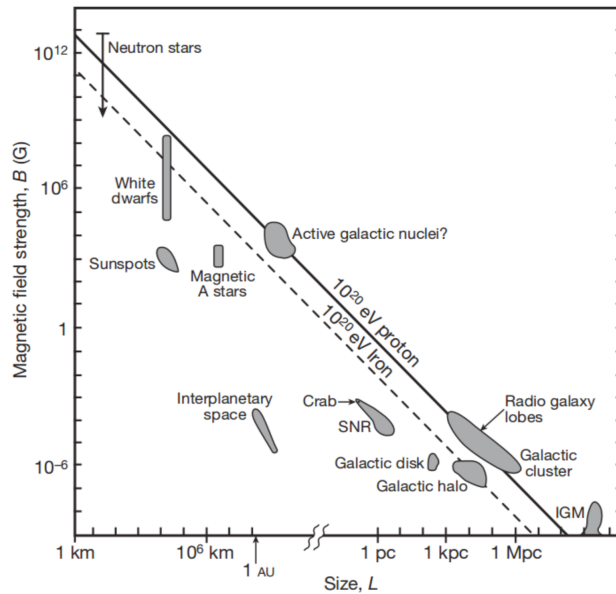


Figure 1.3: The Hillas plot [1], linking the dimensions of an astrophysical source with the intensity of its magnetic field.

The graph shown in figure 1.3, known as Hillas plot, highlights the correlation between magnetic field strength and astrophysical source dimension, asserting that in case of small sources magnetic field's intensity should be high and the other way around.

$$\underbrace{Ze\beta cB}_{\text{Lorentz force}} = \frac{m\gamma\beta^2 c^2}{\underbrace{L}_{\text{centripetal force}}} \Rightarrow E_{max} \approx ZeBcL\beta \quad (1.11)$$

The Hillas plot is based on the simple assumption that the accelerated particle has to be confined within the magnetic field of the accelerator; under this hypothesis the maximum particles' energy could be easily obtained, equating Lorentz and centripetal force as shown by equation 1.11 (here B , L , Ze represent respectively magnetic field intensity, source size, and particle charge, while $\beta \approx 1$). Following this picture only objects with a gigantic size and/or a huge magnetic field strength could accelerate particles up to the ultra high energies of above 10^{20} eV as measured in the CR. All our considerations have not included any kind of energy loss, particularly important for light particles, as just explained.

The particle acceleration mechanisms could be addressed as direct or stochastic processes; in the first case they're particularly rapid and occur in exceptional dense zones where radiative losses become important and have to be considered, while the second ones are based on continuously and gradual energy gains. Fermi's acceleration mechanisms, that we're now going to describe [2,3], belong to the second class and are based on successive crossings through inhomogeneities of magnetic fields, randomly moving into the interstellar medium; this kind of processes, although not particularly fast, permit to reach extremely high energy obtaining a spectrum very similar to the observed one.

Considering an energy gain ξ in each scattering process with the magnetic inhomogeneities, assuming E_0 the particles initial energy and k the number of collisions, the final energy may be written as $E_k = E_0(1 + \xi)^k$.

Being P the escape probability for a single particle from the inhomogeneity, after k scattering processes we can write:

$$P_k = \underbrace{(1 - P) \cdot (1 - P) \dots (1 - P)}_{\text{k-times}} P = P(1 - P)^k \quad (1.12)$$

Knowing the number of escaping particle $n_k = N_0 P_k$ is finally possible to easily obtain the differential energy spectrum:

$$n_k = N_0 P \left(\frac{E_k}{E_0} \right)^{\frac{\ln(1-P)}{\ln(1+\xi)}} \quad (1.13)$$

$$\frac{dn}{dE} \simeq \frac{n(E_k)}{\Delta E_k} \propto \frac{n(E_k)}{E_k} \propto E^{\frac{\ln(1-P)}{\ln(1+\xi)} - 1} = E^{-\gamma}$$

Obtained the differential spectrum, we'd ask our self what will be the maximum reachable energy for the particles; considering the whole process has a finite time to happen, that will be also the final energy. After a certain time t passed, and knowing the duration τ_{cycle} of each cycle involved in the process, maximum energy could be written as follows:

$$E_{max} < E_0(1 + \xi)^{t/\tau_{cycle}} \quad (1.14)$$

Fermi developed two independent models for CR acceleration, both based on these general assumptions: the first and second type acceleration mechanisms.

Mechanism I results particularly inefficient, except for particle with extremely high initial energy, being the mean energy gain proportional to the β^2 of the accelerated particle¹.

The second acceleration model proposed by Fermi increased its efficiency (in this case the mean energy gain results directly proportional to the Lorentz factor) and is capable to describe the measured particles' spectrum:

$$dn(E) \propto E^{-2} dE \quad (1.15)$$

More detailed calculus and information may be found in appendix A.

¹As reported in appendix A, fermi acceleration mechanisms consider particles as classic, $\beta \sim 0$

1.4 CR sources

Cosmic rays sources are extremely powerful astrophysics objects; up to *knee* energies both *Super Novae* and *pulsars* fulfill the role of acceleration sites. Based on different physical mechanisms, they contribute to the observed power spectrum.

The evaluation of the crossed grammage ξ , using the *slab model* (equation 1.3), permits to obtain the residence time τ of cosmic rays inside the galaxy; completely ignoring any kind of radiative loss, that value is of the order of 10^7 years. Once τ is known, together with the galactic volume V_G and the density energy of cosmic rays $w_{CR} \simeq 1 \text{ eV/cm}^3$, the power needed to maintain a stationary status can be evaluated: 10^{41} erg/s . Ordinary stars are not sufficient to explain a such result, also considering solar flares; integrating their whole power we obtain 10^{35} erg/s , many order of magnitude away.

We will now briefly describe all possible CR sources, highlighting the physical mechanism and considering the corresponding energy window.

1.4.1 Super Novae

A Super Novae is an extremely interesting and important source, particularly fascinating for its violent explosive energy releasing mechanism, covering many order of magnitude of the cosmic rays' spectrum.

These sources could be classified as:

- *type Ia*, whose mechanism is the explosive carbon burning in a mass-accreting white dwarf;
- *type Ib-Ic* and *type II*, releasing energy by core collapse of massive star.

The acceleration mechanism of the particles is based on shocks (Fermi second type A); the system could be physically described as a *blast wave*, a shock wave formed by an hot gas bubble expanding supersonically in the ambient medium. The typical observed expansion speed of a supernova remnant is $\sim 10^4 \text{ km/s}$, while the sound speed in the ISM ranges $10 - 100 \text{ km/s}$; this way the shock will form at the outer edge of the bubble (which acts as a supersonic piston).

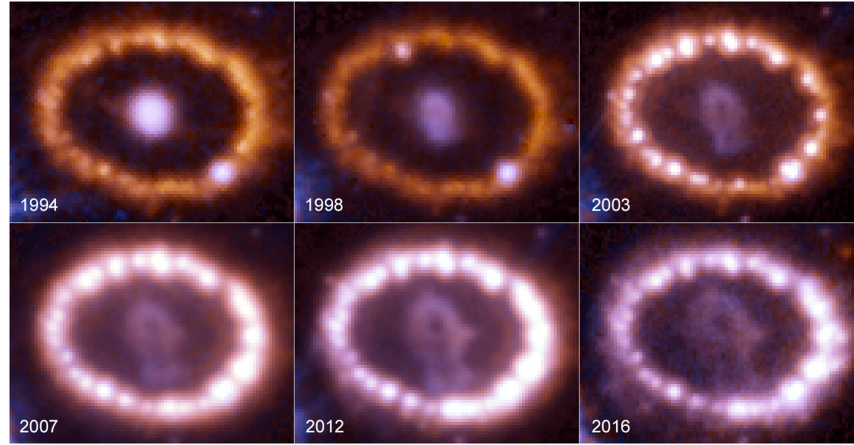


Figure 1.4: SN blast wave shock hits inner ring

In figure 1.4 we could see the blast wave shock hitting inner ring at 20,000 km/s, lighting up knots of shocked, compressed and heated material, 160 billion km wide.

The energetic study is done on SN of type *Ib*, *Ic* and *II*, considering the collapse of a massive core:

$$E = \frac{GM_{core}^2}{r_{NS}} - \frac{GM_{core}^2}{r_{before\ collapse}} > 10^{51} \text{erg} \quad (1.16)$$

Only 1% of energy goes in kinetic energy of the particles, the remaining part is transferred to neutrinos and photons, respectively 99% and 0.01%. SN explosions are extremely energetic phenomena, whose luminosity could hide the host galaxy too; this gives you an idea of the total released energy during the process, considering how it's distributed.

Released power by a Super Novae explosion could be evaluated considering the following arguments:

- each explosive process releases an energy $E \sim 10^{51}$ erg;
- an estimate of their frequency, in our galaxy, is easily obtained:

$$f_{SN} = \frac{1}{\tau_{SN}} = \frac{1}{30} \text{y}^{-1} \quad (1.17)$$

- this could be considered practically as a continuous process, considering CR escaping times of 10^7 years;
- power is thus finally evaluated:

$$W_{SN} = \frac{10^{51} \text{erg}}{30 \cdot 3.1510^7 \text{s}} \cong 10^{42} \text{erg/s} \quad (1.18)$$

- Considering the power needed to maintain a CR stationary status before obtained, what we need is a process capable to transfer to particles at least 10% if the whole energy released; this is exactly type II Fermi's mechanism.

SN are responsible for the cosmic ray spectrum up to 10^{15} eV, covering so many orders of magnitude; as we just said they are important astrophysical sources, whose study permits to investigate many features of CR and astroparticle physics in general.

1.4.2 Pulsar

Pulsars are fast rotating neutron stars, with an extremely intense magnetic field capable to accelerate particles up to 10^{19} eV, so covering the most energetic part of the cosmic ray spectrum. These sources originate from heavy cores of death stars; when the internal energy due to thermonuclear reactions is no more present, external pressure due to gravitational force cannot be opposed and the stellar core starts to collapse. In this situation, contrary to what could be imagined, stationary equilibrium status can still be found at the degeneracy pressure of neutrons, whose β -decays no more happen.

$$n \rightarrow p + e^- + \bar{\nu}_e \quad (1.19)$$

Because of Pauli's exclusion principle the process represented by equation 1.19, in case of extremely high pressure, could no more happen and a dense neutron core represents so a stable configuration. In case of core's mass bigger than M_{\odot} there is no possibility to balance the external pressure, final status could be nothing else than a black hole.

We're going to obtain pulsar's maximum emission energy, showing how the electromagnetic induction, that's the physical mechanism powering up this astrophysical source, could be used to reach the scope. We could start applying the Gauss theorem before and after the stellar collapse, obtaining the magnetic field B_{NS} of the neutron star:

$$B_{NS} = B \left(\frac{R}{R_{NS}} \right) \cong 10^{-2} \text{T} \cdot 10^{10} = 10^8 \text{T} \quad (1.20)$$

Rotational angular velocity ω_{NS} is easily obtained equating gravitational and centripetal acceleration:

$$\frac{GM^2}{R^2} = M\omega_{NS}^2 R \rightarrow \omega_{NS} \approx 10^3 - 10^4 \text{s}^{-1} \quad (1.21)$$

Pulsars have a mass similar to the solar one, $1.5 M_{\odot}$, concentrated in a radius ranging from 10 to 15 Km, which gives an idea of how high the density should be. Inserting these parameters, together with the typical magnetic field and radius of a pre-collapse star, into equation 1.20 we obtain a period that's in the range of milliseconds and a magnetic field strength of order 10^8 T, due to the conservation of angular momentum and magnetic flux of the original star.

The energy production mechanism, as we just said, is the electromagnetic induction; using Maxwell's equation regarding Faraday law, the induced electrical field ϵ onto a linear region L could be easily obtained as follows:

$$\begin{aligned} \nabla \times \epsilon &= -\frac{1}{c} \frac{\partial B}{\partial t} \rightarrow \frac{\epsilon}{L} = \frac{B\omega}{c} \\ \epsilon &= \frac{LB\omega}{c} \end{aligned} \quad (1.22)$$

Equation 1.22 highlights an important concept: differently from the other astrophysical sources studied, in this case the energy for particle acceleration comes from an electric field.

We could finally write the maximum energy E_{max} for a particle of charge Ze :

$$E_{max} = \int Ze \cdot \epsilon \cdot dx = \frac{ZeB\omega L^2}{c} \quad (1.23)$$

Equation 1.22 is particularly important and, inserting all the values before obtained, a good estimate for the maximum energy is $E_{max} = 10^{19}$ eV; pulsars could so be considered extremely powerful astrophysical sources for cosmic rays, interesting the most energetic and experimentally challenging part of their spectrum, the region above the *knee*.

The electromagnetic radiation emitted by the pulsars is not isotropic into the surrounding space but, at the contrary, concentrated into a narrow cone; whenever this one hits earth we see a pulse similar to the light of a lighthouse. Studying this particular physical system has been understood that the misalignment between rotation and spinning magnetic axis generates, as shown in figure 1.5, an accelerated magnetic dipole moment which radiates (in complete analogy to an electric dipole) electromagnetic radiation causing an energy loss of:

$$-\left(\frac{dE}{dt}\right) = \frac{\mu_0 \Omega^4 p_{m\perp}^2}{6\pi c^3} \quad (1.24)$$

Within equation 1.24 Ω denotes the angular velocity, μ_0 the vacuum permeability and $p_{m\perp}$ the magnetic moment perpendicular to the rotational axis. The necessary energy, spent emitting electromagnetic radiation and acceleration particles, is provided by a loss in the rotational energy which results in an observed increase of the rotation period P of the pulsar.

While the *magnetic dipole* model explains where the energy for particle acceleration comes from, it does not state the actual mechanism, *Goldreich-Julian* model fills this gap; the neutron star, and the pulsar too, is seen as a perfect conductor so that any induced electric fields inside the star with radius R will be canceled out by charges flowing around without resistance resulting:

$$\vec{E}_{in} + \underbrace{[(\Omega \times R) \times \vec{B}_{in}]}_{\text{induced field}} = 0 \quad (1.25)$$

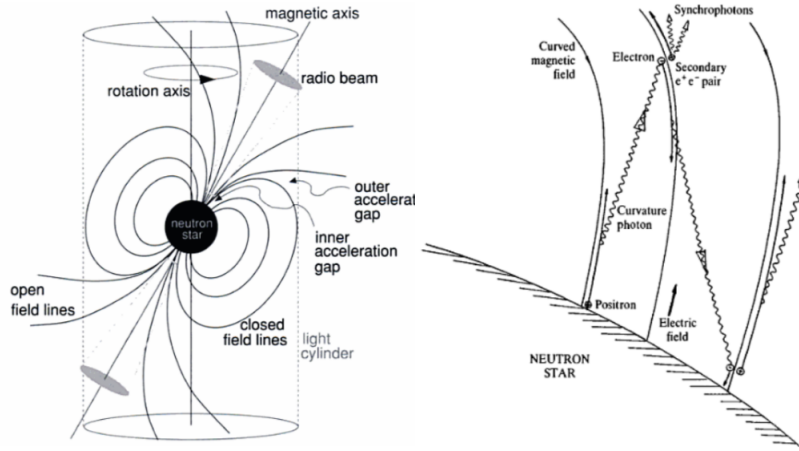


Figure 1.5: **(left)** a schematic representation of a misaligned pulsar. Here different possible emission regions of radiation are shown: the inner gap, where a strong magnetic field prevents high energy photon emission due to production of e^\pm pairs and the outer gap, more distant from the pulsar's surface, where the magnetic field is much smaller and could allow high energy emissions. **(right)** schematic view of a cascade generation in the pulsar's magnetic field causing photon and e^\pm emission/acceleration. Both the images have been taken from [1].

This approximation could be expanded to the pulsar magnetosphere in case of extremely high electric fields (up to 10^{12} V/m), whose could rip off charges from pulsar's surface and surround it with a fully conducting plasma. As seen in figure 1.5 particles could escape in case of open electric field lines and, at the same time, accelerated by them flowing along the curved magnetic field lines.

1.5 Dark Matter

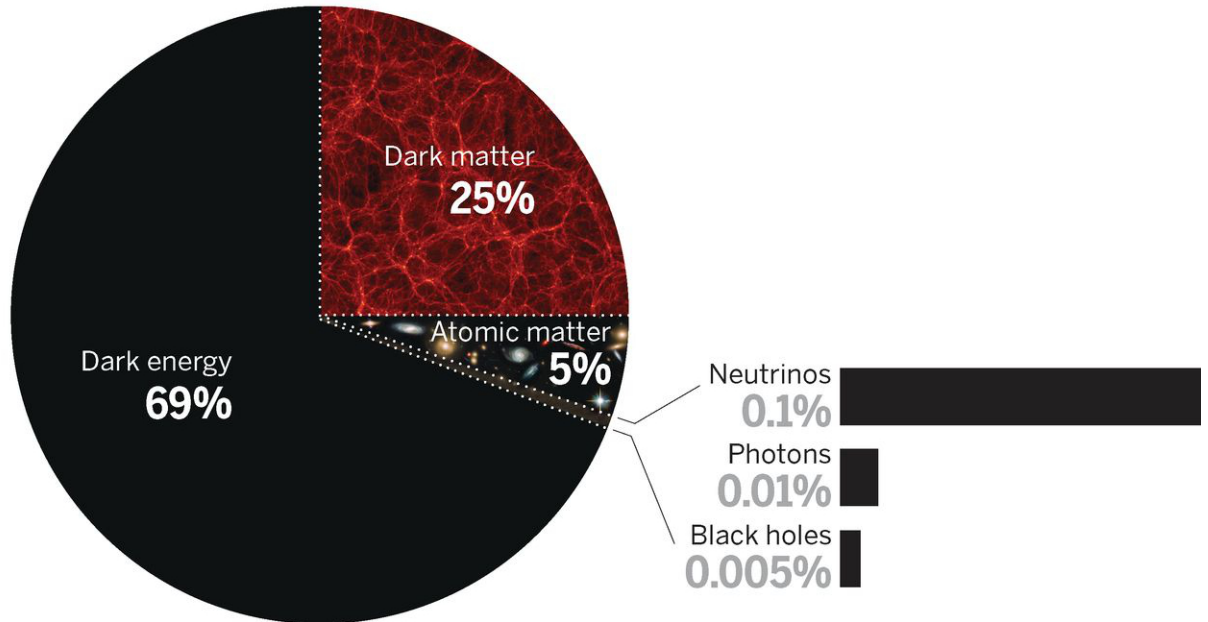


Figure 1.6: An effective sketch representing the energy content of the universe; the reader may notice that just few percent of the total is covered by barionic matter.

The Dark Matter (briefly DM) is characterized by *non barionic* matter, weakly interacting² (all the electromagnetic interactions should not be considered); this explains where its name comes from.

Figure 1.6 represents the energy content of the universe; the common barionic matter just covers few percent of the whole content, which is mainly divided between dark energy (DE) and cold dark matter³ (CDM). While for the DM particles there are several candidates and theoretic models, dark energy is, until now, an even deeper mystery.

Indirect proofs of the DM existence are known from many years, starting with the rotation speed of galaxies, the famous Bullet Cluster and arriving up to the gravitational lensing effects.

²See appendix B for the evaluation of the dark matter cross section.

³See appendix B for a more complete description of the dark matter.

Many different theoretical models of dark matter particles exist, but all of them need to satisfy some basic requirements: the particles need to be neutral⁴, particularly massive and weakly interactive⁵(candidate particles are commonly known as *WIMPs*, *Weakly Interactive Massive Particles*). One of the models that has been particularly investigated in the past years considers supersymmetric particles χ , known as neutralinos, with a characteristic mass of about 100 GeV and a cross section typical of the weak interactions.

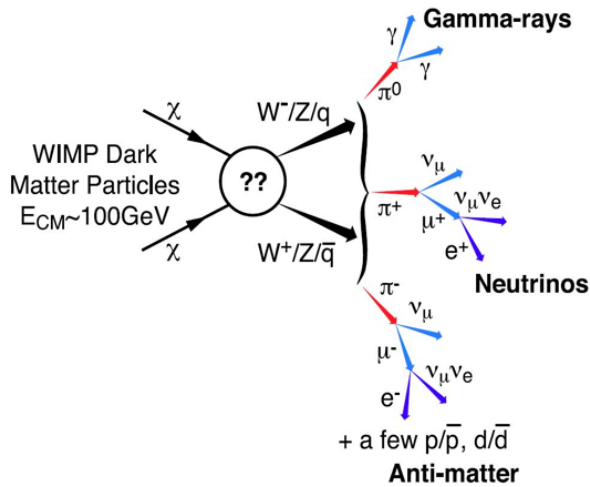


Figure 1.7: Illustration of possible dark matter annihilation channels. The detection of an excess or peak at the *neutralino* mass in those spectra would be a hint for WIMP dark matter.

Space experiments perform indirect research of DM, through the precise measurement of fluxes of photons and charged particles. As well explained in figure 1.7 the annihilation process of two DM particles (whatever their nature could be) produces barionic matter, like γ -rays, neutrinos⁶ and matter/anti-matter couples, whose fluxes could be measured by space experiments.

Dark matter, however, is not only investigated in indirect manners; physicists are trying to produce dark matter pairs through accelerating machines, like *LHC*, or highlight its presence by direct scattering experiments. Unfortunately both these investigation ways did not lead to conclusive results.

⁴Otherwise the electromagnetic cross section could not be ignored.

⁵See appendix B for more details.

⁶Neutrino detection is not possible with space experiments; it requires huge detection volumes (because of the cross section, typical of weak interactions), complex geometries for the detectors, ultra radio-pure materials.

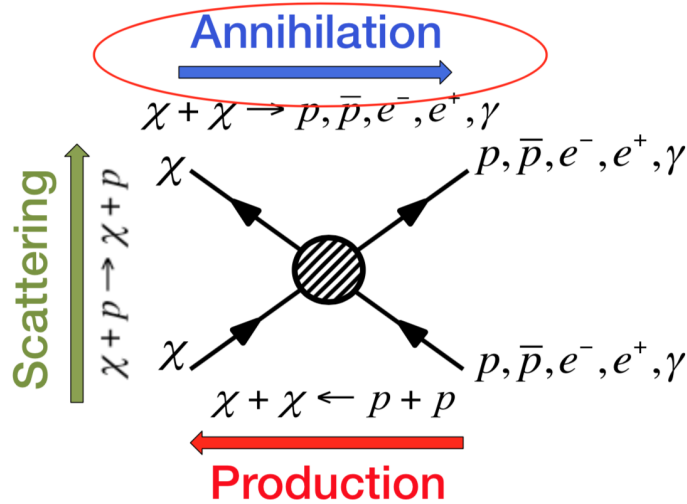


Figure 1.8: A very effective sketch showing all the pursued methods used to investigate DM. Indirect measurements exploit *annihilation channel*, accelerating machines the *production* one, while direct *scattering* experiment proceed vertically in the graph.

Dark Matter annihilation, or decay, is often invoked to explain open problems in cosmic ray physics, like the positron excess measured in the positron fraction (see section 1.6 for more details).

Signatures of dark matter activity in cosmic rays can be searched in many channels. For what regards charged CRs, since dark matter annihilation or decay produces a pair of particle plus antiparticle Standard Model matter (like p/\bar{p} , e^+/e^- and others), and considering that cosmic rays are dominated by matter particles (protons, helium, electrons, etc), physicist are searching for an overabundance of antimatter with respect to what expected by the production models. Typical searches are the channels of positrons, antiprotons, antideuterium and antihelium.

An evident excess has been found in the positron channel, as described in the next section. Measurements of antiproton fluxes are at the limit of compatibility with the expectation of a purely secondary antiproton production, as shown by the plot in figure 1.9.

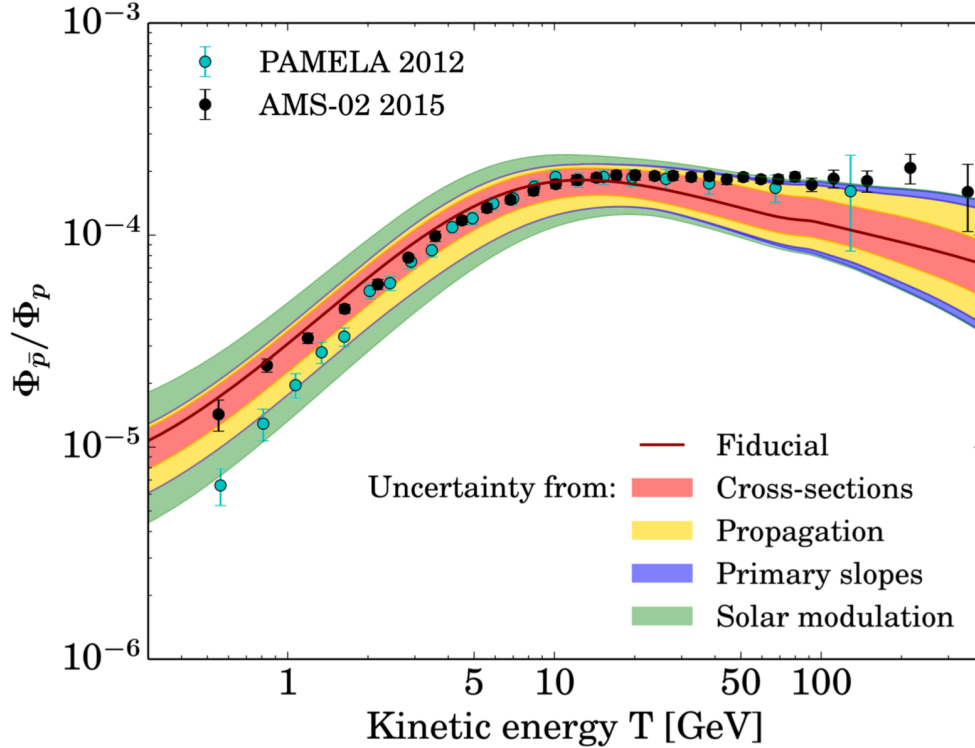


Figure 1.9: Antiproton measurements by *PAMELA* and *AMS-02* compared to the astrophysical prediction and its uncertainties [4].

Antideuterium and antihelium are instead considered the *smoking gun* for the indirect search of DM in CRs. No events of antideuteron or antinuclei has been found in CRs, and only upper limits in their flux has been set. The sensitivities of all this channels to the presence of DM activity are dictated by the level to which the production of antimatter by secondary processes of spallation of primary cosmic rays is known. In fact, the predictive power of such predictions is fixed by the finite knowledge of cosmic ray propagation mechanisms, by the knowledge of nuclear scattering and production cross sec-

tion at high energies, by the influence of the solar modulation for low energy cosmic rays and by the knowledge of the fluxes of the primary progenitors. All of these uncertainties can be and are being improved by complementary measurements of charged cosmic rays (like nuclear and isotopic abundances in cosmic rays), by the study of time dependent Solar effect on the low energy part of the fluxes, and by dedicated measurements at accelerators or fixed target experiments on ground.

1.6 Positron fraction

Many times we referred to the isotropy or anisotropy in the incoming directions of charged cosmic rays as a very promising study; the positron fraction, a very important measurement performed by *AMS-02*, permits to understand the physical applications of this research.

1.6.1 Spectrum characteristics

$$\psi = \frac{\phi_{e^+}}{\phi_{e^+} + \phi_{e^-}} \quad (1.26)$$

Equation 1.26 represent the definition of the positron fraction ψ , that's the positron flux respect to the *all electron* one (electrons and positrons)⁷.

Figure 1.10 shows different measures of positron fraction in function of energy by *Fermi*⁸, *PAMELA* and *AMS-02* [5]; in the latter case with the biggest accuracy, high statistics and wider energy range, defining new standards for space astroparticle measures.

This graph immediately highlights an unexpected behavior: starting from 10 GeV is present an hardening of the spectrum, meaning that other sources of positron should exist. Considering just propagation models the positron fraction is expected to decrease as function of the energy; expected values

⁷The usefulness of this definition is principally due to experimental reasons: having to measure the flux of two particles, dealing with a measurement ratio permits to cancel the contribution of systematical errors, similarly present at both numerator and denominator of the fraction.

⁸Differently from the other experiments, *Fermi-LAT* is not a magnetic spectrometer; Earth's magnetic field asymmetry, such as East-West effect, permits for certain positions of the detector to distinguish between electrons and positrons.

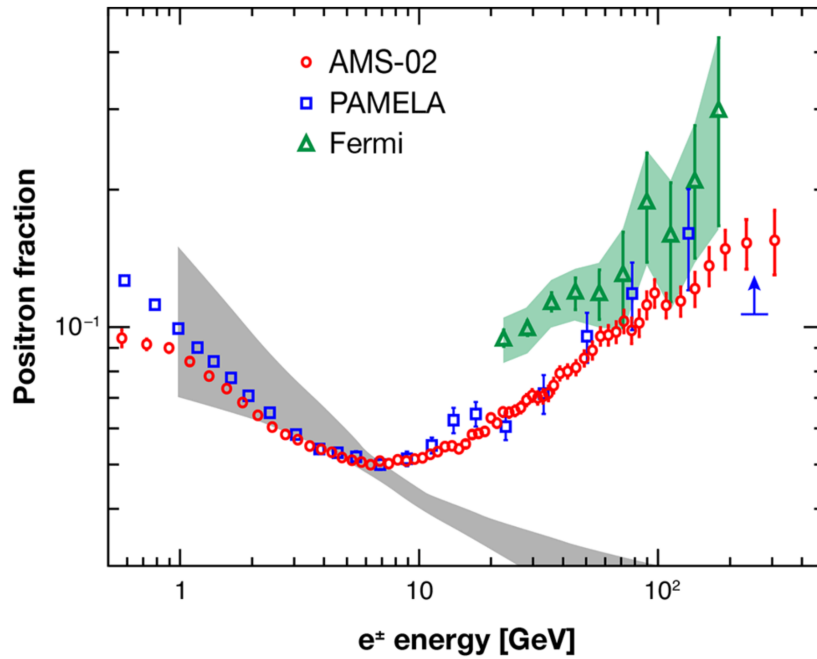


Figure 1.10: Measured positron fraction by *AMS-02*, *PAMELA* and *Fermi*; discrepancies with the expected flux from CR propagation (represented by the grey band) are evident [5]. Other sources for positron should exist. Grey thick bar represent the positron fraction value just considering the effects of the cosmic ray propagation.

are shown as a grey thick band. All three experiments show consistently a rise in the positron fraction above 10 GeV, while *AMS-02* data indicate a change of slope up to 275 GeV, as shown in figure 1.11.

Studying the positron fraction several characteristics may be highlighted:

- is not present any kind of *fine structure*;
- positron fraction steadily increases between 10 GeV and 250 GeV;
- the ratio is of the order of 10% after few tens of GeV;
- is possible to estimate that 90% of the electrons must be of primary origin; this is possible assuming that no positrons are accelerated at

sources, together with the symmetrically creation of matter and anti-matter in each interaction. Positrons are thus created by interactions of primary cosmic rays with the interstellar medium; this phenomenon is well predicted by all the cosmic ray propagation software, such as *GALPROP* or *DRAGON*.

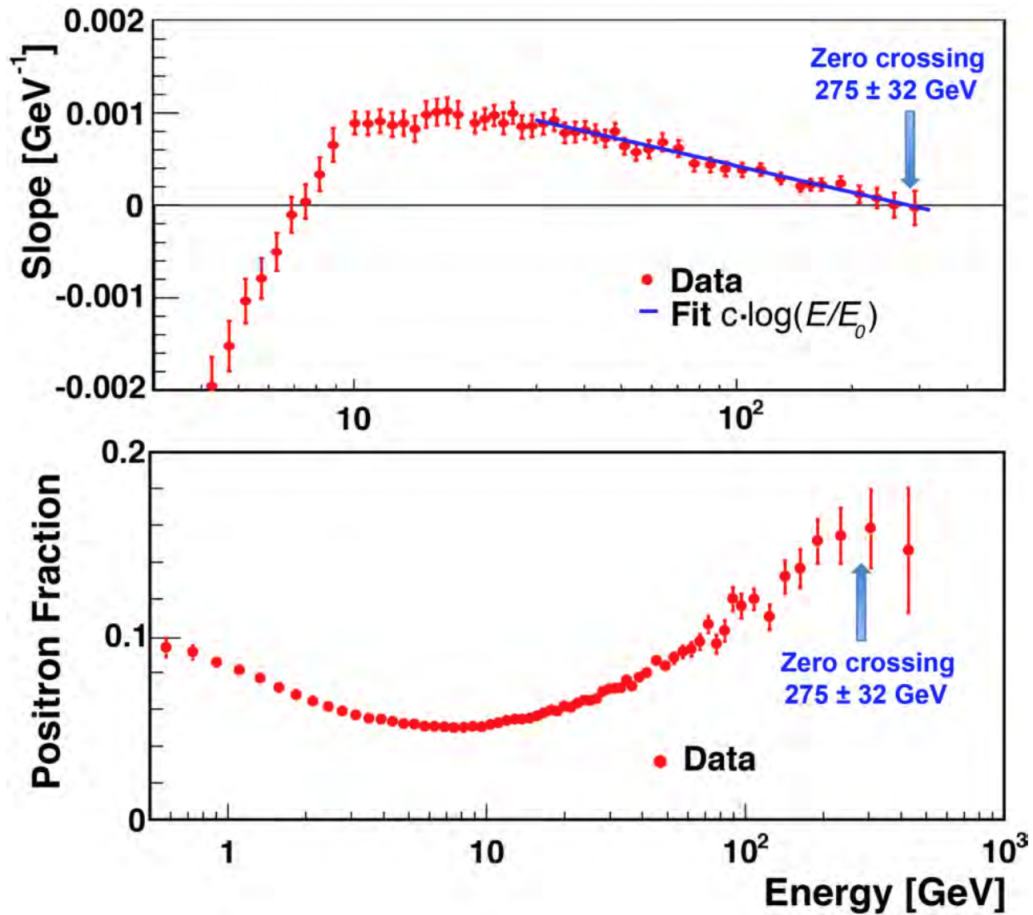


Figure 1.11: *AMS-02* positron fraction slope analysis [6].

Figure 1.11 highlights some of the characteristics of the positron fraction, such as its slope and the *zero crossing* point⁹.

⁹The *zero crossing* point is the value of energy at which the positron fraction stops to increase.

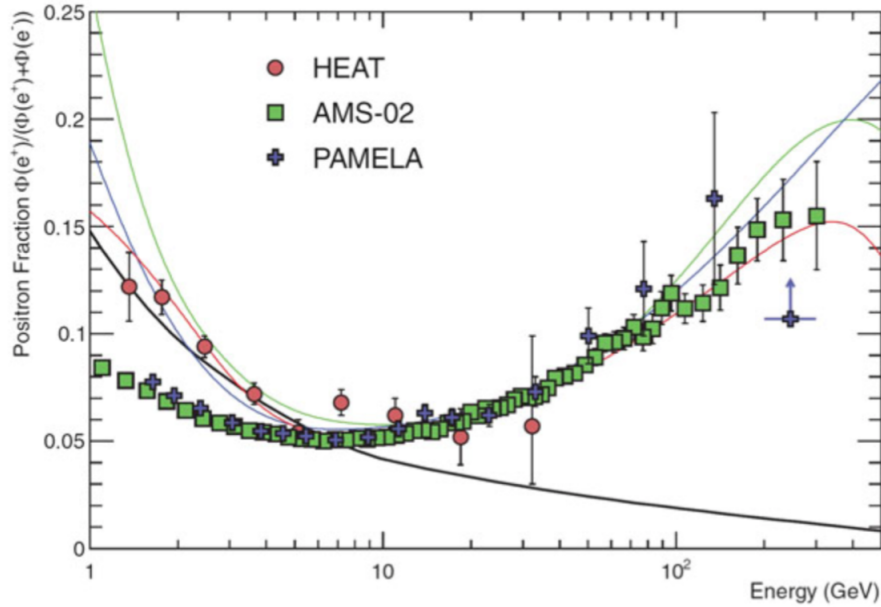


Figure 1.12: The graph shows a data fit with different models: dark matter decay (green), propagation physics (blue) and production in pulsars (red). The ratio below 10 GeV is dependent on the polarity of the solar magnetic field.

Figure 1.12 shows different theoretical models trying to fit the measured spectrum of the positron fraction; unfortunately all consistent with the measures at high energy, together with data lack in the same region, make this operation complex. Looking at the provided fitting models, two of them are particularly interesting, precisely regarding pulsars and dark matter and will be described in the following section.

The positron fraction strongly contradicts the assumption that positrons are produced only by the interactions of the primary cosmic rays with the interstellar medium; for this reason an additional new source of primary positrons is needed to explain the data.

Among the most likely and investigated scenarios there are e^+/e^- couples produced by annihilation of galactic dark matter particles or by astrophysical sources, such as pulsars.

The anisotropy study of the incoming directions of charged cosmic rays may be helpful to distinguish between these models.

Chapter 2

Anisotropy of the incoming directions of charged cosmic rays

In chapter 1 the basic concepts of cosmic rays physics, together with the characteristics of their sources, have been described, paying particular attention to *Dark Matter* and *Pulsars*.

Here we are going to deeply study the concepts of isotropy and anisotropy in the incoming directions of charged cosmic rays, applied to the case of electrons and positrons, describing how they could be used to explain and better understand the positron fraction measured by *AMS-02* [5,6].

This section is particularly important and resembles the center of this work; we'll start discussing about the distance from which cosmic rays are coming from, depending on energy and family of the particle, their confinement into the galaxy by non-collisional scattering processes with magnetic field irregularities, leading to the concept of isotropy and anisotropy on both theoretical and experimental point of view.

2.1 Confinement of cosmic rays

The cosmic rays continuously hit our planet from very different distances, principally depending on their mass, energy and *cooling* mechanism; just analyzing electrons and protons (and respective antiparticles) enormous dif-

ferences could immediately be highlighted¹. An accurate analysis of the physical processes acting on them is thus needed; electrons and positrons start to lose significant amount of energy, by radiative cooling, at relatively low energies (lower than that of the *knee*), strongly limiting their traveled distance through the interstellar medium. At the contrary, this is not valid for protons and heavier nuclei which, at the same energy, are able to cover larger distances².

The *slab-model*, briefly described in section 1.1, allows to obtain the crossed grammage ξ by the cosmic rays, together with their residence time τ inside the galaxy. Obtained this result is immediately possible to evaluate the traveled distance L , assuming the galactic density (including halo) $\rho = 0.3$ particles/cm³ and considering also their relativistic speed:

$$L = c\tau = \frac{\xi}{\rho} \sim 10^6 \text{pc} \quad (2.1)$$

The distance computed by equation 2.1 is several order of magnitude bigger than the galactic dimension, typically of order of several Kpc. The path of the cosmic rays is thus not *smooth* and continuous, but similar to a random one, ruled by radiation, matter and magnetic field distributions with which they continuously interact. As will be described in this section, the arrival directions of charged cosmic rays don't point to the sources and their flux is isotropic up to very high energies. That is an important difference respect to the photons; the electromagnetic radiation keeps the information about the generation sites, except for gravitational interactions.

Cosmic rays confinement, except in the case of extreme energy, let suppose that the particle sources are located into our galaxy.

¹See section 2.1.1 for more details.

²As an example, extremely high energy protons with energy $\sim 10^{20}$ eV may be able to cover a distance of 30 Mpc before loosing all their energy (*Greisen-Zatsepin-Kuzmin* effect, more details in appendix C). This value have to be compared with the 10 Kpc traveled by the electrons (positrons) (see section 2.1.1). Though these energies are numerous orders of magnitude higher than those that DAMPE is capable to measure (~ 10 TeV), this example well highlights the difference between adrons and electrons (positrons).

2.1.1 Electrons and positrons traveled distance

Evaluation of the traveled distance for electrons and positrons is not as easy as the proton case, and additional energy loss terms have to be taken into account in the description of their propagation. This is possible considering the propagation equations for cosmic rays, a real mine embedding all the physical processes and interaction that these particles perform:

$$\frac{dN_i}{dt} = D\nabla^2 N_i + \frac{\partial}{\partial E}[b(E)N_i] - \frac{N_i}{\tau_i} + \sum_{j>i} \frac{N_j}{\tau_{ij}} - nvN_i\sigma_i + \sum_{j>i} nvN_j\sigma_{ij} \quad (2.2)$$

All the single terms on the right hand side of equation 2.2 contribute to the variation of the number of particles regarding a certain species i , both in positive and in negative, considered fixed:

- $D\nabla^2 N_i$: this is the **diffusive term**, proportional to the density gradient through $D = \langle v_i \rangle / 3N_i\sigma_i$, the diffusion coefficient. As this last equation is describing, the diffusion coefficient is proportional to the velocity and the reciprocal of density and cross section of "i" species particles;
- $\frac{\partial}{\partial E}[b(E)N_i]$: this term resembles the **continuous energy losses**, due to radiative processes, such as inverse compton and synchrotron, principally concerning light particles.

$$\left\langle \left(\frac{dE}{dt} \right)_{tot} \right\rangle = \frac{4}{3} c\sigma_T U_{rad} \gamma^2 \beta^2 \quad (2.3)$$

$$\left\langle \left(\frac{dE}{dt} \right)_{tot} \right\rangle = \frac{4}{3} c\sigma_T U_B \gamma^2 \beta^2 \quad (2.4)$$

Equations 2.3 and 2.4 describe the mean energy losses by electrons and positrons during their diffusion through the galaxy; σ_T represents the Thomson cross section, U_{rad} and U_B are respectively the energy density of the radiation and magnetic fields.

The cross section of the processes is proportional to the square of the mass of the charged particle. The radiative energy losses can be ignored

for particles heavier than electrons and positrons, at least for energies below that of the *knee*.

- $\frac{N_i}{\tau_i}$ and $\sum_{j>i} \frac{N_j}{\tau_{ij}}$ represent **the decay of instable elements**, with a lifetime τ_i and τ_{ij} respectively. While the first term resembles the decay of "i" particles the second represents, on the contrary, the decay of "j" elements to "i". The decay terms are fundamental especially for the description of nuclei propagation;
- $nvN_i\sigma_i$ and $\sum_{j>i} nvN_j\sigma_{ij}$ are the **spallation terms**; consisting in the interaction of heavier nuclei with the interstellar medium (principally protons) that produce lighter particles.

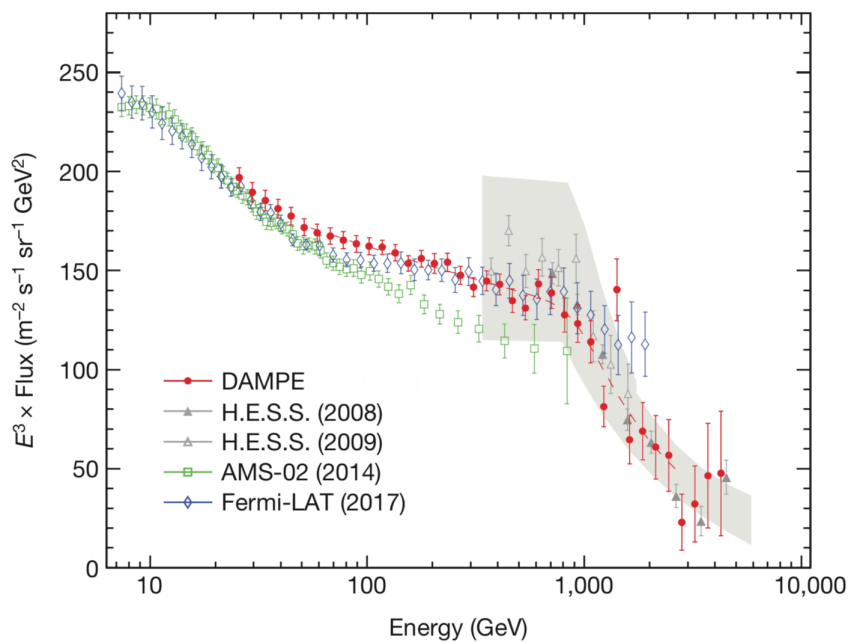


Figure 2.1: The spectrum of electron plus positron (multiplied by E^3) measured by *DAMPE* [7], together with the measurements of the previous experiments. The grey band represents *H.E.S.S.* systematic errors apart from the approximately 15% energy scale uncertainty. The error bars ($\pm 1\sigma$) of *DAMPE*, *AMS-02* and *Fermi-LAT* include both systematic and statistical uncertainties added in quadrature.

Figure 2.1 is the *all-electron* ($e^+ + e^-$), i.e. the sum of the electron and positron flux) spectrum, measured by *DAMPE* in 2017, based on more than 500 days of data acquisition [7]. In the plot the red dashed line represents a smoothly broken power-law model that best fits the *DAMPE* data in the range 55 GeV to 2.63 TeV. The direct measurements from the space-borne experiments *AMS-02* and *Fermi-LAT*, together with the indirect measurement by the *H.E.S.S.* experiment.

The all-electron spectrum shows, for the first time, a break in correspondence of 0.9 TeV, consistent with the 1 TeV break obtained (by indirect measurements) by ground-based experiments, such as *H.E.S.S.* [8] and *VERITAS* [9]. The analysis of the spectrum shows a softening of the spectral index γ from -3.1 to -3.9: this feature is expected by the radiative energy loss of electrons and positrons [10]. To explain the data different theoretical models have been considered; among all, the case of CRs released during the final life stages ($\sim 10^5$ years) of a smoothly distributed SNRs, cooled by radiative losses, seems to naturally explain the break.

To evaluate the traveled distance of the incoming particles, in case of electrons and positrons, we consider a diffusive model, where no other physical process is considered:

$$\frac{dN_i}{dt} = D\nabla^2 N_i \rightarrow N(x, t) = \frac{N_0}{\sqrt{\pi Dt}} e^{-\frac{x^2}{4Dt}} \quad (2.5)$$

A gaussian path-length distribution is expected in the purely diffusive propagation obtaining that particles move on average of $\lambda \approx (2Dt)^{1/2}$. Considering the energy dependence of the diffusion coefficient, the distance traveled by particles could be written as its time integral:

$$\lambda(E, E_0) = \left(\int_0^{\tau(E)} D(E') d\tau' \right)^{1/2} = \left(\int_{E_0}^E \frac{D(E') dE'}{b(E')} \right)^{1/2} \quad (2.6)$$

The mean galactic value for D is approximately $10^{29} \text{ cm}^2 \text{ s}^{-1}$ and, considering only energy losses by Inverse Compton (IC) and synchrotron, the distance traveled by the electrons with 1 GeV energy is 10 kpc.

Neglecting the energy dependence of the diffusion coefficient, is possible to evaluate the distance: $\lambda \propto E^{-1/2}$.

Radiative losses need to be considered if we want estimate the maximum traveled distance of electrons and positrons; λ permits to evaluate the distance traveled by the particles. Figure 2.2 shows the relation between the energy of the particles and the traveled distance: for increasing particle energy, the distance of propagation quickly decreases: for example, 1 TeV electrons measured at Earth are constrained to a maximum origin distance of 30 pc from our planet.

Table 2.1: Maximum distance of propagation for electrons

Distance (Kpc)	Energy (GeV)
9	1
3	10
1	100
0.03	1000

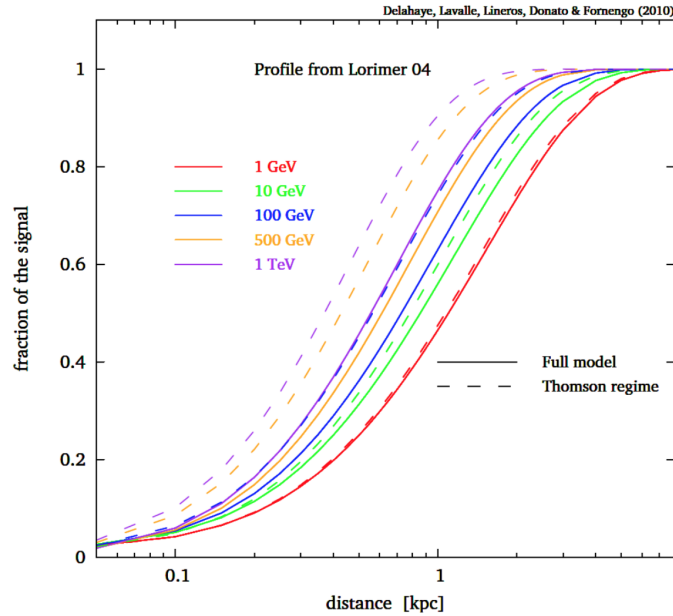


Figure 2.2: Fraction of flux intensity loss for e^+ and e^- , as function of their energy and traveled distance [11]. These particles have strong radiative cooling and arrive at Earth if produced within few Kpc around it.

Due to their large energy losses, it seems not plausible (contrary to the case of protons and nuclei) that the observed electrons originate from a uniform distribution of sources in the Galaxy. If the source is too far, the probability that an electron reaches the Earth is extremely small. More likely, primary high-energy electrons observed on Earth originate from a small number of sources well localized in space and relatively close (on a scale of galactic distances) to the Solar System, as shown by figure 2.3.

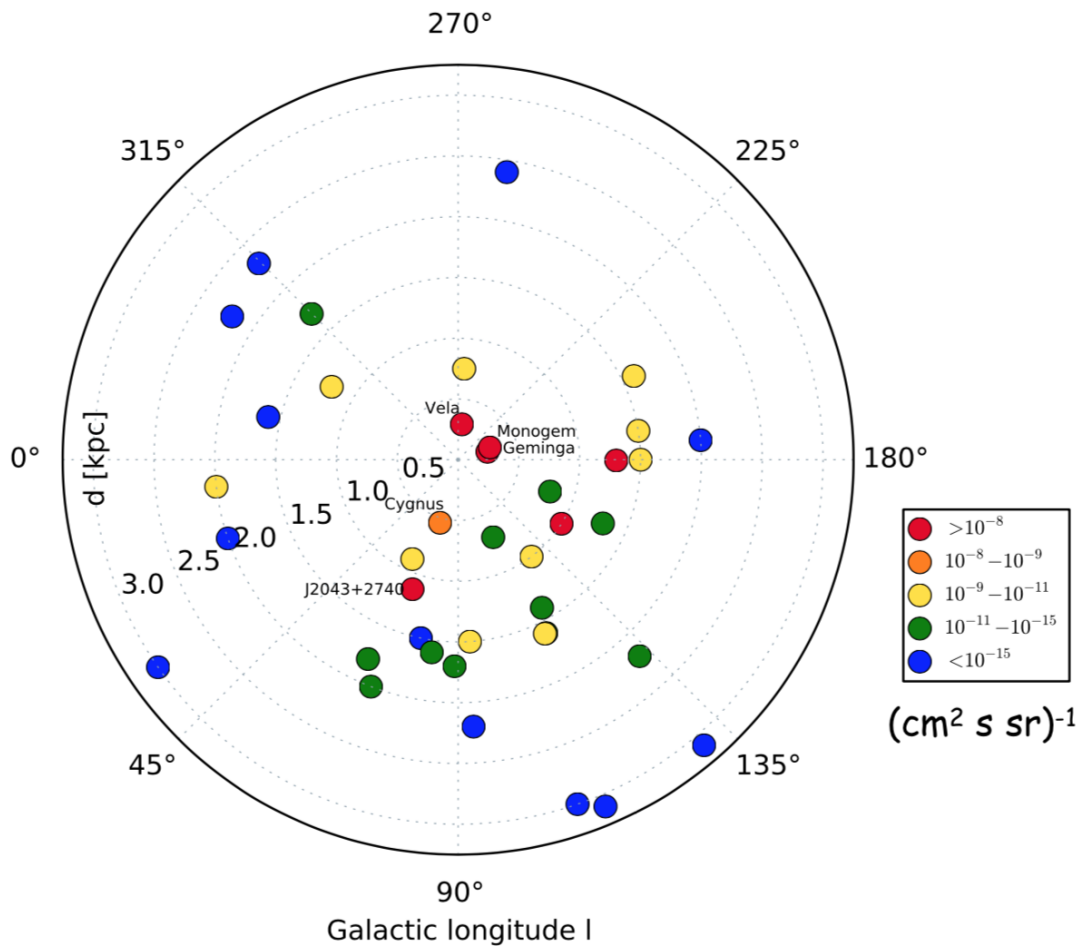


Figure 2.3: Most powerful known sources within 3 Kpc from the Sun [12].

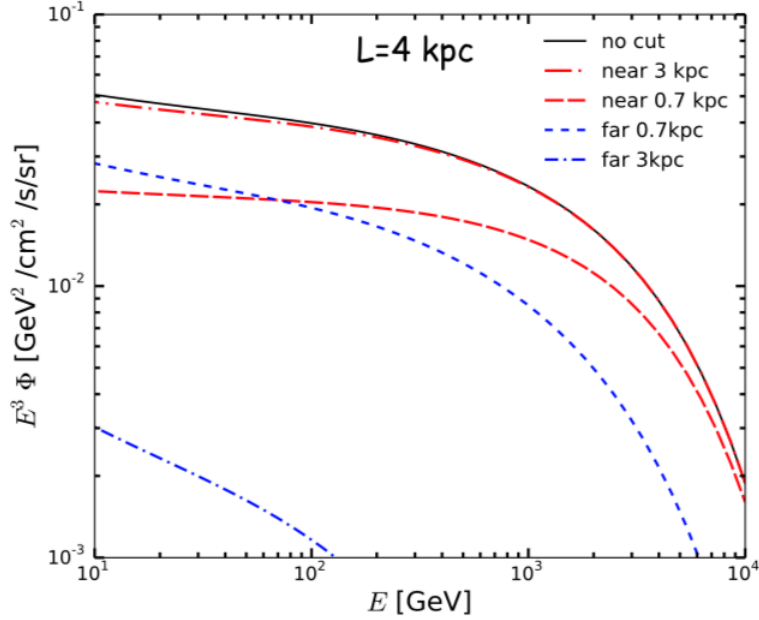


Figure 2.4: Electron flux [13]. Several cuts have been added to each single graph considering different distances for incoming particles. Fluxes are multiplied to E^3 to better highlight slope variations.

In figure 2.4 is presented the electron fluxes from a smooth SNR distribution [13] from a very few Kpc from Earth; the contribution from different distances have been separated, considering different distances; in order to evaluate the relevance of the sources of electrons and positrons relatively far into the entire measured flux. Looking at the results, on both graphs the whole spectrum is practically coincident with the electron flux relative to particles coming from a distance smaller than 3 Kpc . We can argue that less than 10% of the electrons come from distances bigger than 3 Kpc .

Due to the features of the propagation distance of electrons and positrons, the analysis of the properties of cosmic ray ele and pos provide important information to study the sources in the galactic neighborhood. The measurement of such channel is, therefore, one of the most relevant investigation of the majority of detectors for direct detection of cosmic rays in space.

2.2 Isotropy and Anisotropy in cosmic rays

In this section we are going to introduce the important concepts of isotropy and anisotropy of cosmic rays, on which all the other chapter of this work will be based. The search for patterns in the incoming direction of charged cosmic rays is important not only to provide information on the distribution of sources in the galactic neighborhood, but it can be also studied to investigate and provide an explanation for the unexpected behavior of the cosmic rays, that could be due to *new physics* effects.

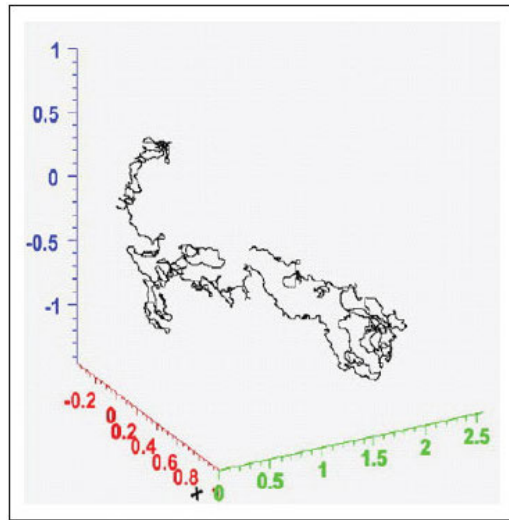


Figure 2.5: Trajectory of a simulated cosmic ray, with energy ~ 10 TeV, in a $1\mu\text{G}$ turbulent magnetic field. Note: distance scales are in units of Kpc.

As we briefly stated, at the beginning of section 1.4, while arriving to our detectors, cosmic rays don't travel linearly; on the contrary they continuously change direction because of non collisional scattering processes with magnetic field inhomogeneities.

A simulation of this process is shown in figure 2.5, where a cosmic ray of energy ~ 10 TeV propagates through a $1\mu\text{G}$ turbulent magnetic field³, a value similar to the one in our galaxy.

³Due to *guide center decomposition* procedure, a charged particle's motion in a magnetic field can be decomposed in three quasi-periodic components: **gyration** around the field lines, **bouncing** between the mirror points along them and **drifting** normal to the field line and to the field gradient.

Due to the randomization of the charged cosmic ray trajectories, the flux of charged cosmic rays at Earth is extremely isotropic. This means that we do not observe a macroscopic, dominant, direction of arrival of cosmic rays. However, in case of few localized nearby sources as for high energy electrons and positrons, the randomization is not completely efficient, and several models predict a residual anisotropy in the arrival direction of electrons and positrons. As of today, however, no anisotropy has been measured for the e^+/e^- channel, and only upper limits have been set.

$$\delta = \frac{I_{max} - I_{min}}{I_{max} + I_{min}} \quad (2.7)$$

Equation 2.7 defines isotropy amplitude; that's the difference between flux intensity in direction of the dipole minimum and maximum respectively, normalized to their sum.

- experimental results indicate only negligible amounts of anisotropy at low energies, with δ increasing with energy;
- below $E \approx 10\text{GeV}$, solar modulation affects the original directions of the cosmic rays;
- for higher energies, direction of maximum excess is close to that of the Local Supercluster of Galaxies.

2.3 Possible sources of the positron excess

The positron fraction, shown in section 1.6, clearly shows that a new positron source should exist; both nearby astrophysical sources, such as pulsars or SNRs⁴, and dark matter annihilation process could contribute to the excess. In this section we are going to provide a set of observable that could provide information to distinguish the nature of the primary source that dominates the production of primary electrons and positrons to explain the positron fraction rise.

⁴Super Novae Remnants

Dark matter is supposed to permeate all the galactic halo and our surroundings; for this reason we expect the arrival directions of dark matter annihilation products to be distributed isotropically⁵ [14]. On the contrary, particles produced by pulsars (or others point-like astrophysical sources) arrive from a certain localized space region and the distribution of their directions is expected to be anisotropic.

In the next few lines some examples of expected dipole anisotropy for SNRs and PWNs models will be provided. Since the *Vela* SNR is the most intense local source, it has been taken as example, while *Geminga* and *Monogem* have been chosen as main representative examples of PWNs.

The study of the spectrum of the positron fraction alone is not sensitive enough to distinguish between the model proposed, as discussed in [15]. The assumption that a Dark Matter origin of primary electron and positron spectrum would show a sharp cut-off (at the value corresponding to the particle's mass) while in the positron fraction spectrum an astrophysical source would present a smoother decline is a simplistic picture. For example, a combination of several channels for the annihilation of dark matter particles (including the hadronic ones) can result in a smooth, non sharp, decrease in the positron fraction. On the contrary, an opportune combination of young and nearby pulsars could explain the positron fraction data and produce a steep spectral descent, mimicking what expected for simple models in which DM annihilates directly to electron and positron pairs.

In this framework the anisotropy study of the arrival directions of electrons and positrons could be really helpful to distinguish between different models, producing more robust conclusions.

A search for anisotropies in CR electrons and positrons was performed by *PAMELA* [16], *AMS-02* [17, 18] and *Fermi-LAT* [4, 19] experiments (with a technique described in section 4.5): no anisotropy has been found, and only upper limits have been set.

The *Fermi-LAT* experiment searched for an $e^+ + e^-$ anisotropy in the first year [4] and 7 years [19] of data, with energies above 60 GeV in order to minimize the effects of the geomagnetic field and the Heliospheric Magnetic

⁵Other theories provide a different description of the dark matter distribution into the galactic halo; DM *subhalo* are restricted dark matter domains, whose annihilation products thus result anisotropically distributed. Distinguish between a point-like astrophysical source and a DM subhalo results particularly complex.

Field, both affecting the direction of detected charged particles in the GeV range. The upper limits $\Delta_{e^+e^-}$ have been obtained from spherical harmonics based analysis, particularly similar to the one used in this work. In case of low statistic samples the upper limits (ULs), at 95% CL, range from $\Delta_{e^+e^-} = 0.005$ to $\Delta_{e^+e^-} = 0.010$. Though the analysis of 7 years of data, ULs at 95% CL cover an interval from $3 \cdot 10^{-3}$ to $3 \cdot 10^{-2}$.

The *PAMELA* experiment has performed a search on large-scale positron dipole anisotropy with the first four years of data. The sample consists of 1489 e^+ with rigidity $10 \leq R \leq 200$ GV. To account for the instrument exposure, and other detector effects, the results are given in terms of positron over proton ratio⁶. Also in this case an upper limit, $\Delta_{e^+e^-} = 0.166$, at 95% CL has been fixed.

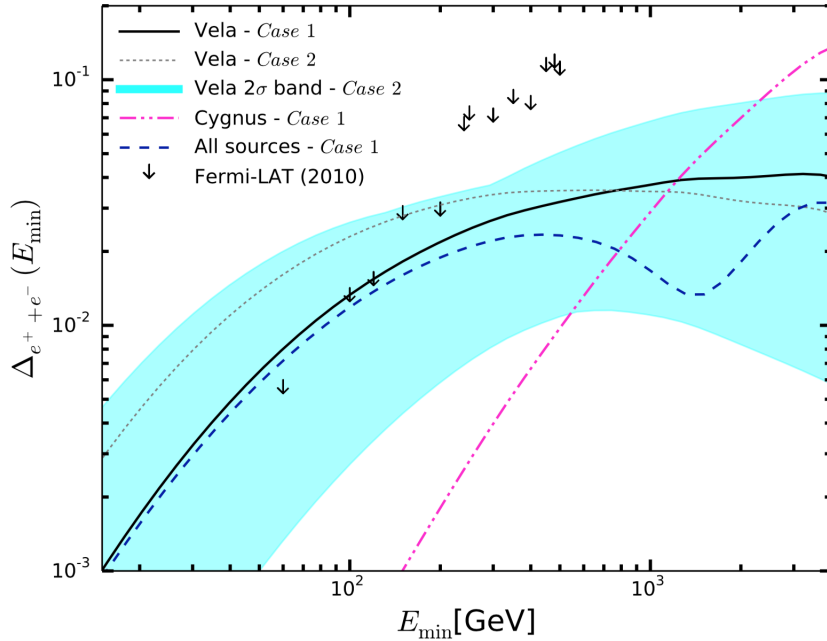


Figure 2.6: Predictions for the dipole anisotropy in the $e^+ + e^-$ flux from single SNRs, for and $R_{cut} = 0.7 Kpc$ [20]. The energy bins are integrated in energy from E_{min} up to 5 TeV. The downward arrows represent the *Fermi-LAT* upper limits for the 2010 analysis, based on 1 year of collected data.

⁶At these energy values the distribution of the incoming directions of the protons is isotropic.

It should be noted that the upper limits discussed refer to different observables: $e^+ + e^-$ for *Fermi-LAT*, e^+/e^- for *AMS-02* and e^+ for *PAMELA*.

Figure 2.6 is the result of an all-electron flux simulation showing the predicted anisotropy for a near SNR. Case 1 and 2 refer to different methods to inject model parameters.

The anisotropy value is an increasing function of the energy, at least up to few hundreds GeV, depending on the model chosen. For E_{min} below 200 GeV, the *Fermi-LAT* upper limits lie in the Vela anisotropy band, while for higher energies the experimental limits are at least a factor of two higher than the maximal expected $\Delta_{e^+e^-}$.

Similar simulations has been realized to predict anisotropy values for near PWNs.

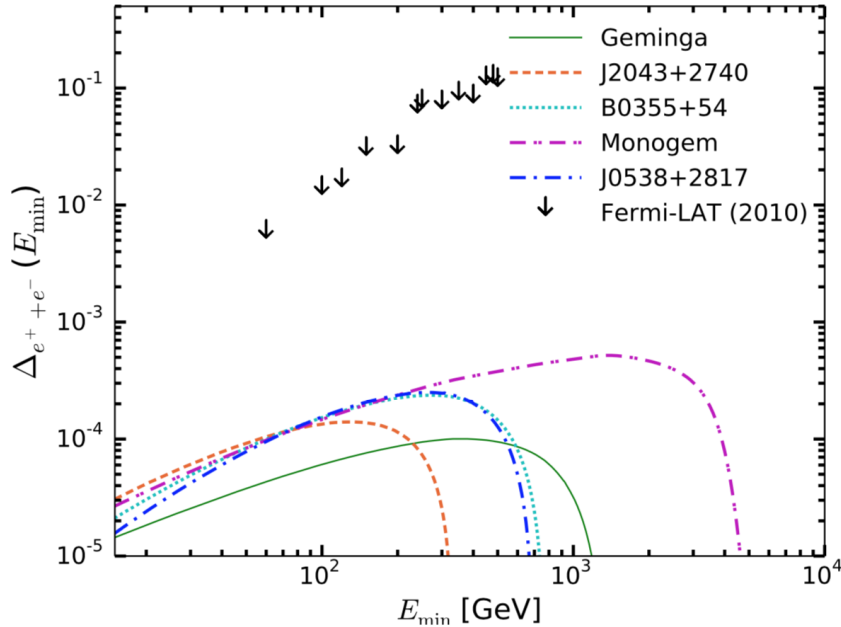


Figure 2.7: Predictions for the anisotropy from single PWNe in the $e^+ + e^-$ flux, along with experimental upper limits from *Fermi-LAT* [20]. The energy bins are integrated in energy. The results are for the five most powerful PWNs, as labeled inside the panels.

The *Fermi-LAT* upper limits, as graph in figure 2.7 clearly shows, are several orders of magnitude higher respect to the expected anisotropy level. *Fermi-LAT* sensitivity rapidly diminish with the increasing energy, highlighting the impossibility to provide a measure of $\Delta_{e^+e^-}$.

The search for anisotropies in the electron and positron channel is an extremely complicated scenario: as of today, the upper limits set by *Fermi-LAT*, *PAMELA* and *AMS-02* on different observables are used to limit the parameter space of astrophysical models that could explain the positron fraction rise.

The expected anisotropies are very faint at low energies even for the limits set by the most sensitive detector *Fermi-LAT*, but increase at higher energies. Measurements from the most recent generation of cosmic ray direct detection experiment may provide additional information to the scenario, by providing an independent search for anisotropies that could confirm, or possibly improve, the current limits.

DAMPE is a new generation calorimetric experiment, that has been developed to improve the energy resolution and containment for cosmic rays in the TeV region. The data collected by the detector can be analyzed to search for anisotropies especially at the high energy regime.

In this thesis, the sensitivity of *DAMPE* for the search of anisotropies in the cosmic rays will be studied.

Chapter 3

The DAMPE Detector

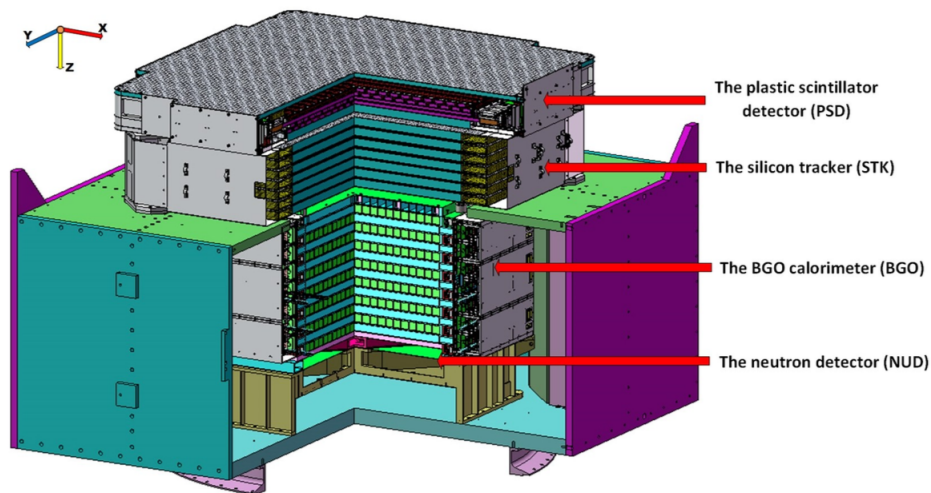


Figure 3.1: Schematic view of the DAMPE detector [21].

The DARK Matter Particle Explorer (DAMPE), is a detector on board of a satellite, successfully launched into a sun-synchronous orbit¹ on 2015 December 17th, from the Jiuquan launch base.

This detector offers a new opportunity for advancing our knowledge of cosmic rays, dark matter, and gamma-ray astronomy. DAMPE is able to

¹This is the primary observing mode, at the altitude of 500 km; DAMPE is expected to cover the full sky at least four times in two years.

detect electrons/positrons, gamma rays, protons, helium nuclei and other heavy ions in a wide energy range with much improved energy resolution and large acceptance, compared to *AMS-02* and *Fermi-LAT*.

The main goals of the experiment are the following:

- understanding the mechanisms of particle acceleration operating in astrophysical sources and the propagation of cosmic rays in the the Milky Way;
- probing the nature of dark matter;
- studying the gamma-ray emission from Galactic and extragalactic sources.

Respect to *Fermi-LAT*, *DAMPE* is capable to distinguish electrons from the hadronic background up to one over 10^6 ; having an high rejection power is a fundamental characteristic in order to realize anisotropy measurements.

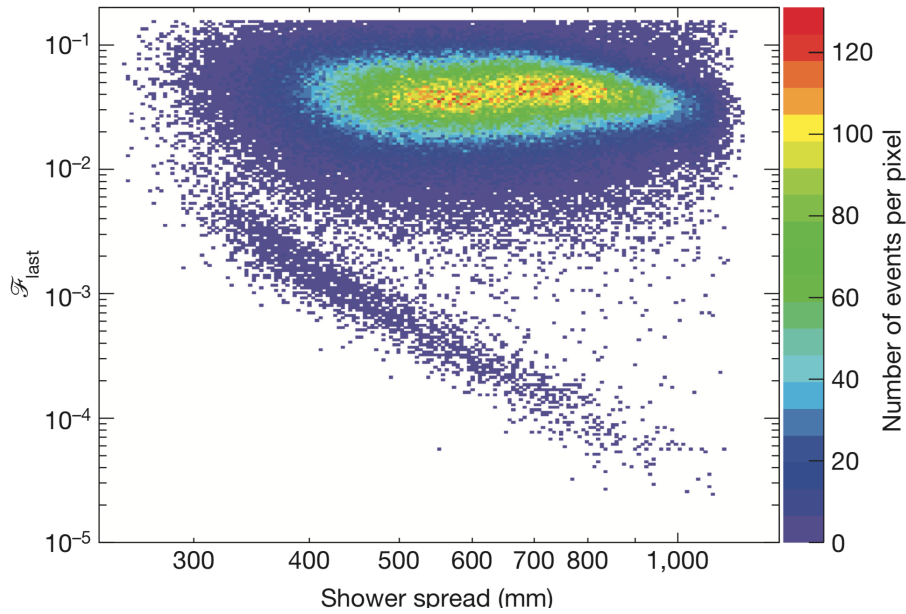


Figure 3.2: Discrimination between electrons and protons in the BGO instrument (section 3.0.3) of *DAMPE* [7].

To separate electrons and positrons from the proton background, different techniques have been used: (a) comparison between MC simulations of hadronic and electromagnetic showers inside the calorimeter and the acquired data, intensive beam tests at CERN facility and boost decision trees.

The plot in figure 3.2 shows the rejection power of *DAMPE* flight data, with energies between 500 GeV and 1 TeV; both the electron (the lower population) and proton candidates (the upper population) are clearly recognizable. \mathcal{F}_{last} represents the ratio of energy deposited in the last BGO layer to the total energy deposited in the BGO calorimeter. The shower spread is defined as the summation of the energy-weighted shower dispersion of each layer.

The DAMPE collaboration published in 2017 an article [7] highlighting, for the first time in the case of a space experiment, a break in the *all-electron* spectrum, as shown in figure 2.1.

The accurate measurement of the proton's spectrum is one of the goals of the experiment; figure 3.3 is a projection of the flux over three years of data acquisition, compared with other experiments.

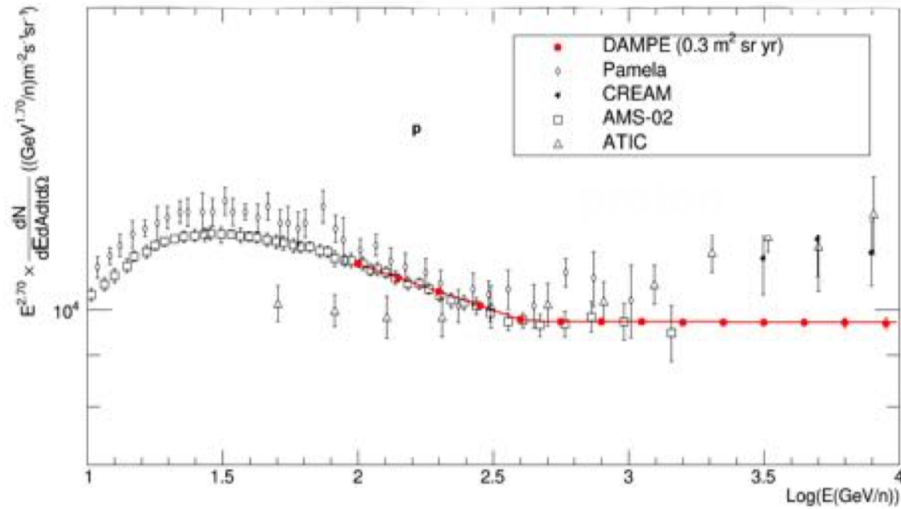


Figure 3.3: Three years projection of the proton spectrum measurement of DAMPE experiment, compared with other ones.

DAMPE is capable to precisely measure photons energy up to the TeV; in

figure 3.4 is represented a preliminary gamma sky map, for photons with energy bigger that 1 GeV.

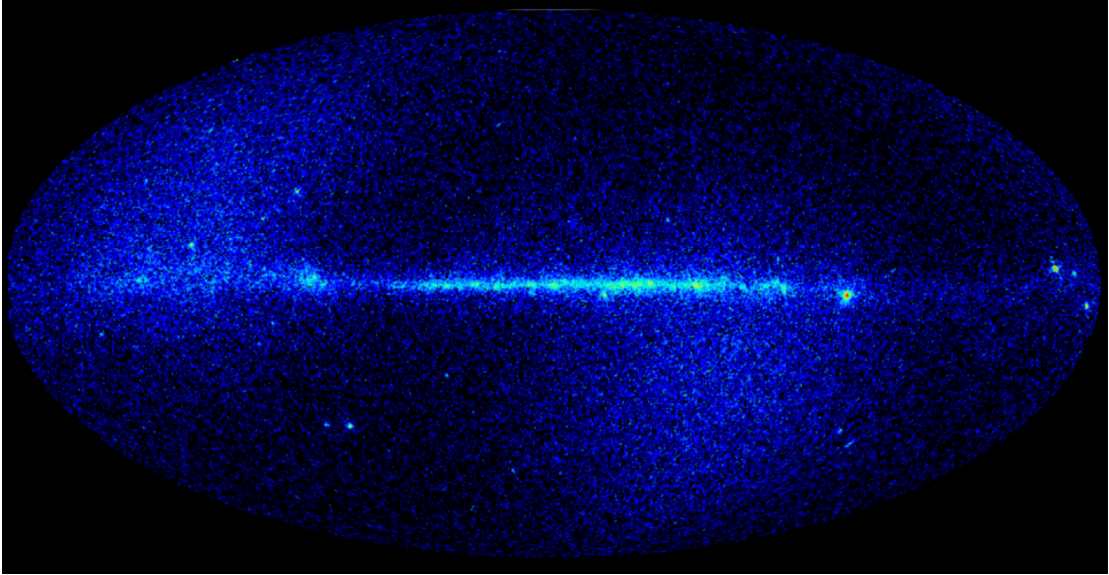


Figure 3.4: Preliminary DAMPE γ sky map, with energy bigger that 1 GeV.

As explained in section 1.5, photons may be the final state of annihilating DM particles; differently from all the other particles, γ do not interact with galactic magnetic field, maintaining so the information on the incoming direction. That is the reason why their study is particularly important.

Respect to other experiment, such as *AMS-02* and *Fermi-LAT*, *DAMPE* is capable of precise and accurate energy measurements from 5 GeV up to 10 TeV for electrons (positrons) and photons, while for the adronic component of the cosmic rays energy ranges from 50 GeV to 100 TeV. The electromagnetic calorimeter is characterized by a depth of 32 radiation lengths (compared with the 8.6 of *Fermi-LAT* and 17 of *AMS-02*) and an energy resolution of the 1.5% at 800 GeV²; differently from the other, *Fermi-LAT* in particular, *DAMPE* is capable of precise energy measurements in narrow energy bins, a feature particularly useful for the study of the anisotropy of the incoming

²This value refers to electrons and photons. In case of protons or heavy nuclei the energy resolution is less than 40% at the same energy.

directions of the charged CRs. All the detectors guarantee an high rejection power of 10^6 from the proton background, from the 300 times to 800 times bigger respect to the electron flux.

Considering all the characteristics until now explained, *DAMPE* is a powerful instrument to perform anisotropy measurements in the incoming direction of charged CRs; all the techniques and the developed analysis methods will be explained in the next chapters.

Figure 3.1 shows a schematic view of the DAMPE detector, from top to bottom: a Plastic Scintillator strip Detector (PSD), a Silicon-Tungsten trackConverter (STK), a BGO imaging calorimeter and a Neutron Detector (NUD).

Table 3.1: Summary of the design parameters and expected performance of DAMPE instrument [21]

Parameter	Value
Energy range of γ -rays/electrons	5 GeV - 10 TeV
Energy resolution ^a of γ -rays/electrons	$\leq 1.5\%$ at 800 GeV
Energy range of protons/heavy nuclei	50 GeV - 100 TeV
Energy resolution ^a of protons	$\leq 40\%$ at 800 GeV
Effective area at normal incidence (γ -rays)	1100 cm ² at 100 GeV
Geometric factor for electrons	0.3 m ² sr above 30 GeV
Photon angular resolution ^b	$\leq 0.2^\circ$ at 100 GeV
Field of View (FoV)	~ 1.0 sr

Notes: ^a σ_E/E assuming Gaussian distribution of energies. ^b At 68% containment radius.

3.0.1 The Plastic Scintillation array Detector (PSD)

The main purpose of this detector is to provide a charged particles background rejection for the photon measurement, together with the precise measurement of the high energy particle's charge Z in a wide range, $Z \leq 26$. DAMPE is equipped with two PSD layers, each one with an effective area of $82\text{cm} \times 82\text{cm}$; the whole sub-detector consists in 82 plastic scintillator bars, each with a double layer configuration, where the upper layer ones are placed orthogonally to the bottom ones. Each of them is 88.4 cm long

with a $2.8\text{cm} \times 1.0\text{cm}$ section; signals are readout by two Hamamatsu R4443 Photomultiplier Tubes (PMTs) coupled to the ends of each scintillator bar. The bars of the two layers of a plane are staggered by 0.8 cm, allowing a full coverage of the detector with the active area of scintillators without any gap³.

As the efficiency of a single layer is greater than 0.95, the PSD provides an overall efficiency ≥ 0.9975 for charged particles.

The segmented structure of the PSD allows to suppress the spurious veto signals due to the *backsplash effect*, which can lead to a misidentification of gamma rays as charged particles. This phenomenon was observed in *EGRET* and was found to be significant for photon energies in the GeV region and above. A similar choice of the segmented design was adopted in the *AGILE* and the Large Area Telescope onboard the Fermi telescope (*Fermi-LAT*), both equipped with anti-coincidence detectors consisting of plastic scintillator tiles.

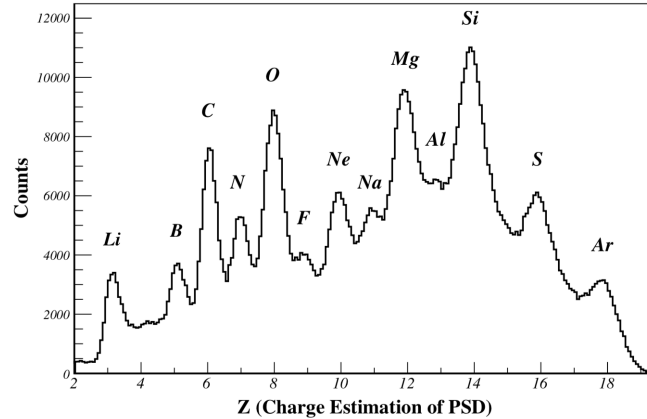


Figure 3.5: Reconstructed charge spectra of PSD for nuclei with $A/Z = 2$, generated by a $40\text{ GeV/n } ^{40}\text{Ar}$ beam [21]. The helium peak has been removed for clarity.

Since the PSD is used to identify the nuclei charge (from helium to iron, as shown in figure 3.5), a wide dynamic range extending up to ~ 1400 times the energy deposition of a minimum ionizing particle (MIP)⁴ is required. To cover

³To minimize the materials used in the active area, the mechanical support is mainly made by honeycomb boards with Carbon Fiber Reinforced Plastics (CFRP)

⁴A singly charged MIP at normal incidence, which is assumed as reference, deposits on

such a broad range with good energy resolution, a double dynode readout scheme for each PMT has been implemented. Signals from the dynode with high gain cover the range from 0.1 MIPs to 40 MIPs, while those from the dynode with low gain cover the range from 4 MIPs to 1600 MIPs; the overlap region can be used for cross calibration.

PSD performances have been tested through beam test experiment at CERN facility, using relativistic ions beams.

Figure 3.5 clearly shows that nuclei from lithium ($Z = 3$) up to argon ($Z = 18$)⁵ were correctly recognized.

3.0.2 The Silicon-Tungsten trackER-converter (STK)

Like the PSD, the STK detector has been designed to pursuit different goals, such as the precise particle track reconstruction with a resolution better than $80 \mu m$ for most of the incident angles, the measurement of the electrical charge of incoming cosmic rays and the γ photoconversion up to electron/positron couples.

The STK is characterized by six double-planes of silicon detectors, with a total sensitive area⁶ of $\sim 7 m^2$; multiple tungsten layers have been inserted in the tracker structure, in order to perform the photo-conversion of high energetic γ rays (with energy above ~ 5 GeV). The total length available for the process is $1.425 X_0$, leading to a conversion efficiency of the 65%.

The overall sub-detector must present lightness and strength as main structural characteristics, in order to withstand the vibrations and accelerations during the launch. The alignment of each tungsten plate with respect to the 4 corners of the tray has been checked with a X-ray scan at CERN.

The STK detector is equipped with a total of 768 single-sided AC-coupled silicon micro-strip detectors (SSD), while the total strip length along a ladder (the union of four SSDs) is about 37 cm. Each silicon layer consists of 16 ladders, as shown in the top image of figure 3.6.

average about 2 MeV in a single PSD bar.

⁵The Birks-Chou law permits to extend the results up to the iron nuclei, $Z = 26$.

⁶Comparable with the total silicon surface of the AMS-02 tracker.

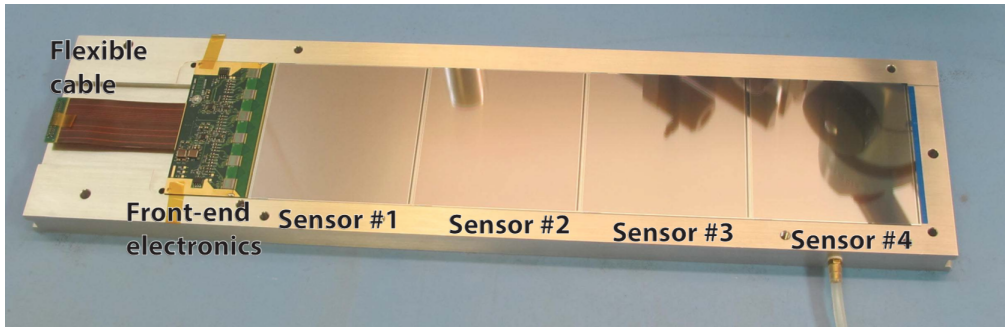
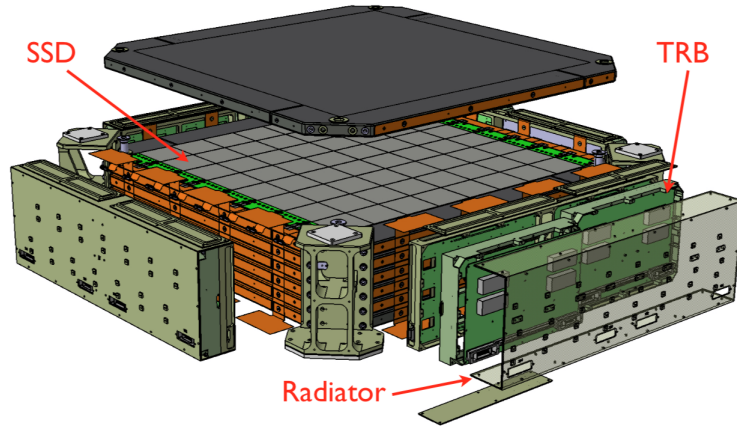


Figure 3.6: **(top)** Schematics of DAMPE’s STK, complete of the radiators and the Tracker Readout Boards (TRB) [21]. **(bottom)** Image of a ladder, complete of PCB cable, front-end electronics and four SSDs [21].

The silicon ladders on the bottom surface of each tray are placed orthogonal with respect to the ones of the top surface of the lower tray, in order to measure the X-Y coordinates of the incident particles (note that the Z coordinate of each plane is precisely known)⁷. This permits to obtain a full 3D tracking of all the particles crossing the sub-detector. The inter-distance between two consecutive silicon layers is ~ 3 mm.

⁷*AMS-02*, at the contrary, is equipped with double-face SSDs; this permit to reduce the thickness of the particle crossed material, decreasing in turn the *multiple-scattering* effects.

Table 3.2: Summary of designed parameters of STK [21]

Parameter	Value
Active area of silicon detectors	$0.55 \text{ m}^2 \times 12 \text{ layers}$
Thickness of each silicon layer	$320 \text{ } \mu\text{m}$
Silicon strip pitch	$121 \text{ } \mu\text{m}$
Thickness of tungsten layers	$3 \times 1\text{mm}$
Total thickness of the converter	$1.425 (X_0)$
Spatial resolution ^a	$< 80 \text{ } \mu\text{m}$ within 60° incidence
Power consumption	82.7 W
Total mass	154.8 kg

Notes: ^a 68% extension range.

The readout is done one every other strip (corresponding to 384 channels per ladder and a pitch of $240 \text{ } \mu\text{m}$), in order to keep a good performance in terms of spatial resolution, and at the same time reduce the number of readout channels. Both the acquisition process and power supply functions are performed by the Tracker Readout Boards (TRB), mounted on the side of the tray, as shown in figure 3.6 (top); each of them is connected to 24 ladders.

Figure 3.7 highlights two important characteristics of the STK; the top one refers to the charge ID, showing a clear particle identification up to the oxygen (to better represent all the distributions, $Z = 1$ particles have been removed from the sample).

The bottom figure shows the spatial resolution of the STK planes, as function of the incoming particles angles; as the graph highlights the minimum resolution is in general obtained with an incidence angle of 20° . In this case the charged particles cross a thicker quantity of Silicon, respect to the case of normal incidence; the bigger energy deposit permit to better interpolate the incidence point. For highly inclined particles crossing, at the contrary, the produced charge is splitted on numerous strips, obtaining a worse resolution. considering the capacitive-readout (analog readout) of the energy deposits, when the produced charge is divided on an high number of strips.

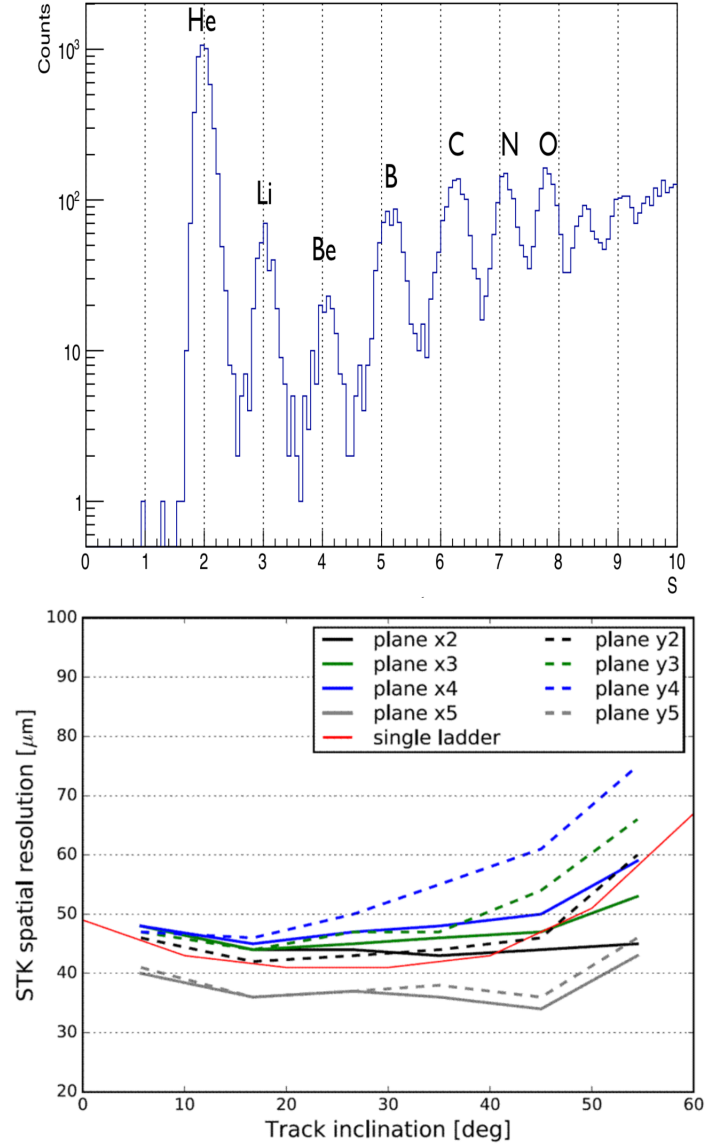


Figure 3.7: **(top)** STK signal mean distribution for nuclei produced by a lead beam on target, after removing $Z=1$ particles [21]. The signal mean, with current reconstruction procedures, allows for the identification of ions until Oxygen. **(bottom)** Spatial resolution for different STK planes as a function of particle incident angle for cosmic rays data at ground [21].

3.0.3 The BGO calorimeter (BGO)

The BGO calorimeter on board of DAMPE experiment has three main purposes: measuring the energy deposition of incident particles, imaging the 3D profile (both longitudinal and transverse) of the shower development and providing the level 0 trigger for the data acquisition system.

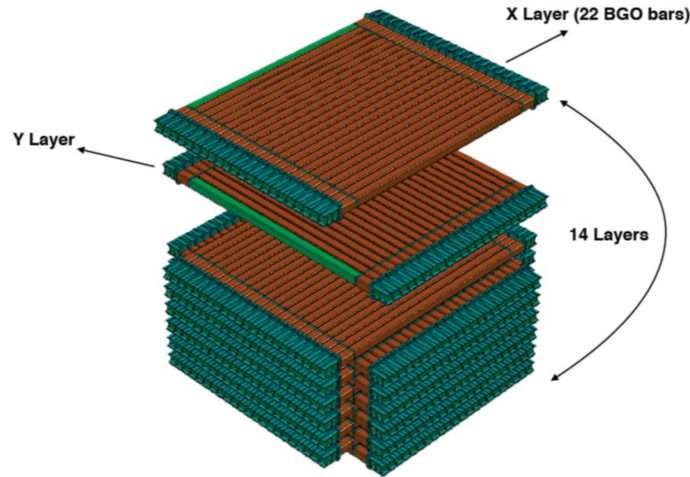


Figure 3.8: Schematic view of the DAMPE BGO calorimeter [21].

Table 3.3: Summary of designed parameters and expected performance of the BGO calorimeter [21].

Parameter	Value
Active area	60 cm \times 60 cm (on-axis)
Depth (radiation lengths)	32
Sampling	$\geq 90\%$
Longitudinal segmentation	14 layers ($\simeq 2.3$ rad. lengths each)
Lateral segmentation	~ 1 Molière radius

The DAMPE imaging calorimeter characterized by 14 layers of BGO bars (as represented in figure 3.8), 2.5×2.5 cm² in cross section and 60 cm in length. The total of 336 bars have an hodoscope arrangement with a thickness of 32

radiation length⁸. Each crystal is readout by two Hamamatsu R5610A-01 PMTs; in order to increase the dynamic range 3 dynodes of each PMT are connected to the VA based readout system. The PMTs are coupled to the crystal with optical filters, which have the role to attenuate the scintillation light produced in the BGO.

For electrons and photons, the detection range is 5 GeV – 10 TeV, with an energy resolution of about 1% at 800 GeV.

For proton and ions in the cosmic rays, the expected detection range is 100 GeV – 100 TeV, with energy resolution better than 40% at 800 GeV.

The ground calibration of BGO has been performed using both the data collected in a beam test campaign at CERN (figure 3.9) and cosmic ray data collected from ground. The calibration procedure includes the measurement of the pedestals, the evaluation of the calibration constants from the MIP peaks, the evaluation of the dynode ratios, and the measurement of the bar attenuation lengths.

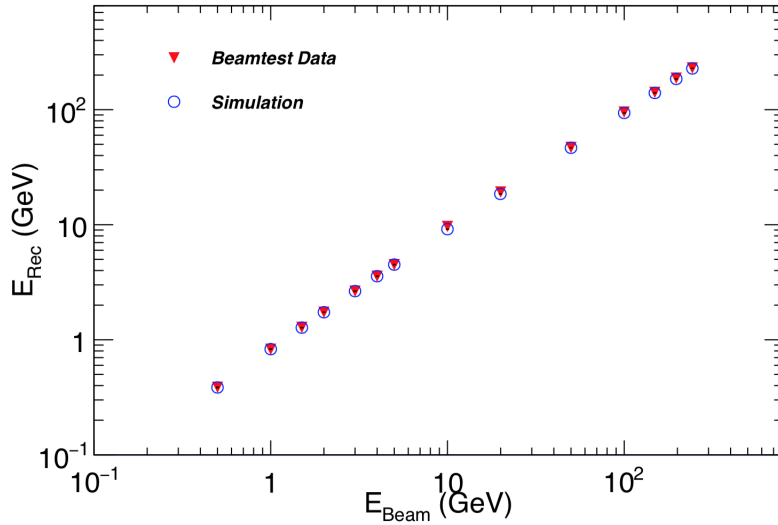


Figure 3.9: Energy reconstructed as a function of the incident energy of the electron beam. Red triangles shows the beam test data, and the open blue circles shows the simulation.

⁸Detailed evaluation of the longitudinal and trasversal containement of the BGO sub-instrument may be found in appendix D.

3.1 The NeUtron Detector (NUD)

The main purpose of the neutron detector is to perform electron/hadron identification, using the neutrons produced by the hadron interactions in the BGO layers. In fact, for a given initial particle energy, the neutron content of a hadronic shower is expected to be one order of magnitude larger than that of an electromagnetic one; once the neutrons are created, they are quickly thermalized in the BGO calorimeter, and the total neutron activity over a few microseconds is measured by NUD.

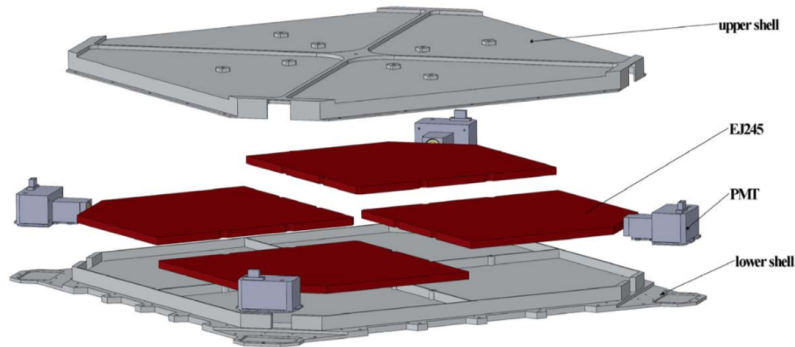


Figure 3.10: Schematic view of the DAMPE NeUtron Detector (NUD) [21].

Table 3.4: NUD designed parameters [21].

Parameter	4 Plastic Scintillators (^{10}B)
Active area	61cm \times 61cm
Energy range	2 - 60 MeV for single detector
Energy resolution ^a	$\leq 10\%$ at 30 MeV
Power	0.5 W
Mass	12 Kg

Notes: ^a σ_E/E assuming Gaussian distribution.

The detector is characterized by four 30 cm \times 30 cm \times 1.0 cm blocks of boron-loaded plastic scintillator, each one wrapped with a layer of aluminum film for photon reflection, anchored in aluminum alloy framework by silicone rubber,

and readout by a PMT. The scintillators are embedded with wavelength shift fibers for optical transmission, in order to reduce the fluorescence attenuation and increase photon collection efficiency; signals are readout by corner-on Hamamatsu R5610A-01 PMTs.



Equation 3.1 describes the process that transforms the neutrons generated⁹ in the BGO calorimeter into γ rays, in turn read by PMTs. These neutron captures are the dominant source of photon generation in the NUD, after $\sim 2 \mu\text{s}$ from the initial calorimeter shower.

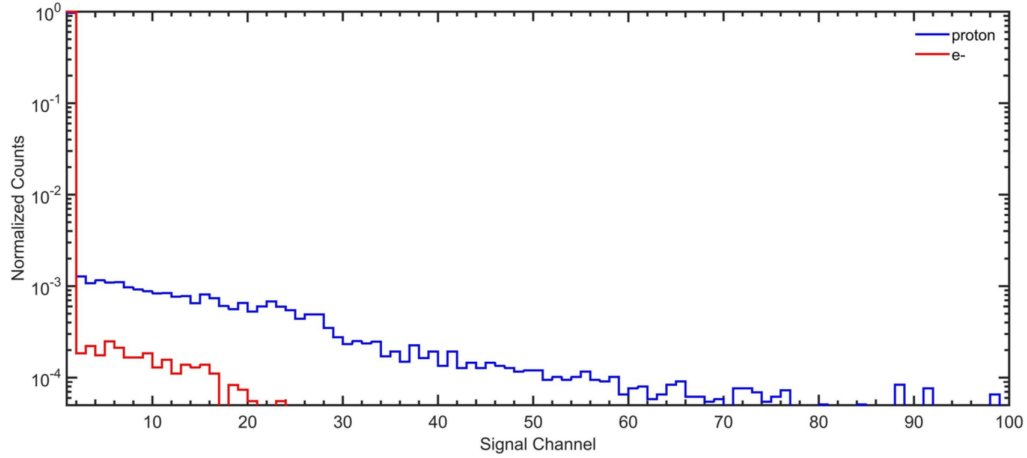


Figure 3.11: NUD signals for protons and electrons with an energy of ~ 150 GeV deposited in the BGO calorimeter (the distributions are normalized to unit area).

Figure 3.11 shows the different signals released by electrons and protons into the NUD detector.

⁹About 600 optical photons are produced in each capture.

3.2 Performing anisotropy measurements with DAMPE

In chapter 3 some of the main characteristics of the DAMPE detector have been analyzed. In this section we are going to describe all the characteristics that make this instrument particularly suited for anisotropy measurements, particularly at high energy.

Respect to other experiments, such as *AMS-02* and *PAMELA*, *DAMPE* is characterized by a bigger geometrical acceptance; this permits to obtain an higher statistic sample with a reduces observation acquisition time.

DAMPE is equipped with a deep imaging electromagnetic calorimeter of 32 interaction lengths X_0 (compared with the 8 X_0 of *Fermi-LAT* and 17 X_0 of *AMS-02*), capable of precise and accurate energy measurements for γ and e^+/e^- up to 10 TeV, with an energy resolution $\leq 1.5\%$ at 800 GeV. All these features permit a detailed study of the measured all-electron and photon spectra in each energy bin.

In section 2.3 have been analyzed the expected anisotropy values for different types of sources; an high rejection power of the proton flux is thus required to reach the goal¹⁰. Thanks to the joint work of its detectors (see 3 for more details) *DAMPE* has an e/p discrimination power of 10^5 , higher respect to the value reached by *Fermi-LAT*.

All these characteristic bestow *DAMPE* as a great candidate to accomplish anisotropy measurements, especially at the higher energies.

¹⁰The proton flux is \sim three orders of magnitude higher respect to the electrons, and from 4 to 5 times higher respect to the positrons (figure 1.1). More details can be found in chapter 1)

Chapter 4

Tools for the anisotropy study

The information on the anisotropy of the arrival direction of cosmic rays can be extracted from the analysis of the so-called "exposure maps", which are the distributions of the arrival coordinates of each event in the selected coordinate frames. The exposure maps contain a dominant level of anisotropy that is induced by the limited exposure to which the experiment has observed different portions of the sky. Areas of the sky with higher exposure contain a larger number of events, and viceversa. This effect results in a background anisotropy, that has to be taken into account when searching for physical anisotropy effects. Therefore, the knowledge of the exposure maps that the experiment would collect in the hypothesis that the flux of cosmic rays is 100% isotropic is of primary importance. It affects, in fact, the level of sensitivity to which an anisotropy can be detected.

This work is based on the development of the techniques for the definition and construction of the "reference" exposure maps to which to data exposure maps have to be compared to determine the level of anisotropy in the data.

A technique to obtain simulated data sky maps, at different energy and injected values of anisotropies (see section 5.1 for the details), has been developed to properly calculate the detector sensitivity in the different situations.

The analysis developed in the context of this work can be applied to real flight data - after definition of the procedures to select the signal events - to evaluate the level of anisotropy or its upper limit by comparison of the data exposure map with the simulated reference maps.

In this chapter the tools developed to perform anisotropy measurements will be described:

- the study of the geometrical factor and the exposition of the detector,
- the realization of reference maps,
- a brief description of the *multipole analysis* technique;
- the development of *template-fit* procedures.

The geometrical factor of the detector, obtained in section 4.2 through MC simulations, is fundamental to correctly evaluate its FoV ¹ and for the exposition study.

The reference maps, as better explained in section 4.4, provide an image of the sky considering the exposition of the detector assuming an isotropic distribution of the cosmic rays. These maps, compared with data, allow to quantify a possible presence of anisotropy, through the application of mathematical tools.

4.1 Galactic and Geographic coordinate systems

When a cosmic ray event is detected by DAMPE, the information on its incoming direction is provided in the so-called "local" coordinate system. However, since any anisotropy in the incoming direction of charged cosmic rays is expected to be correlated with the direction of astrophysical sources with respect to the observer, the most suitable reference coordinate system for the exposure maps are galactic coordinates.

Figure 4.1 is an artistic representation of the galactic coordinate reference system, used in many of the following maps. The Sun is fixed in the center of the coordinate system, the primary direction is aligned with the approximate center of the Milky Way and the fundamental plane, parallel to the galactic plane, is moved north.

¹Field of View

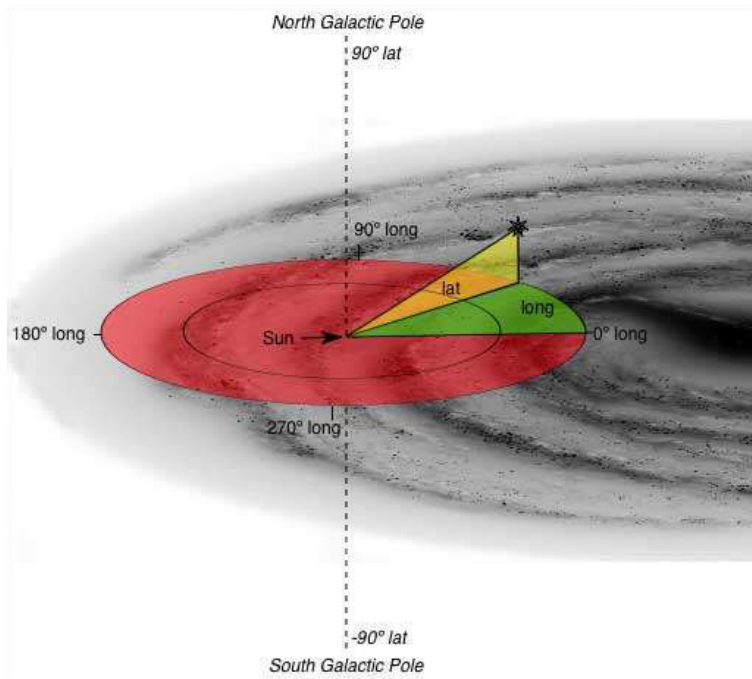


Figure 4.1: Representation of the galactic coordinate system.

The longitude l measures the angular distance of an object eastward along the galactic equator from the galactic center, while the longitude b measures the angle of an object positioned north or south of the galactic equator, as viewed from Earth. Both l and b are measured in degrees.

To represent the orbits of the detector, or the mean acquisition rate, the geographic coordinate system is often used; it is the same method utilized to evaluate the latitude and longitude of a point of the surface of our planet, as explained from the plot in figure 4.2.

A set of C/C++ functions, part of the *DAMPE* collaboration software, have been used to transform the directions of the incoming particles from the local frame of the detector to galactic coordinates, taking into account the direction pointed by the satellite, expressed in galactic coordinates and the time-dependent position of the satellite, expressed in geographic coordinates.

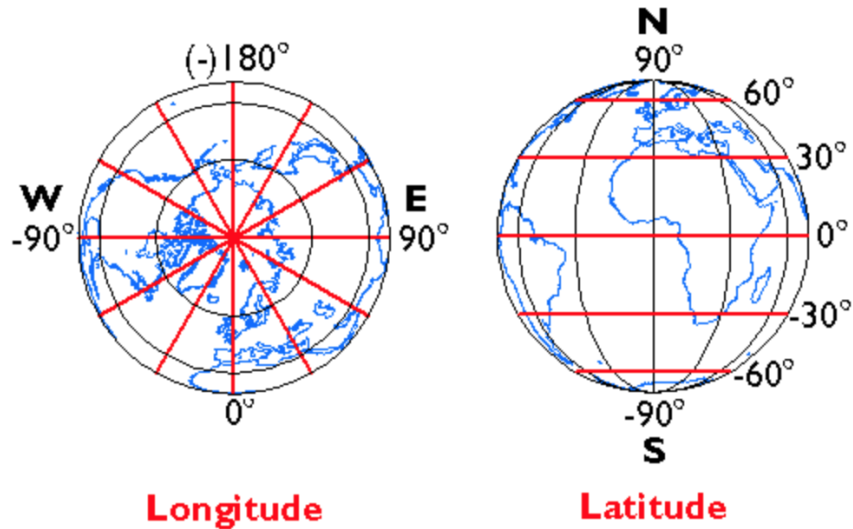


Figure 4.2: Representation of the geographic coordinate system.

4.2 The acceptance of the DAMPE experiment

The portion of the sky observed by the detector is determined by its opening angle and its dimension. These two factors are quantified by the so-called "acceptance" of the detector. The acceptance of a detector is usually quantified by MonteCarlo simulations of the detector geometry and of the interactions of the particles with the detector material. For this sensitivity study, we have produced a preliminary estimation of the detector acceptance by a simple MC simulation in which:

- we assume that DAMPE detects all and only the cosmic rays whose track crosses the upper and lower plane of the BGO calorimeter; in fact, even if the STK dimensions are larger than to the BGO ones, particle tracks without associated energy measurements are unusable. The detector is thus simplified as a parallelepipedon, having the same dimensions as the DAMPE BGO calorimeter;
- we neglect the interaction of the particles with the detector material, assuming that most of the interesting events do not fragment in the PSD or STK and that the direction of the shower reconstructed in

the BGO calorimeter corresponds to the real incoming direction of the cosmic ray.

The geometrical factor is an important and specific characteristic of each particle experiment, connecting the particle counting rate with the spectral intensity.

$$C(\vec{x}) = \int_S d\vec{\sigma} \cdot \hat{r} \int_{\Omega} d\omega \int_0^{\infty} dE \times \sum_{\alpha} \epsilon_{\alpha}(E, \vec{\sigma}, \omega, t) J_{\alpha}(E, \omega, \vec{x}, t) \quad (4.1)$$

Equation 4.1 express a telescope counting rate of particle as function of the observation time t , its surface S and the direction of the incoming particles \hat{r} , the solid angle ω explored, the efficiency ϵ_{α}^2 and the spectral intensity J_{α} [22]. Several simplifications and approximations may be applied to equation 4.1, making the analitic calculation simpler. In the case of a simple geometric shape as that described before, it is even possible to provide an analytical estimation of the detector acceptance.

The geometrical factor has been computed using a Monte Carlo simulation based on a simplified geometry of the detector, represented in figure 3.1, comparing the obtained results with the analytic calculations.

$$G = \pi S \frac{N_{acc}}{N_{gen}} \quad (4.2)$$

$$G(\theta, \phi) = \pi S \cos \theta \frac{A(\theta, \phi)_{sel}}{A(\theta, \phi)_{gen}} \quad (4.3)$$

Equation 4.2 is used in the MonteCarlo simulation to compute the integrated geometrical acceptance; N_{acc}/N_{gen} is the ratio of the events crossing the detector respect to the total sample, while S is the surface of the generating plane.

² α refers to the specific particle type; the efficiency, infact, highly depends on the particle analyzed.

Equation 4.3 represents the differential geometrical acceptance, expressed in function of the angles θ and ϕ in the local frame of the detector; $A(\theta, \phi)_{sel}$ is the selected distribution of events crossing the simple geometry, while $A(\theta, \phi)_{gen}$ is the distribution of the whole generated events. S , as in the previous case, is the surface of the generating plane.

In all these calculations we are supposing an isotropic flux of the cosmic rays; systematic uncertainties eventually present need to be discussed during the data analysis procedure even if significant discrepancies are not expected due to the small value of the expected anisotropy.

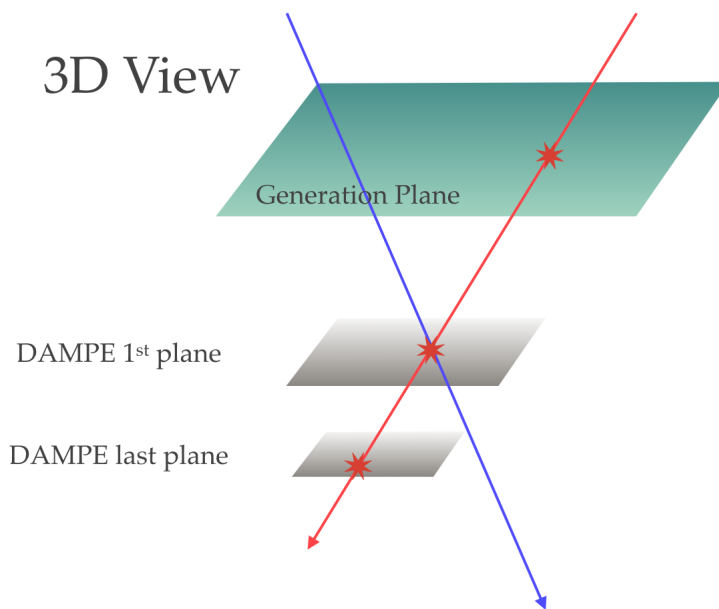


Figure 4.3: Schematic view of the general simulation process and DAMPE's simplified geometry.

Figure 4.3 is a sketch of the MC simulation, also including the used detector simplified geometry. The figure includes the representation of a general generation plane, used to generate the particles, than propagated to the detector layers.

The graph in figure 4.4 is a 3D representation of the differential acceptance, obtained with the Monte Carlo simulation. The graph clearly shows a periodic structures in $\cos(\theta)$ and ϕ angles in the local reference frame describing the incoming direction of a particle; this is the result of the rectangular profile of the detector inserted in an environment where cosmic rays are propagated using spherical coordinates.

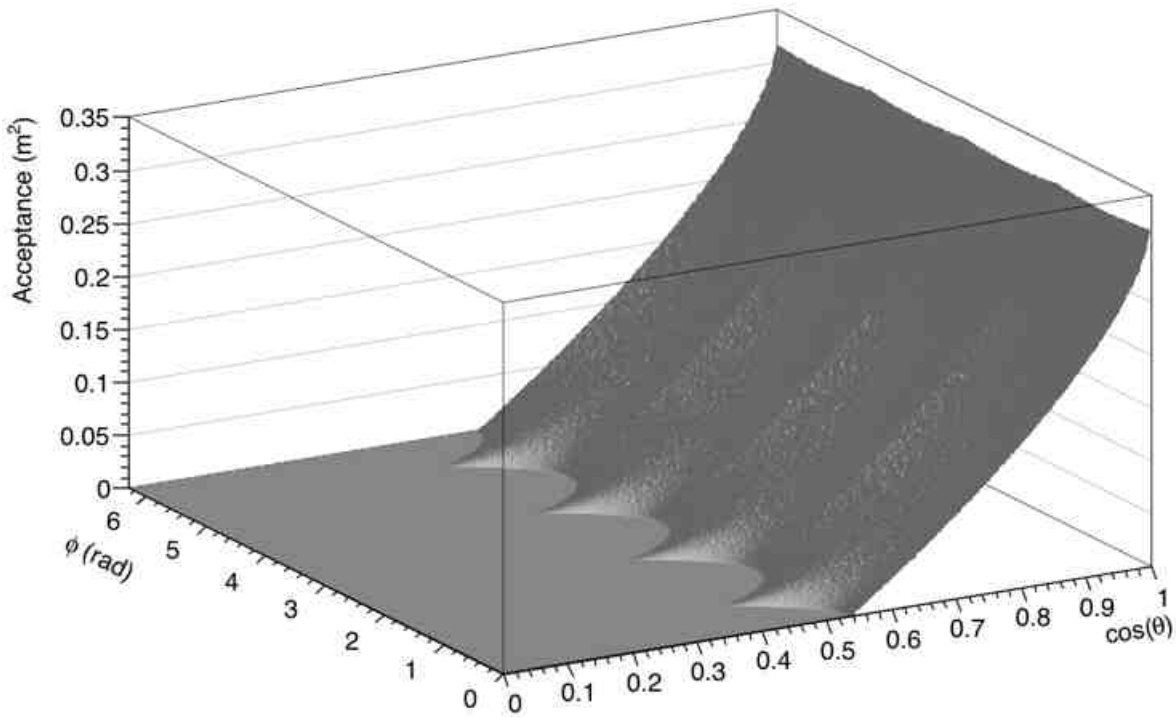


Figure 4.4: Lego plot of the differential acceptance in $\cos(\theta)$ and ϕ , angles in the local reference frame describing the incoming direction of a particle.

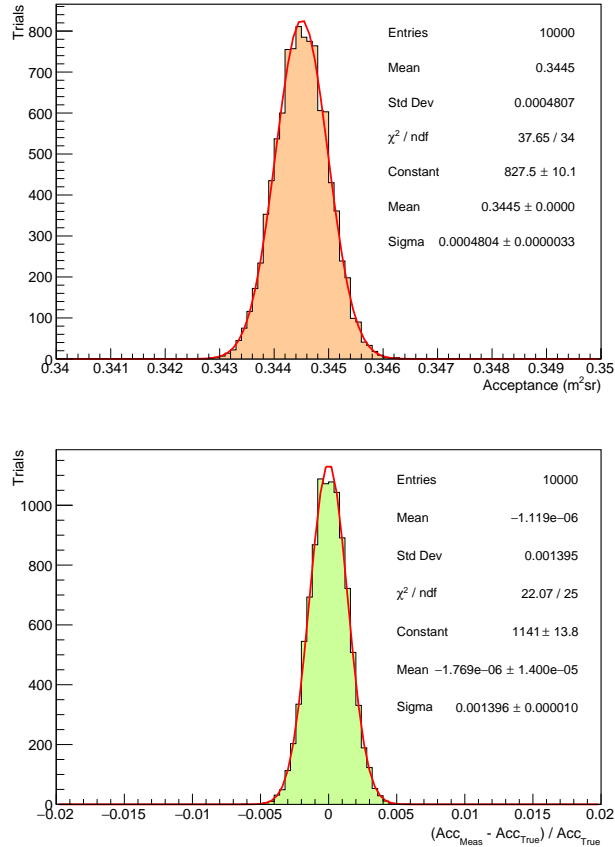


Figure 4.5: **(top)** Distribution of the geometrical acceptance of the detector. **(bottom)** Distribution of the relative difference between simulated geometrical acceptance and the analytic one.

Figure 4.5 show the main results of the Monte Carlo simulation: the geometrical acceptance (top graph) and the relative difference with its analytic value (bottom graph). The acceptance computed in our approximation is compatible with the geometrical factor shown in table 3.1³, confirming that the assumptions are reasonable and verified.

More details and graphs regarding the toyMC simulations may be found in appendix E.

³Considering that no physical interactions between particles and the detector have been considered (toyMC simulation).

4.3 Calculation of DAMPE exposure

To calculate the DAMPE exposure, the time dependent information on the satellite position and orientation are needed. These are available in the SBI ("Second Based Information") database, that provides information second of data acquisition of the mission. The SBI files contain second based information of the detector and the host satellite, regarding the position, speed, tracking, Earth's magnetic field intensity, the number of detected events, the status of the whole system and the information on the Livetime of the detector. The livetime, defined as $1 - \text{deadtime}$, defines the fraction of time in which the detector is able to record the trigger of an incoming cosmic rays and it has to be taken into account in the definition of the reference maps.

The exposure of the detector may be obtained reading the SBI files and extracting the information regarding the position and tracking; DAMPE was launched into a sun-synchronous orbit at the altitude of 500 Km, expecting to reach the whole sky coverage in 4 years [21].

During its mission, DAMPE will not observe the sky homogeneously, due to its orbits and the limited field of view (read section E for the details regarding the geometrical factor).

In this work the period ranging from 27th December 2015 to 28th June 2018 has been considered, excluding the calibration and detector's down times.

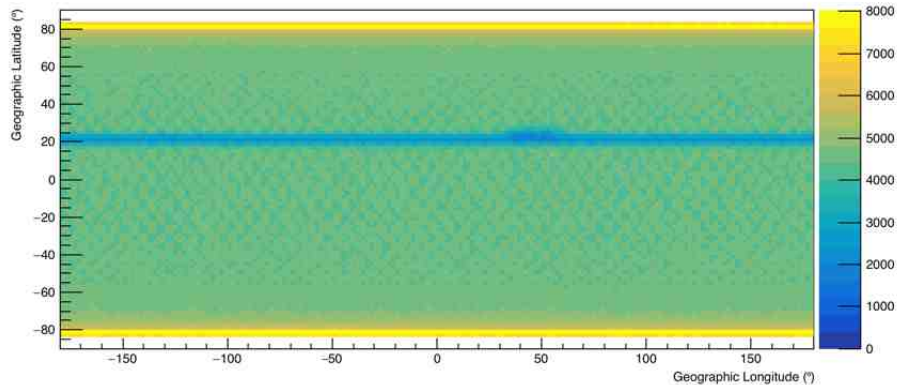


Figure 4.6: Orbits of the the host satellite in geographic latitudes.

Figure 4.6 represents the orbits of the host satellite in geographic latitudes. Each entry in the histogram represent 1 second of the data acquisition. The satellite spends large fraction of its time in the northern geographic poles. The missing time at latitude 20° is due to calibration of the detector and data acquisition reset, that is always done in that region.

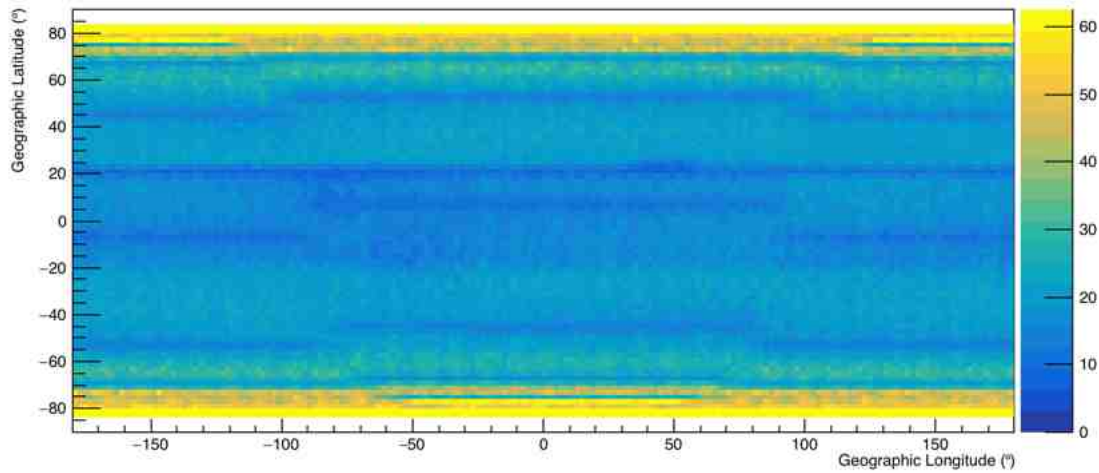


Figure 4.7: Acquisition rate of the detector, in Hz, as function of the galactic coordinates.

The graphs in figures 4.6 and 4.7, obtained considering a period of 914 days, represent respectively all the orbits of the satellite (the typical orbit pattern is visible) and DAMPE's acquisition rate, both in function of the geographic coordinates.

The rate visible in figure is coherent with the expected result; considering the geomagnetic-cutoff, more intense at latitudes closer to zero, the number of triggered particles at the higher latitudes is expected to be bigger.

4.4 Realization of reference maps

Due to exposition-related phenomena (as explained in section 4.3) a perfectly isotropic sky measured by *DAMPE* appears to be anisotropic; this has to be considered in the building process of the reference maps. Several different techniques may be used for this purpose, using Monte Carlo procedures (as proposed in this work) or directly the acquired data (for example *shuffling* techniques [23]).

MC techniques provide an high customizable and scalable procedure; the reference maps are obtained considering both the position and the tracking of the detector, information obtained from the *Second Based Information* (SBI) DAMPE files. [17]. Here the details of the procedure:

- the telemetric information of the satellite in the target time interval is extracted from the SBI database;
- for each second, a number N of events, the product of a fixed number of events⁴ k multiplied for the *live-time* of the detector are randomly extracted from the event distribution, that is the distribution of the incoming direction of the incoming cosmic rays, expressed in function of the local variables $\cos(\theta)$ and ϕ , previously obtained through MC simulations in section 4.2. Considering the high number of events produced, a Mersenne and Twister random generator has been used, implemented through the class *TRandom3* of the ROOT framework: `ROOT::Math::TRandomEngine TRandom3();`
- the events so obtained are then propagated in galactic coordinates, building the reference sky map. Custom C/C++ functions, part of the DAMPE collaboration software, have been used for the transformation from the local reference frame of the detector to galactic coordinates.

Figure 4.8 is the final product of this process; the plot, representing an highly-anisotropic sky, highlights the importance of considering the exposure of the detector. Similar results have been obtained using a slightly different approach: for each second N events, equal to the mean acquisition rate τ , are

⁴Several different values for k have been explored: 5, 10, 50, 100, 500, 1000. In order to minimize statistical fluctuations on the final map, $k = 1000$ is chosen as default value from now on.

extracted from the events distribution. τ is calculated considering the same SBI files and the satellite position in geographical coordinates (figure 4.7).

The reference isotropic sky maps can also be directly obtained using the data; however with respect to the Monte Carlo simulations, more complex procedures, not considered in this work, are required. The *shuffling* technique is one of the most used; it consists in the random exchange of the cosmic rays arriving directions from a data sample, obtained considering a certain sky portion.

This procedure, usually applied to the photons analysis, cannot be directly used in case of charged cosmic rays due to their diffusive motion; in that case, infact, large scale anisotropies may still be present in the final maps.

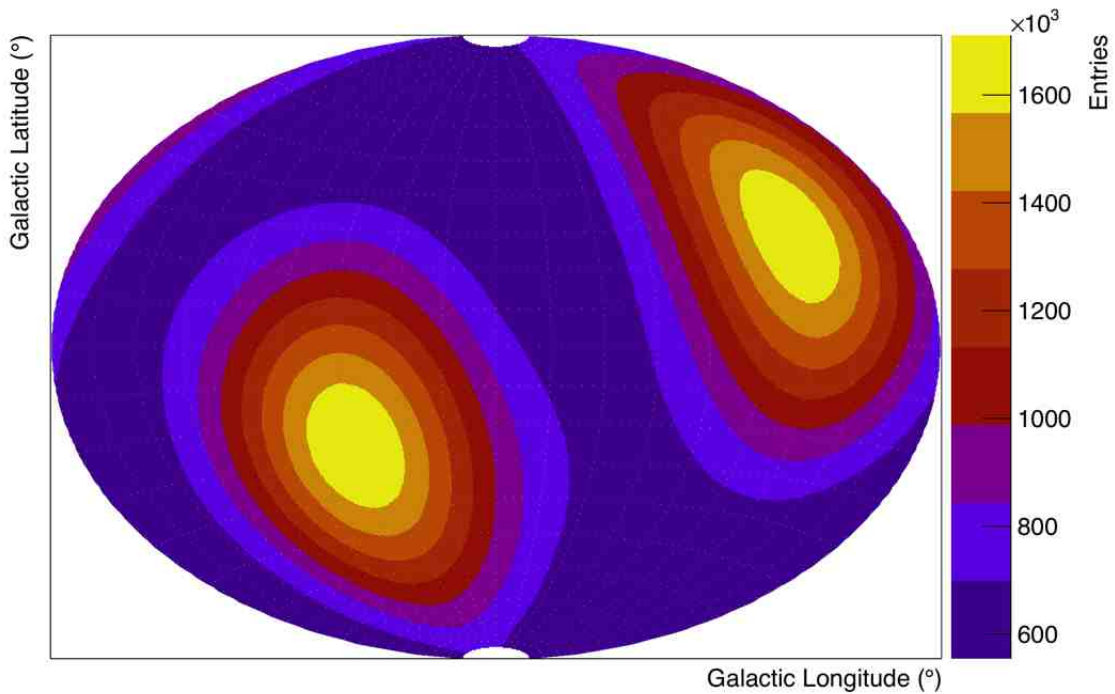


Figure 4.8: Reference isotropic high statistic sky map. For the representation the Aitoff projection has been used.

Figure 4.8 represents the high statistic isotropic reference sky map⁵; while it will be used by the template-fit procedures to extract the anisotropy parameters (see section 4.6 for the details), the event statistics should be sufficiently high to ignore any kind of statistical fluctuation. More reference isotropic maps can be found in appendix F.1.

The yellow hot-spots, clearly visible in the map, represent the zones with the highest particle count; these points correspond to the crossing point of the various orbit, as may be seen in figure 4.9. Differently from figure 4.6, in figure 4.9 just few satellite's orbits are shown.

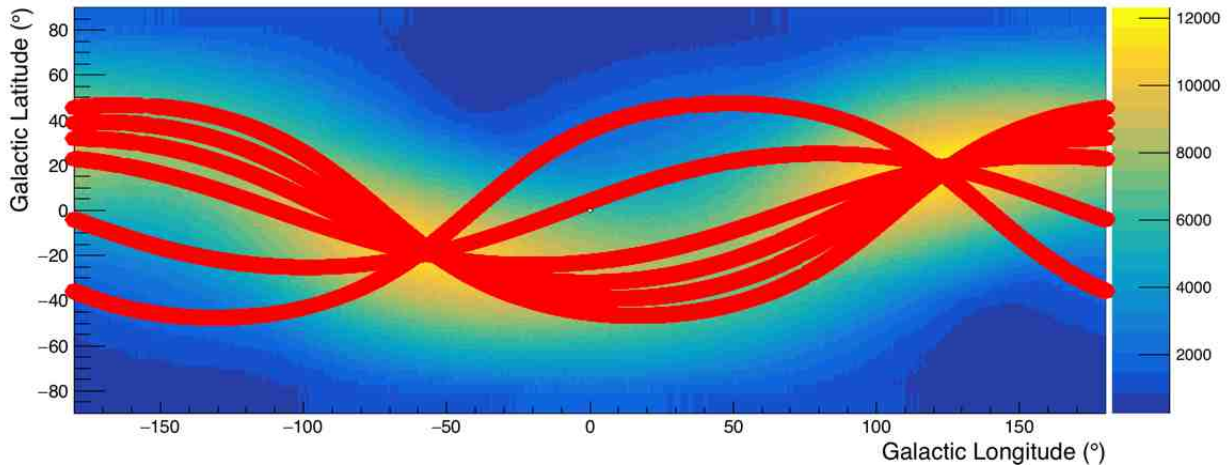


Figure 4.9: Isotropic reference map, obtained considering 9 hours of data. Red thick lines highlight tracking of DAMPE.

⁵Obtained setting $k = 1000$.

4.5 Multipole Analysis

The multipole analysis for measurement of the anisotropy in the sky maps is described in this section.

The search for anisotropy can be powerfully addressed using multipole analysis, method that we're going to deeply describe in this chapter. After a first mathematical introduction to the argument, few simplification will be introduced for application on the data analysis. At the end of this chapter a theoretical model to efficiently describe dipoles will be provided.

Multipole analysis can be mathematically described as a special case of a series expansion, conceptually identical to the Taylor series; as this one, also multipole expansion can be used to represent a particular function as an indefinite sum of powers of basis function. Truncating this expansion at a certain order, an approximation of the original function can be provided; the more terms will be included in the definite series the more accurate will be the final approximation.

Since dealing with an high number of elements could be computationally heavy, even if theoretically could lead to a better estimate of the final result, choosing an appropriate base of periodic functions permit to obtain a good result with a significantly lower number of steps.

A multipole expansion is a series expansion of a function defined on the surface of a sphere; this is particularly useful considering that we have to deal with the distribution of the cosmic rays arrival directions, that's a projection on the surface of the celestial sphere.

In such a series expansion each single term can be identified belonging to certain multipole orders like monopole, dipole, quadrupole and so forth. Figuratively spoken they correspond in the electromagnetic case to the field generated by of one, two or four charges appropriately arranged.

As basis for the expansions, spherical harmonics Y_l^m have been chosen:

$$Y_l^m(\theta, \phi) = \sqrt{\frac{2l+1}{4\pi} \frac{(l-m)!}{(l+m)!}} P_l^m(\cos \theta) e^{im\phi} \quad (4.4)$$

Equation 4.4 describes a spherical harmonic of degree l and order m , defined on a unit sphere in spherical coordinates with longitude $\phi \in [0, 2\pi]$ and

colatitude $\theta \in [0, \pi]$, while P_l^m refers to the Legendre polynomial. Being chosen as a base, the orthonormality condition have to be fulfilled:

$$\int_{\theta=0}^{\pi} \int_{\phi=0}^{2\pi} Y_l^m(\theta, \phi) Y_{l'}^{m'*}(\theta, \phi) \sin(\theta) d\theta d\phi = \delta_{ll'} \delta_{mm'} \quad (4.5)$$

$$Y_l^{m*}(\theta, \phi) = (-1)^m Y_l^{-m}(\theta, \phi) \quad (4.6)$$

These functions form a complete basis of the Hilbert space of \mathcal{L}^2 functions, any square integrable function defined on a unit sphere can thus be expanded as a linear combination of spherical harmonics, as expressed in equation 4.7.

$$f(\theta, \phi) = \sum_{l=0}^{\infty} \sum_{m=-l}^l a_l^m Y_l^m(\theta, \phi) \quad (4.7)$$

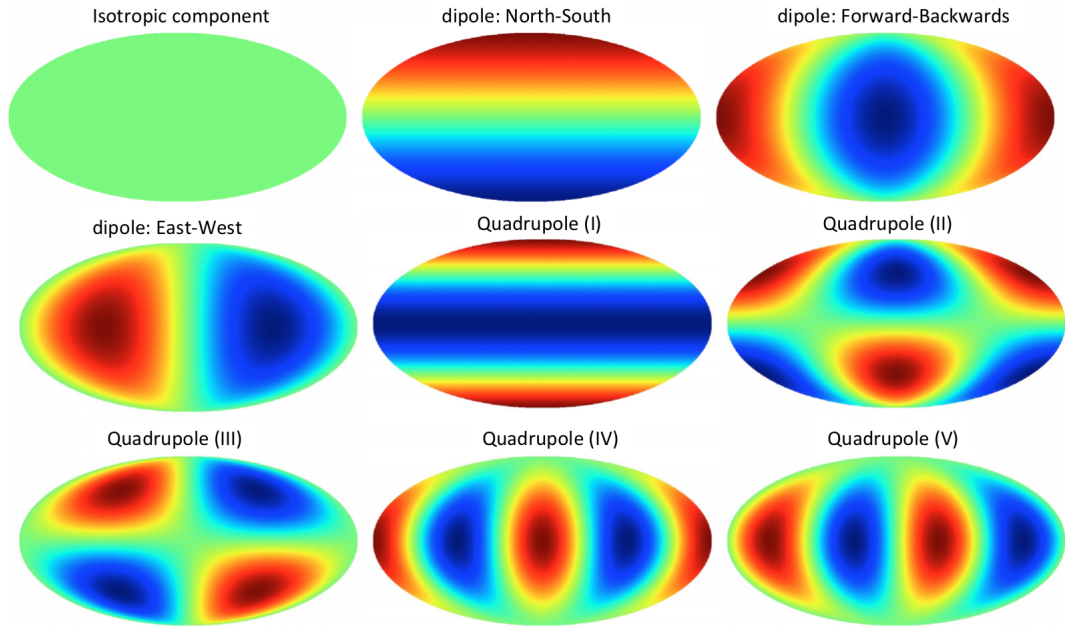


Figure 4.10: Maps representing different analytic multipole orders [1]. The color scale is linear.

From the series shown in equation 4.7, a_l^m represents the expansion coefficients, whose numerical value will be obtained by *data fitting* procedures (see section 4.6 for more details). Their analytical form can be explicated as follows:

$$a_l^m = \int_{\theta=0}^{\pi} \int_{\phi=0}^{2\pi} Y_l^{m'*}(\theta, \phi) f(\theta, \phi) \sin(\theta) d\theta d\phi \quad (4.8)$$

For the search of anisotropies in the charged cosmic rays, we restrict ourself in the search for dipole components, qualitatively corresponding to asymmetries between two sides of the galactic sphere. To this aim, the relevant spherical harmonics reduce to:

$$Y_0^0(\theta, \phi) = \sqrt{\frac{1}{4\pi}} \quad (4.9)$$

$$Y_1^0(\theta, \phi) = \sqrt{\frac{3}{4\pi}} \cos(\theta) \quad (4.10)$$

$$Y_1^1(\theta, \phi) = -\sqrt{\frac{3}{8\pi}} \sin(\theta) e^{i\phi} \quad (4.11)$$

$$Y_1^{-1}(\theta, \phi) = \sqrt{\frac{3}{8\pi}} \sin(\theta) e^{-i\phi} \quad (4.12)$$

To derive the four corresponding expansion coefficients, the appropriate spherical harmonics are fitted to the data sky maps using the least squares method; for this reason we are usual to refer to these spherical harmonics as "template functions".

The entire data analysis process we will perform to extract information regarding anisotropy dipoles, is based on particles count ratio, which is for sure a non imaginary number. Spherical harmonic functions we already presented, at the contrary, are complex functions, this introduces an unnecessary level of complexity.

We're now going to introduce few simplification to the multipole expansion, starting with coefficients and including harmonic functions:

$$a_l^{-m} = (-1)^m a_l^{m*} \quad (4.13)$$

$$s = Y_0^0(\theta, \phi) \quad (4.14)$$

$$p_z(\theta, \phi) = Y_1^0(\theta, \phi) \quad (4.15)$$

$$p_x(\theta, \phi) = \sqrt{\frac{1}{2}}(Y_1^{-1}(\theta, \phi) - Y_1^1(\theta, \phi)) \quad (4.16)$$

$$p_y(\theta, \phi) = i\sqrt{\frac{1}{2}}(Y_1^{-1}(\theta, \phi) + Y_1^1(\theta, \phi)) \quad (4.17)$$

All the simplification introduced permitted to obtain real spherical harmonics functions, whose can be represented in a two-dimensional sphere, as figure 4.12 represents.

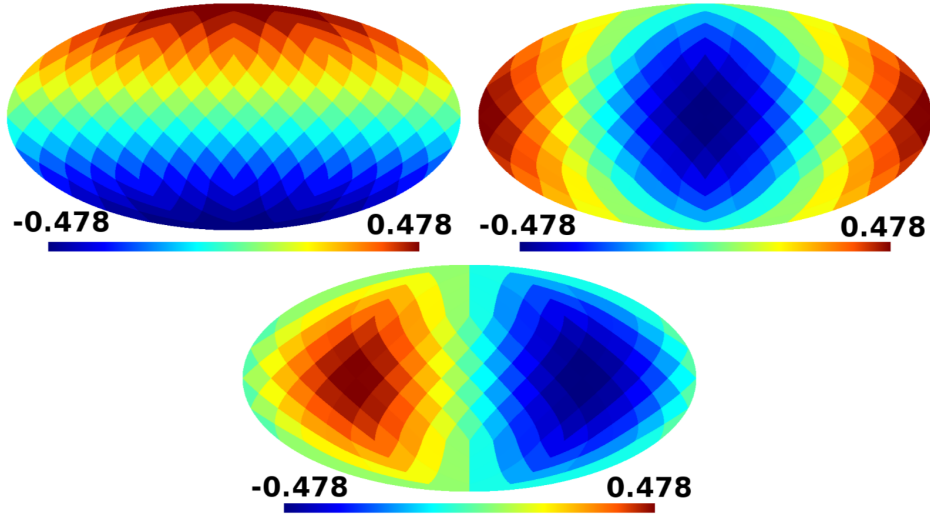


Figure 4.11: Projection of the real harmonic functions $p(\theta, \phi)$ in a *HEALpix* grid [24]. From the top left in clockwise direction there is the *north-south*, *forward-backward* and *east-west* dipole direction [1]. A linear combination of these three maps can describe any dipole.

These functions will be used as templates for the fit procedures, as explained in subsection 4.6.

Figures of section 4.4 and 4.3, together with the ones in appendix F show a different domain, respect to the default one, for the variable of the harmonic functions; in this work $\theta \in [-\pi/2, \pi/2]$ and $\phi \in [-\pi, \pi]$. In order to properly fit the data sky maps a series of variable transformations are needed:

$$\begin{aligned}\theta' &\rightarrow \theta - \frac{\pi}{2} \\ \phi' &\rightarrow \phi - \pi\end{aligned}\tag{4.18}$$

Considering these variable transformations, reported in equation 4.18, the modified functions eqs. (4.14) to (4.17) can be written as:

$$s = \frac{1}{\sqrt{4\pi}}\tag{4.19}$$

$$p_z(\theta, \phi) = -\sqrt{\frac{3}{4\pi}} \sin(\theta)\tag{4.20}$$

$$p_x(\theta, \phi) = \sqrt{\frac{4}{4\pi}} \cos(\phi) \cos(\theta)\tag{4.21}$$

$$p_y(\theta, \phi) = -\sqrt{\frac{3}{4\pi}} \cos(\theta) \sin(\phi)\tag{4.22}$$

The weightings, or expansion coefficients, of eqs. (4.19) to (4.22) are represented as d_1 (*north-south* N-S), d_2 (*forward-backward* F-B) and d_3 (*right-left* E-W); they can be represented in a vector formalism in the following manner:

$$\vec{\rho} = \begin{pmatrix} \rho_{NS} \\ \rho_{EW} \\ \rho_{FB} \end{pmatrix} = \begin{pmatrix} a_0^0 \\ \sqrt{\frac{1}{2}}(a_1^{-1} - a_1^1) \\ \sqrt{\frac{1}{2}}i(a_1^1 + a_1^{-1}) \end{pmatrix}\tag{4.23}$$

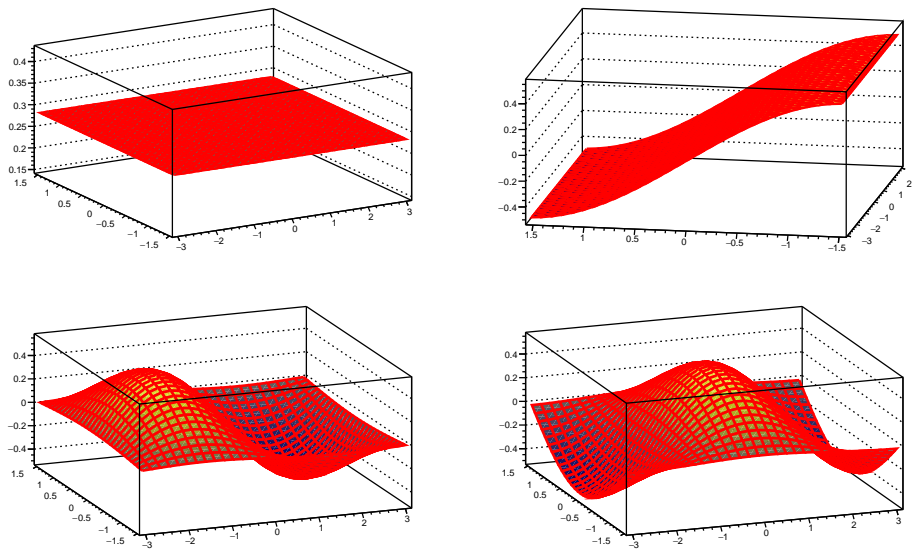


Figure 4.12: Representation of the analytic template functions eqs. (4.14) to (4.17), used in the fit procedures. Starting from the upright corner, and proceeding clockwise: N-S Template, E-W Template, F-B Template and the Isotropic Template.

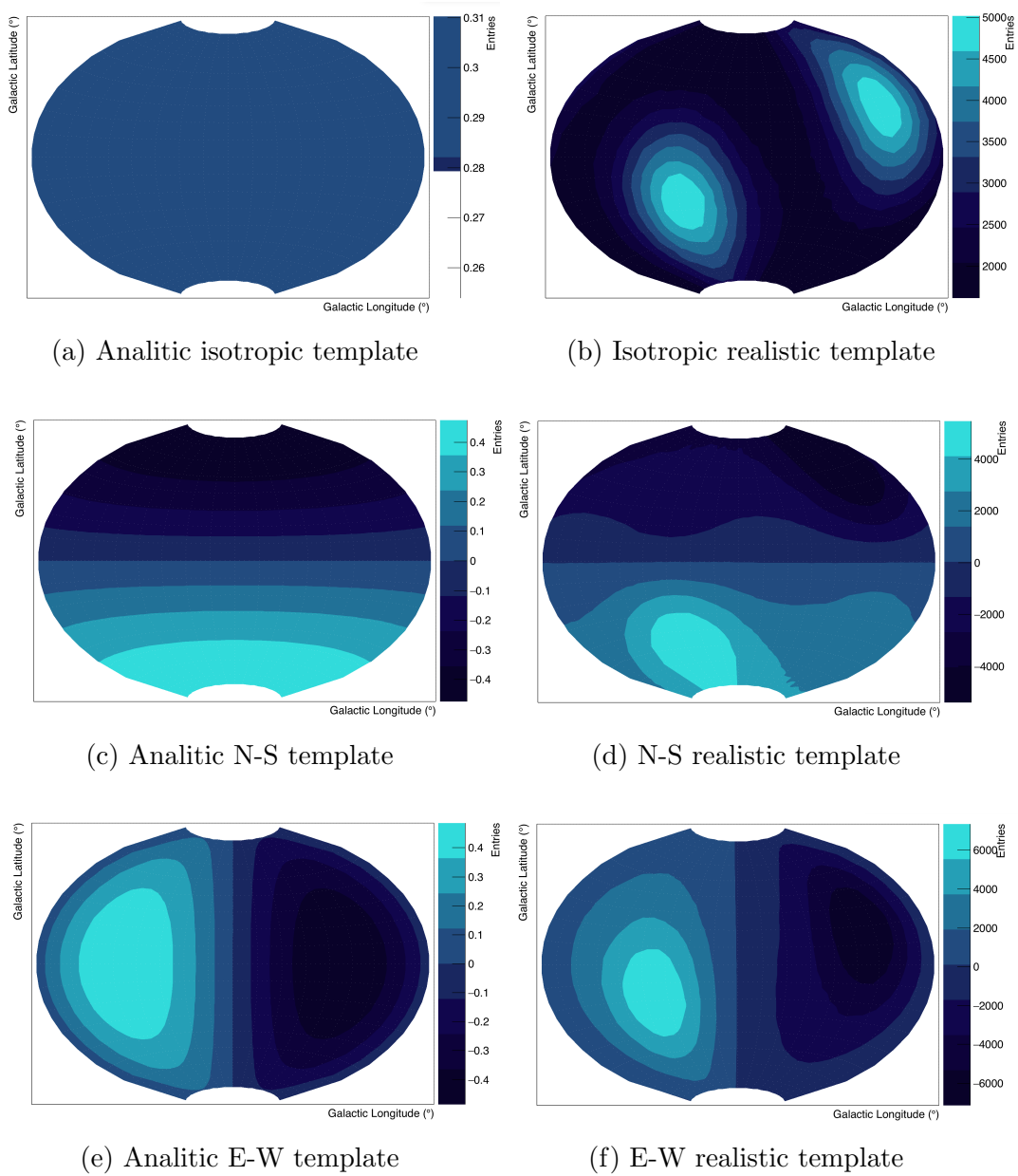


Figure 4.13: Comparison between analytic and realistic templates.

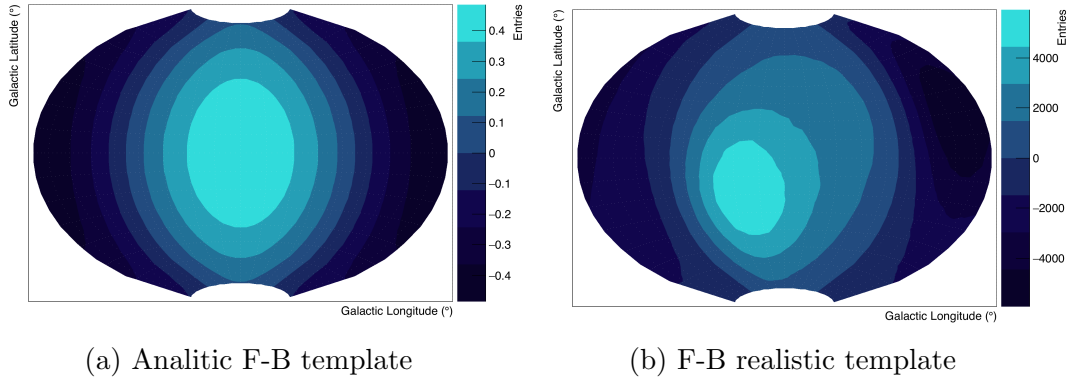


Figure 4.14: Comparison between analytic and realistic templates.

Figures 4.13 and 4.14 show the comparison between the analytic templates for the isotropic and dipole components and the sky reconstructed by DAMPE as it would be exposed to a flux with a distribution that corresponds to such components.

In the next section the procedures to evaluate the dipole anisotropy level δ using the reference maps will be described.

4.6 Fit procedures

Before analyzing the fit procedures, we are going to briefly describe the various maps involved in the procedure:

- ***flat maps***: not representative of the physical problem that we are going to explore, they have been used as a benchmark for the analysis procedure. The analysis of these maps, that do not take into account the exposure of the detector, highly reduce the complexity of the calculations, permitting to evaluate a priori both the fit parameters and their errors.
- ***realistic absolute maps***: these are realistic maps, obtained considering the real exposition of the detector and the various orbits of the satellite. For this reason they are used to extract meaningful anisotropy parameters;

- **realistic relative maps**: like the previous ones, these are realistic maps, but with the characteristics of being able to immediately highlight their anisotropy content. These maps are defined as the relative difference between the realistic and the isotropic reference maps, normalized to the latter one.

$$\Phi = \frac{\phi - \langle \phi \rangle}{\langle \phi \rangle} \quad (4.24)$$

Equation 4.24 describes the technique to build a relative data map Φ , being ϕ the raw data map and $\langle \phi \rangle$ the reference one.

This procedure removes the isotropic content from the maps, showing, on the contrary, the anisotropy dipoles. These maps, even if they have the same information content as the second ones, allow to quickly get an idea of the features of sky represented in the map.

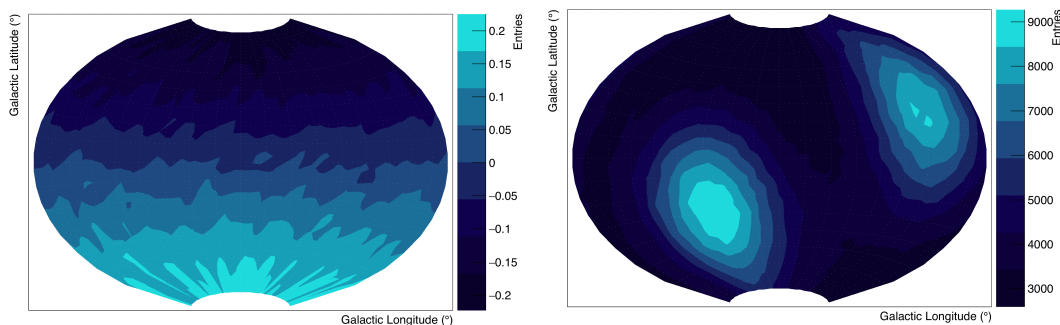


Figure 4.15: **(left)** Simulated relative data map, 10% N-S anisotropy injected. **(right)** Simulated absolute data map, 10% N-S anisotropy injected.

Figure 4.15 shows the difference between the two realistic maps; on the right the absolute map is shown, while on the left the relative one. While the information content is the same for both the maps, the relative map immediately highlights the dipole anisotropy injected, in this case a 10% N-S.

In figures 4.13 and 4.14 both the analytic and the realistic templates are shown; the first ones are used to fit flat and relative maps, while the latter in case of absolute realistic maps.

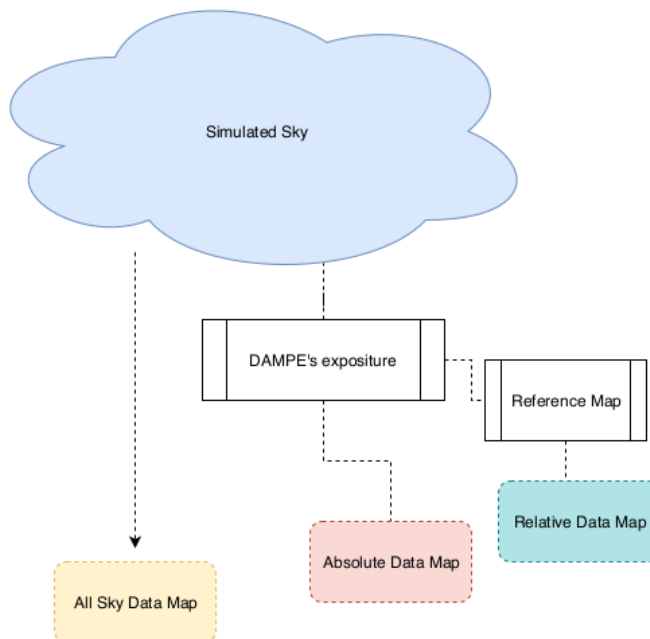


Figure 4.16: Representation of the different fit procedures, explained in this section.

The sketch in figure 4.16 shows the different simulated data maps analyzed with the template-fit technique. See section 5.1 to understand how the simulated maps have been realized.

The fitting procedure minimized the sum of the difference, obtained bin by bin, between the expected (n_{exp}) and observed events (n_{obs}), normalized for the obtained ones:

$$\chi^2 = \sum_i \frac{(n_{i,obs} - n_{i,exp})^2}{\sigma_{i,obs}^2} \quad (4.25)$$

The template-fit procedure considers 4 parameters for the absolute maps, and 3 for the relative ones⁶; labeled as par_j , they resemble the coefficients of the template functions before shown (eqs. (4.14) to (4.17)).

⁶In this case, in fact, the isotropic component is zero by construction.

Writing equation 4.25 we assume the variance on the bin entries σ_{obs}^2 to be poissonian distributed, while the expected number of events is obtained considering the template, as follows:

$$n_{exp,i} = \sum_{j=1}^4 par_j \cdot T_j \cdot d_{w,i} \quad (4.26)$$

Equation 4.26 highlights the function dependence of the number of expected events from the bin number i , the fit parameter par_i and the bin width⁷ $d_{w,i}$. The sum is extended to all the fit parameters, in the same number of the template functions used.

The maps fitted with this procedure have been obtained by a MC simulation, as described in section 5.1; different combination of injected anisotropies have been tested⁸, including a completely isotropic sky, used to evaluate *DAMPE*'s sensitivity at different energy and statistics.

In case of absolute maps, bins with a number of events less than five are excluded from the fit, while for the relative ones only the empty bins were not considered. Differently from the usual, in fact, in this case not only bins with a negative number of observed events are present, but the small percentages of injected anisotropies often determine a poor statistics in many areas of the map.

In order to account these problems, affecting also absolute maps at high energy, different bin width have been used in function of the explored energy. This is particularly important in the simulation of the detector acceptance in function of the time/energy.

Experiments with a bigger geometrical acceptance, such as HERD [25], will be able to detect a larger statistics in the same energy bins.

In case of absolute fit, the norm of the vector in equation 4.23, scaled by the monopole expansion coefficient ρ_{Iso} (which is the isotropic average), provide the value of *delta*, as described by equation 4.27.

⁷Supposed to be the same for all the bins, in this work.

⁸Different anisotropy levels have been explored, as better explained in section 5.1, covering the whole spectrum of expected values (see section 2.3 and [20] for more details): 10%, 0.1% and 1% of the isotropy template.

$$\delta = \frac{I_{min} - I_{max}}{I_{min} + I_{max}} = \frac{|\vec{\rho}|}{\rho_{Iso}} = \frac{\sqrt{\rho_{NS}^2 + \rho_{EW}^2 + \rho_{FB}^2}}{\rho_{Iso}} \quad (4.27)$$

At the contrary, in case of relative fit, the dipole amplitude may be written as $\delta = \sqrt{\rho_{NS}^2 + \rho_{EW}^2 + \rho_{FB}^2}$.

Once the fit parameters, have been obtained, the anisotropy content of the map δ can be finally obtained; this is the physical quantity that we are interested in. This measurement of δ in maps with an a-priori known level of anisotropy is fundamental to verify the correctness and robustness of the method. The same approach can be and will be applied to maps constructed using data collected by *DAMPE* to measure anisotropy content of the sky maps.

The performance of the fit procedure will be shown in the next chapter.

Chapter 5

Simulation tests and detector sensitivity

This chapter includes the description of the simulation tests aimed to verify the analysis technique proposed in the previous chapter, together with the calculation of the detector sensitivity as function of the energy and exposition time. In order to obtain the desired results, a set of realistic simulations have been developed, considering the detector exposure using the *Second Based Information* files (SBI), together with anisotropy injection techniques to realize simulated anisotropy skies.

5.1 Anisotropy injection techniques

In this section we are going to explain the strategy used to simulate anisotropic maps, injecting any dipole combination, of whatever intensity, in the data maps.

Considering the expected anisotropy values for the signal of electrons and positrons produced by nearby pulsars [14, 20], the intensity of the injected dipoles ranges from 10% to 1‰, covering all the wide spectrum of possibilities.

The anisotropic maps are constructed as a weighted linear combination of the isotropic and the 3 dipole components.

$$T_A = W_{Iso}T_{Iso} + W_{NS}T_{NS} + W_{EW}T_{EW} + W_{FB}T_{FB} \quad (5.1)$$

Equation 5.1 describes the general data template, used to build the data map (expressed in galactic coordinates). W refers to the weight of the single dipoles, while T identify the analytic templates. As an example, to build a 10% N-S/E-W data map, the corresponding linear combination is $T_{NS/EW} = 0.8 T_{ISO} + 0.1 T_{NS} + 0.1 T_{EW}$.

As may be noticed, the sum of all the weights is unitary:

$$\sum_i W_i = 1 \quad (5.2)$$

Once the map has been so obtained, a MonteCarlo technique method is used to extract random values from the template to fill the simulated data map. The number events in the whole map follows follows a Poisson distribution, with the average value fixed at the required statistic, determined, as example, by the statistics of data collected in flight.

Maps have been constructed by random number generation from 2D histograms and 2D analytical functions. The results are in agreement.

Figures 5.1 and 5.2 are an example of the described technique; the maps are the combination of 70% of isotropic template and a 10% of all the anisotropic dipoles, as reported by the following equation:

$$T_A = 0.7T_{Iso} + 0.1T_{NS} + 0.1T_{EW} + 0.1T_{FB} \quad (5.3)$$

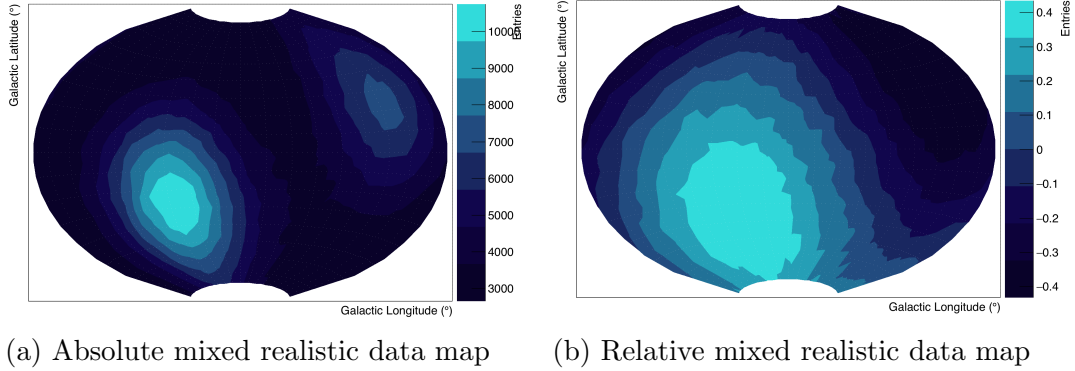


Figure 5.1: **(left)** DAMPE’s simulated (mixed) realistic absolute data map (70% Iso + 10% N-S + 10% E-W + 10% F-B). **(right)** DAMPE’s simulated (mixed) realistic relative data map (70% Iso + 10% N-S + 10% E-W + 10% F-B)

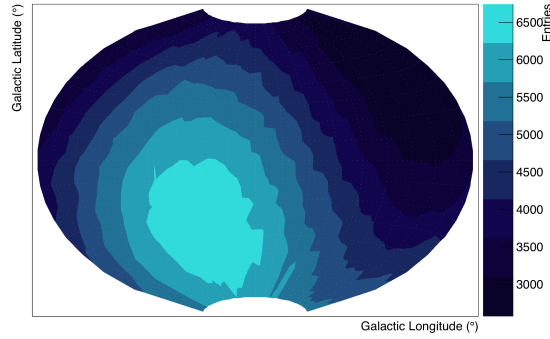


Figure 5.2: Mixed simulated flat data map (70% Iso + 10% N-S + 10% E-W + 10% F-B)

While, as described in section 4.6, the fit process on both the maps in figure 5.1 lead to the same results (as shown in section 5.2), it appears clear that dealing with relative maps immediately highlights the dipole anisotropy that might be present.

More data maps can be found in appendix G.

Maps with different levels of injected anisotropies and different total statistics have been generated using the method described above, and have been used to verify the robustness of the template fit procedure as described in the next section.

5.2 Tests of the fit procedure

In this section we are going to test the template-fit procedure on the simulated maps built with the technique shown in the previous sections.

The flat maps will be used as benchmark for the analysis procedure; later in this section the performance of the analysis on the realistic maps will be presented.

To evaluate the correctness of the results, the fit procedure has been repeated on many statistically independent simulated sky maps. The distributions of the fitted parameters will be shown in the following pages.

We have investigated in particular the features of the following parameters:

- distribution of the fit parameters and of the relative uncertainties;
- distribution of the anisotropy value δ , obtained as described in section 4.6. As explained in the same section, this value is a priori known for the simulated maps; anisotropic maps are used to test the robustness of the procedure: any deviation of the result from the expected, known, values is an indication of a systematic effect in the algorithms.

This section is divided in three subsections: flat maps, absolute realistic maps and relative ones. Independently from the fitted map, relative or absolute, the anisotropy parameters obtained by the fit procedure are always compatible; this means that the physical information contained is the same. The usage of the two types of maps not only validate the results, being used as crosscheck, but proves the absence of systematic uncertainties in the procedure.

5.2.1 Flat map performances

Consider a simulated isotropic map, shown in figure 5.3; it represents an isotropic sky, not considering the exposure of the detector.

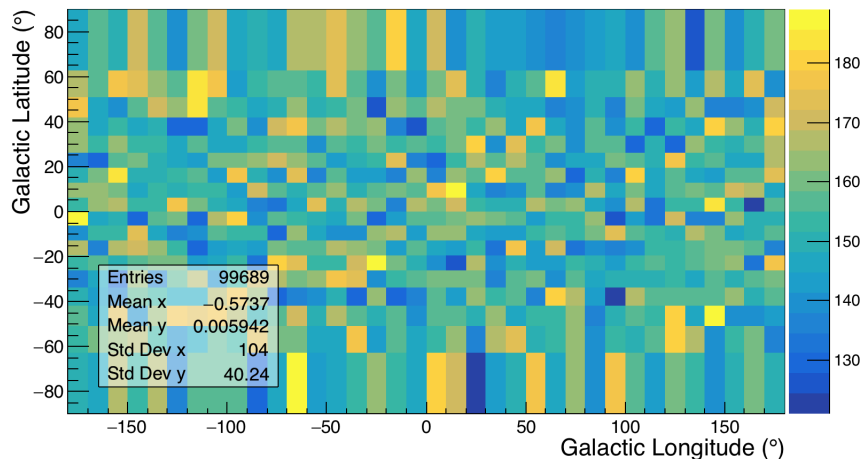


Figure 5.3: Isotropic simulated flat map

To build the map, a number of events $N = 10^4$ has been chosen as representative for the events acquired by *DAMPE* at low energy regime.

Considering the total events of the map, following a Poisson distribution with mean N , and the $n_{tot} = 648$ number of bins, the expected events in each bin n_{exp} is 154. For isotropic maps the error of the isotropic fit parameter can be easily estimated a priori: considering that the poissonian error in each bin σ_b is given by the square root of n_{exp} and that all the bins enter the fit procedure, and the value of the isotropic analytic template, the absolute error σ can be obtained as:

$$\sigma = \frac{\sigma_b}{\sqrt{n_{bin}}} \kappa \quad (5.4)$$

In equation 5.4, κ is the isotropic fit parameter obtained from the fit; it considers both the isotropic analytic template and the bin content of the data map.

The fit procedure has been repeated $3 \cdot 10^4$ times, each time generating a statistical independent data map. The distribution of the isotropic parameter and its uncertainty are represented in figure 5.4. Taking the mean value for the parameter, and applying equation 5.4, the expected value for $\sigma = 1.7$ can be calculated.

The distribution of the parameter uncertainty is compatible with the expected value.

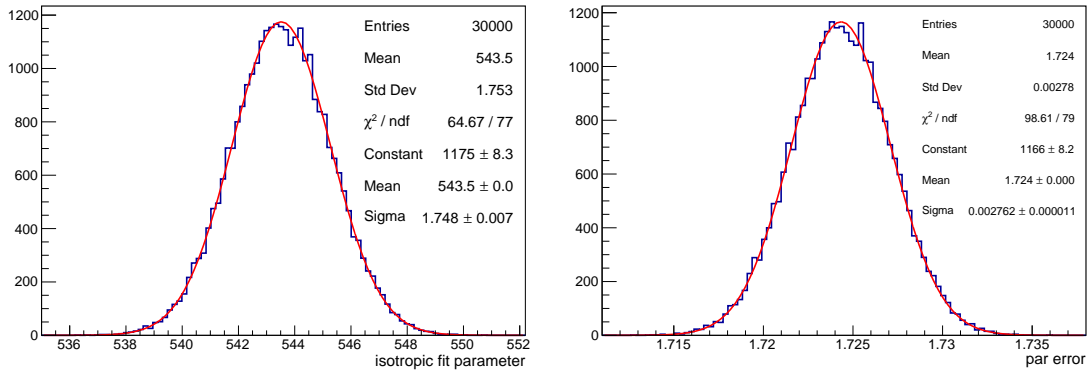


Figure 5.4: **(left)** Distribution of the isotropic fit parameter. **(right)** Distribution of the uncertainty on the isotropic fit parameter. In both graphs the thick red line represents a gaussian fit.

Once obtained the parameters distributions, in case of absolute maps equation 4.27 is used to evaluate the anisotropy value. The isotropic data map in figure 5.3 does not contain any anisotropy dipole: for this reason we expect, for the corresponding anisotropy fit parameters, to be null within their uncertainties.

The plot in figure 5.5 confirms the expectations; here the distributions of the N-S, E-W and F-B parameter are represented. As expected, the distributions all have an average value compatible with 0 and their width is in accord with that of the isotropic parameter (figure 5.4).

The color code introduced in this graph will be maintained until the end of the chapter, if not differently specified.

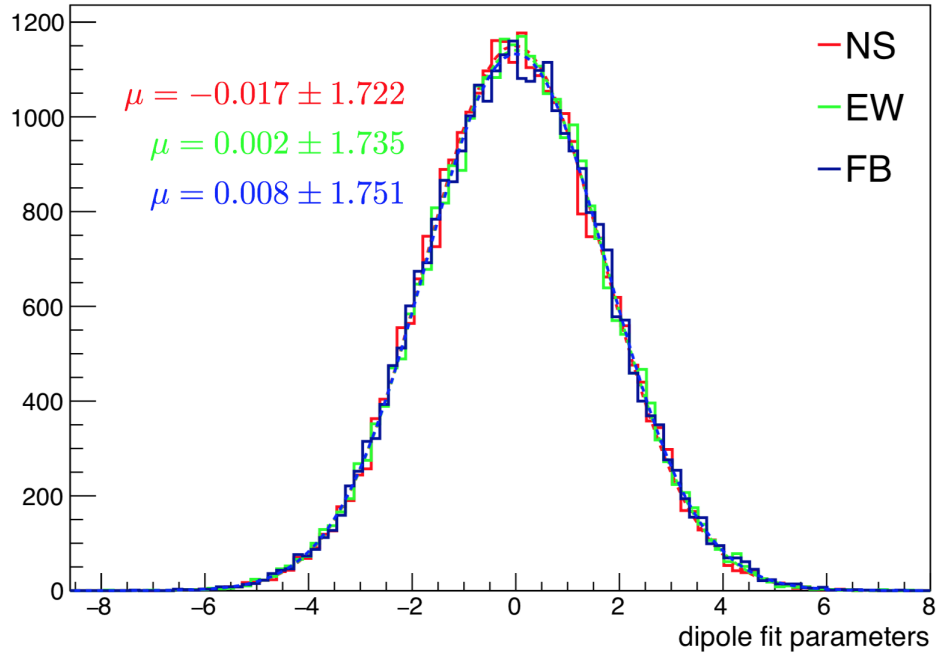
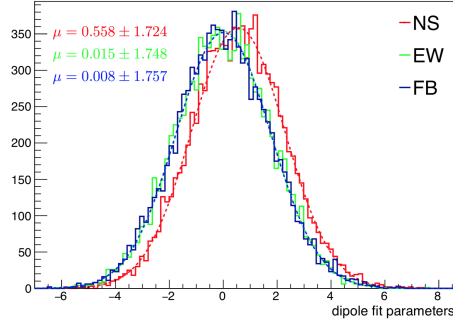


Figure 5.5: Distribution of the N-S (red), E-W (green) and F-B (blue) fit parameters. Gaussian fits have been superimposed to each distribution.

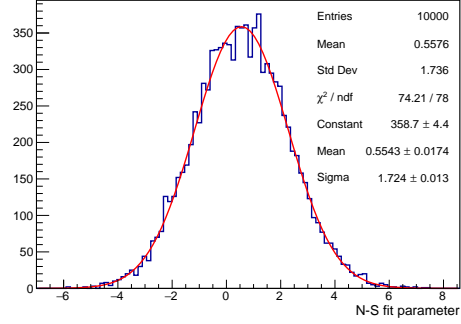
In figures 5.6 5.7 and 5.8 the result of the fit procedures on anisotropic flat maps are presented; in all the cases just one type of dipole anisotropy is injected, with different dipole intensities.

In figure 5.6 the right column represent the distribution of the parameter to which the anisotropy refers, while on the left a comparison with the other components is shown. In the left column, even if the distribution of the parameter associated with the injected anisotropy appears shifted on the right respect to the others, the uncertainties do not permit to distinguish between them. The resolution power of this technique is thus not sufficiently high in the case of 1‰ injected anisotropies.

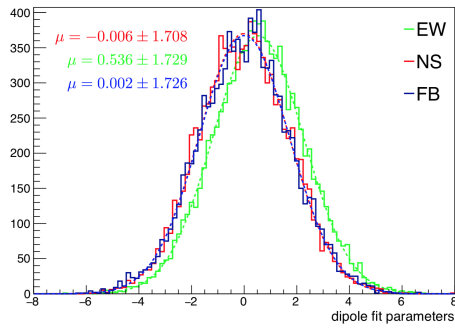
On the contrary this is not true for the 10% and 1% case; figures 5.7 and 5.8 show that the distribution of the fit parameter associated with the injected anisotropy is well separated from the others. This is a first confirmation that the statistics of 10^4 is enough the investigate dipole anisotropies at the level of 1‰, but is not sufficient to accurately identify anisotropies at the level of permille



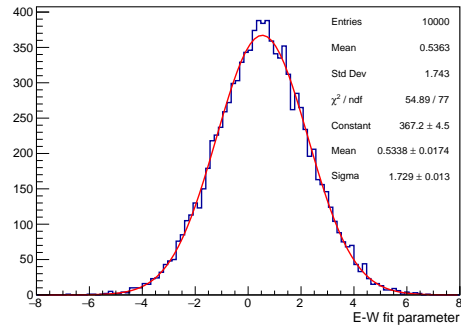
(a) Dipole distribution comparison



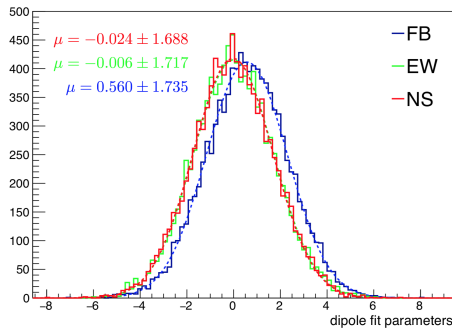
(b) N-S 1%₀ distribution



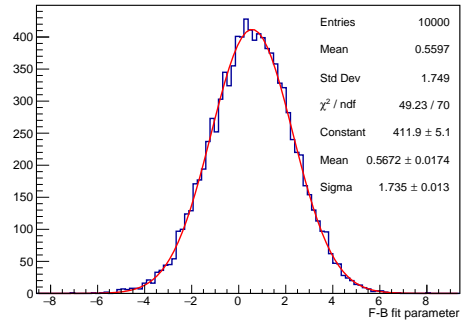
(c) Dipole distribution comparison



(d) E-W 1%₀ distribution

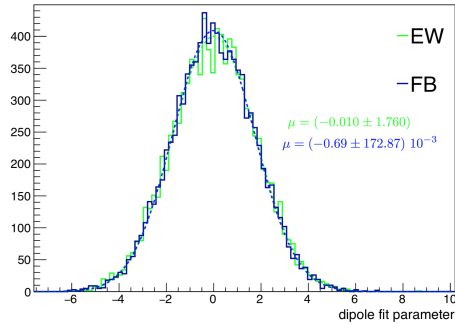


(e) Dipole distribution comparison

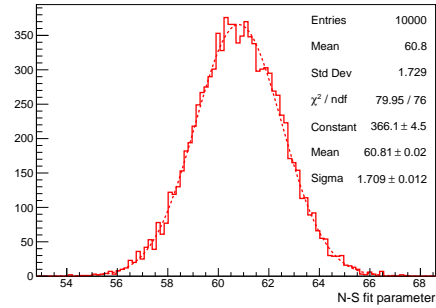


(f) F-B 1%₀ distribution

Figure 5.6: Comparison between dipole fit parameters and isotropic parameter, in case of different anisotropy dipoles of 1%₀ intensity.

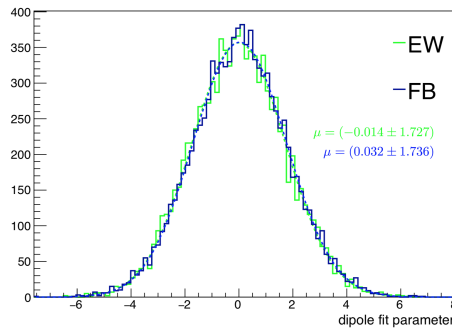


(a) Dipole distribution comparison

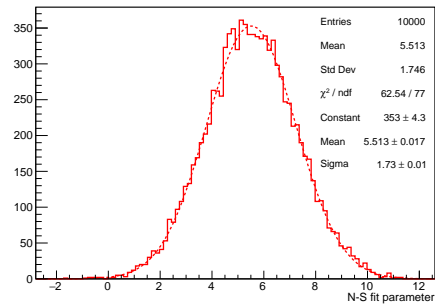


(b) N-S 10% distribution

Figure 5.7: **(left)** Distribution of the E-W and F-B dipole fits parameters for a 10% N-S map. **(right)** N-S fit parameter for a 10% N-S map.



(a) Dipole distribution comparison



(b) N-S 1% distribution

Figure 5.8: **(left)** Distribution of the E-W and F-B dipole fits parameters for a 1% N-S map. **(right)** N-S fit parameter for a 1% N-S map.

As shown by the graphs in the previous page, but more evident in the case of 1% injected anisotropy, the value to which the coefficients tend is the same, no matter the nature of the dipole. This concept is well visible in the graph in figure 5.9; in this case, in fact, three different data maps have been realized, injecting a 1% of N-S dipole anisotropy (red curve), E-W dipole (green curve) and F-B dipole (blue curve). In all the cases, the fit parameter is always the same, no matter what the nature of the dipole is; this proves that the fit procedure is stable also varying the dipole type, maintaining fixed, at the contrary, its intensity.

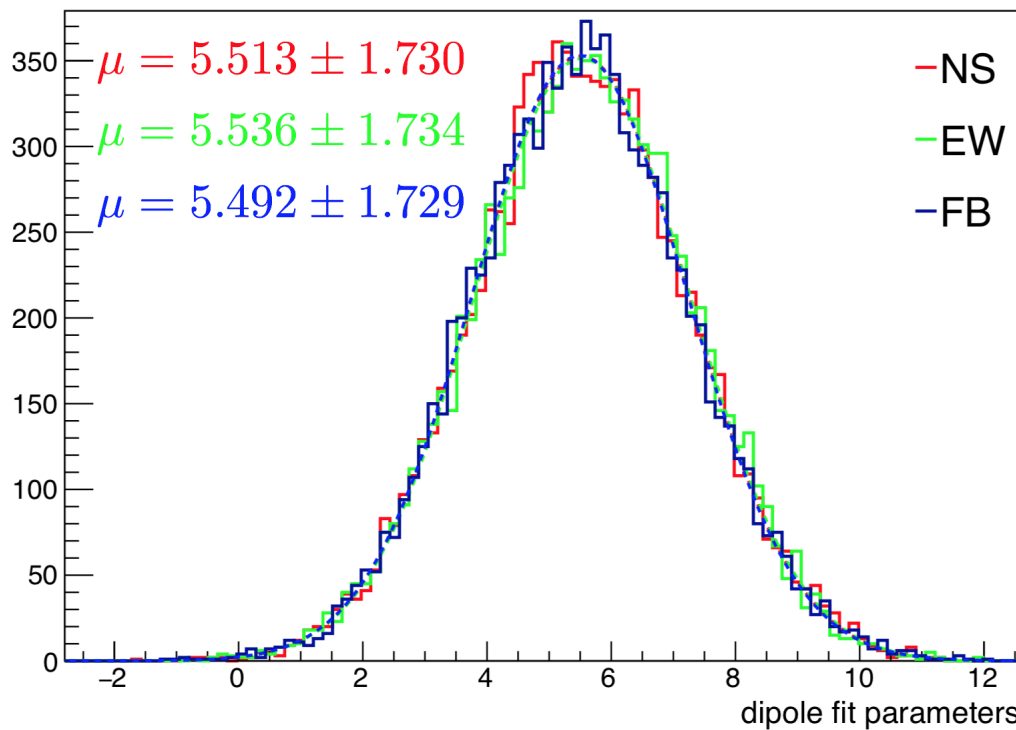


Figure 5.9: Distribution of the N-S (red), E-W (green) and F-B (blue) fit parameters in case of 1% injected map. Gaussian fits have been superimposed to each distribution.

The graph in figure 5.10 represents, at the contrary, the dipole fit parameters for a simulated flat sky map characterized by a 1% of all the dipole anisotropies. The compatibility of the distributions in figures 5.9 and 5.10 is another confirmation of the correctness of the results obtained.

The graph in figure 5.11 represents the distribution of χ^2/ndf on simulated data maps, anisotropic and not; the anisotropic ones contain just a one type of dipole. The distributions, hardly distinguishable, all have the same width and mean value.

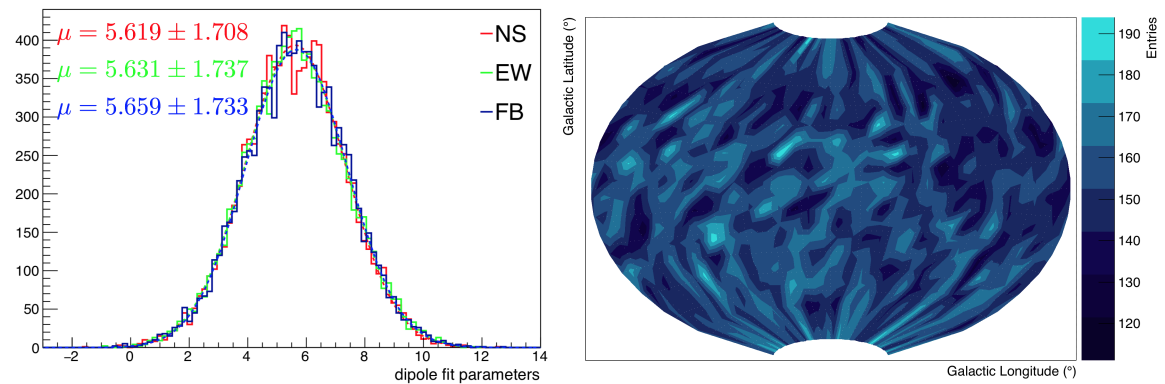


Figure 5.10: **(left)** Distribution of the fit parameters. **(right)** Aitoff projection of the 1% mixed flat data map.

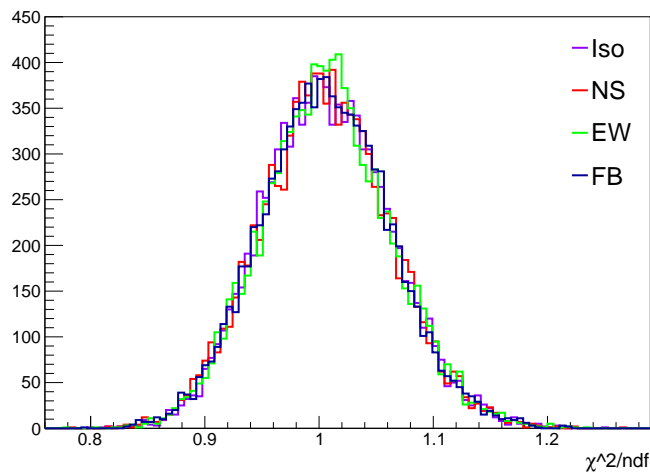


Figure 5.11: Distribution of χ^2/ndf for simulated data maps, differentiated as follows: isotropic (purple), 1% N-S (red), 1% E-W (green) and 1% F-B (blue).

The study of the correlations between the fit parameters is another important question; while they refer to orthogonal harmonic functions we expect a negligible correlation factor between them.

It is interesting to note that the width of the dipole parameter distributions is always compatible with that of the isotropic parameter and the mean values from the fits are compatible with the injected level of anisotropy (a feature that will be present also in the case of realistic maps).

One of the fundamental plots is, without any doubt, the δ distribution; it contains the physical information of the anisotropy content extracted from a certain data map.

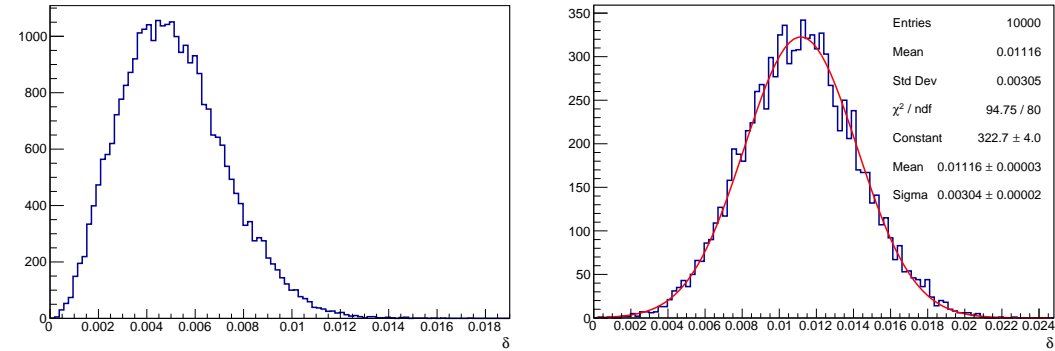


Figure 5.12: **(left)** Distribution of the δ parameter for an isotropic sky map. **(right)** Distribution of the δ parameter for a 1% N-S dipole anisotropy injected.

For the absolute flat maps, the delta distribution is obtained using the equation 4.27. The δ distribution for the isotropic maps, plot on the left in figure 5.12, can be used to evaluate the sensitivity of the instrument to dipole anisotropies; for this scope, however, the realistic maps need to be used. On the right the delta distribution for a simulated map with a 1% of N-S injected anisotropy is shown; the mean value is compatible with the expected one: 0.01. These checks have been performed for different statistics (ranging from 10^6 events to 10^3) and injected anisotropy values (ranging from 10% to 1%). For all tests, the average value of the uncertainty on the isotropic parameter is compatible with the expectations: this provides further confidence in the robustness of the fit method.

5.2.2 Realistic absolute maps

In figure 5.13 and 5.14 the fit parameters for 10%, 1% and 1‰ N-S simulated map are shown.

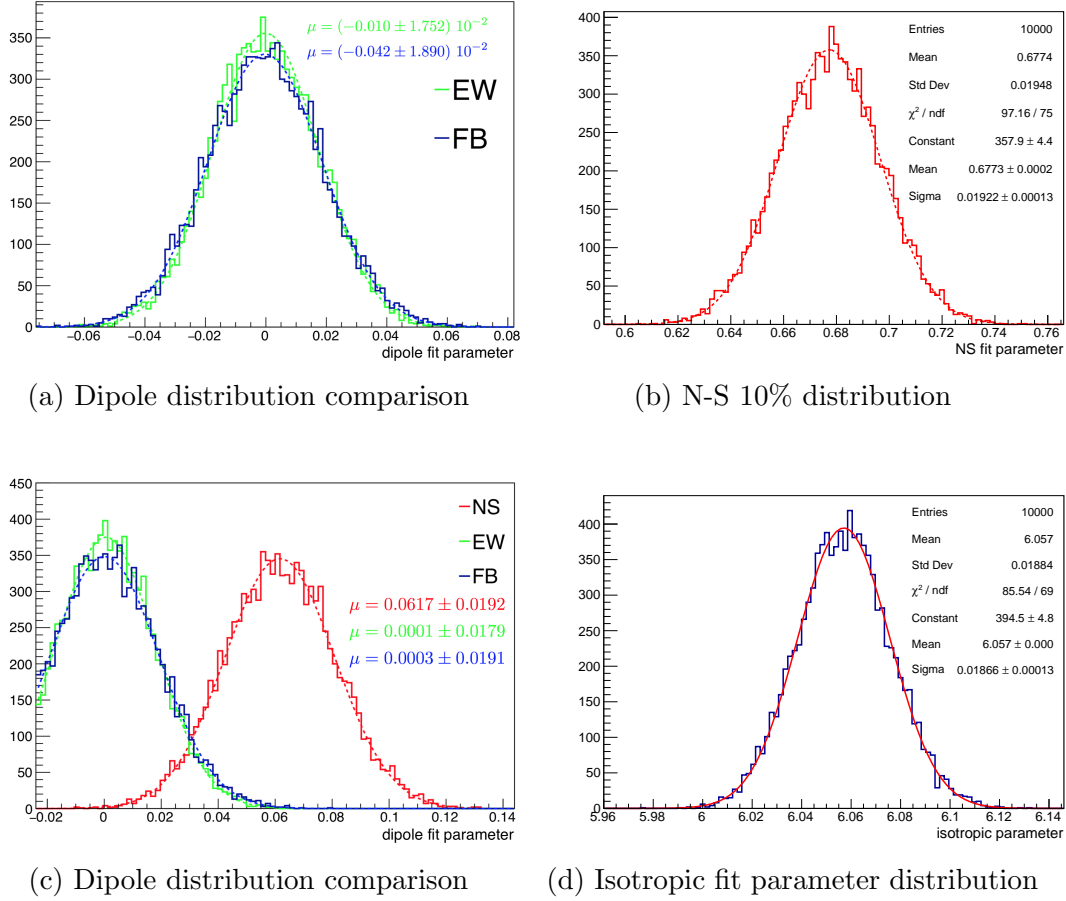
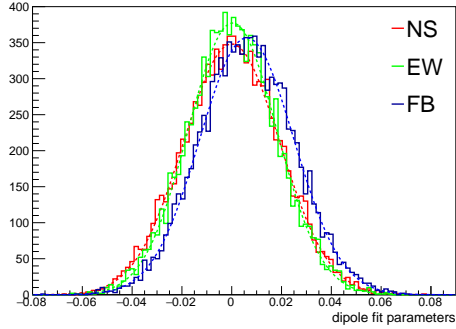
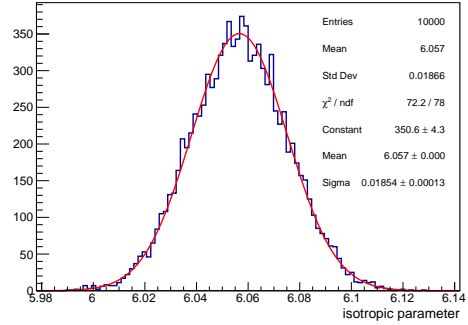


Figure 5.13: **(left column) (top)** Distribution of the E-W and F-B dipole fits parameters for a 10% N-S map. **(bottom)** Distribution of the dipole fit parameters **(right column) (top)** N-S fit parameter for a 10% N-S map. **(bottom)** Distribution of the isotropic fit parameter.

Figure 5.13 shows that in case of 10% and 1‰ of injected dipole intensities, the anisotropy components are well recognised and can be easily distinguished.



(a) Dipole distribution comparison



(b) F-B 1‰ distribution

Figure 5.14: **(left column)** Distribution of the dipole fits parameters. **(right column)** Distribution of the anisotropic fit parameter.

Comparing figure 5.14 with 5.13 the resolution power of the fitting procedure is evident; injecting a 1‰ dipole anisotropy this is not distinguishable from the others.

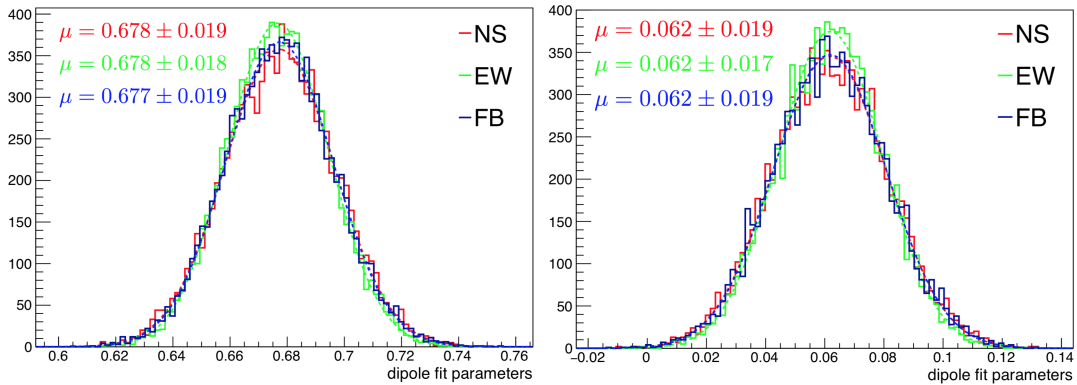


Figure 5.15: **(left)** Distribution of the anisotropic parameters for 10% injected maps. **(right)** Distribution of the anisotropic parameters for 1% injected maps.

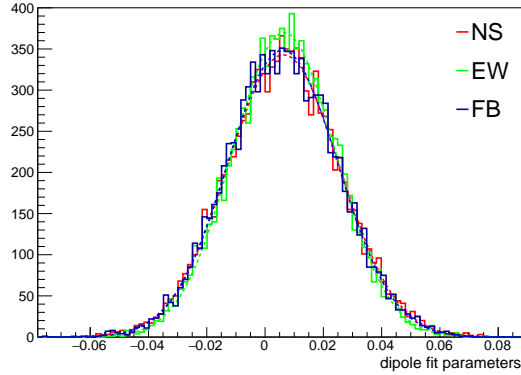


Figure 5.16: Distribution of the anisotropic parameters for 1‰ injected maps.

Figure 5.17 shows the result of the fit procedure on statistical independent 1% realistic mixed maps, characterized by: 1% N-S (red distribution), 1% E-W (green distribution) and 1% F-B (blue distribution). The Aitoff projection of the map is drawn on the right, while on the left the different dipole contributes are shown. Independently on their nature, the mean value if for all the same, as expected.

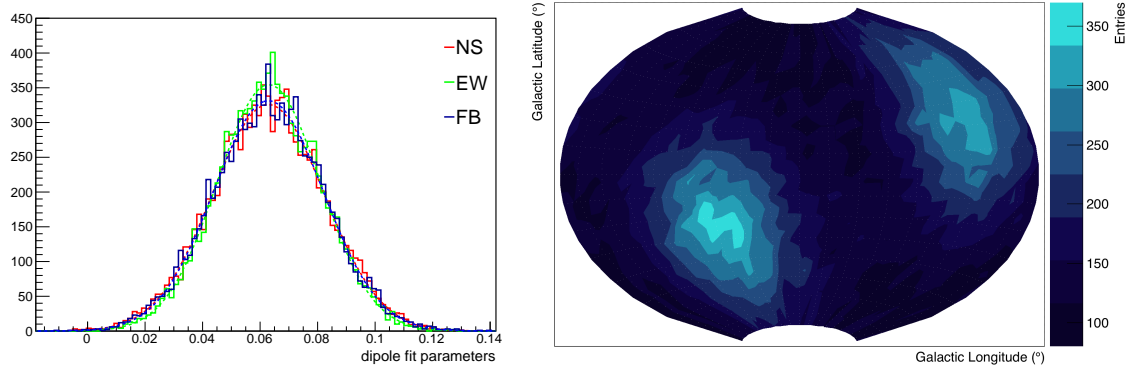


Figure 5.17: Distribution of the fit parameters. **(right)** Aitoff projection of the mixed flat data map: 1% N-S (red distribution), 1% E-W (green distribution) and 1% F-B (blue distribution).

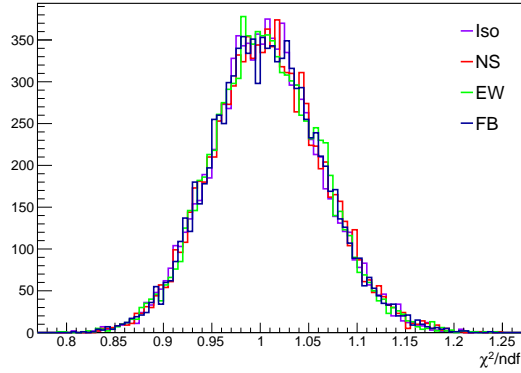


Figure 5.18: Distribution of χ^2/ndf for simulated data maps, differentiated as follows: isotropic (purple), 1% N-S (red), 1% E-W (green) and 1% F-B (blue).

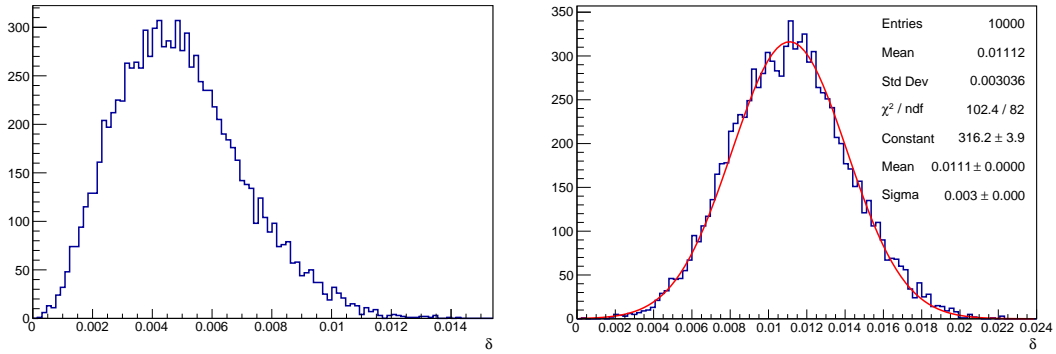


Figure 5.19: **(left)** Distribution of the δ parameter for an isotropic sky map. **(right)** Distribution of the δ parameter for a 1% N-S dipole anisotropy injected.

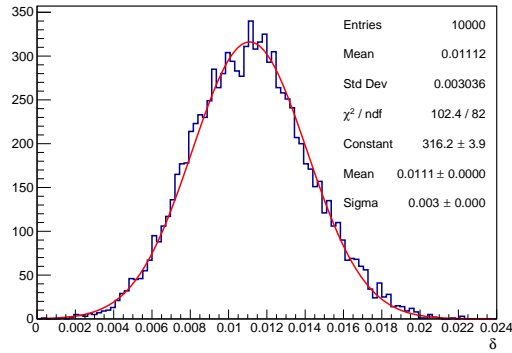
The plots in figure 5.18 represented the distribution of reduced χ^2 ; all the maps, isotropic and not, are correctly fitted though the data analysis algorithm.

Figure 5.19 reports the distributions for the δ parameter; in the left in case of isotropic maps and on the right of anisotropic ones, with 1% of N-S dipole injected. The distribution in the case of isotropic maps will be used, in the next section, to obtain the sensitivity of the detector; that on the right correctly confirms the injected anisotropy value of 1%.

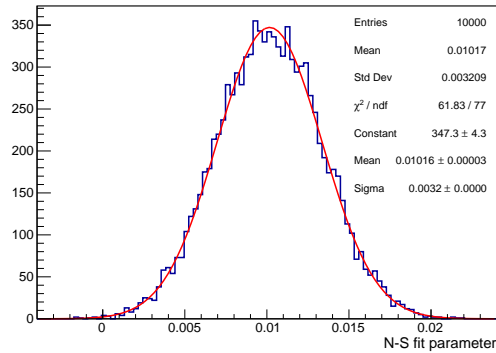
5.2.3 Realistic relative maps

Many of the concepts we explained in the previous section are still valid also for this kind of maps: the correct value of the fit parameters and the good χ^2/ndf values.

The relative maps, however, has the advantage that the fit parameters are directly connected with the injected anisotropy values. In figures 5.20 and 5.21 the comparison between the delta distribution for absolute realistic maps respect to the dipole fitted parameter for relative realistic maps is reported. The injected percentage of anisotropy is 1%, in order to better visualize the obtained results.

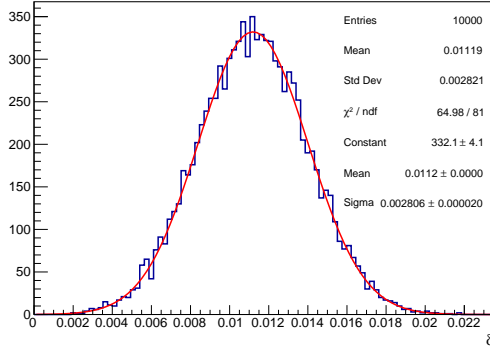


(a) Distribution of δ (N-S anisotropy)

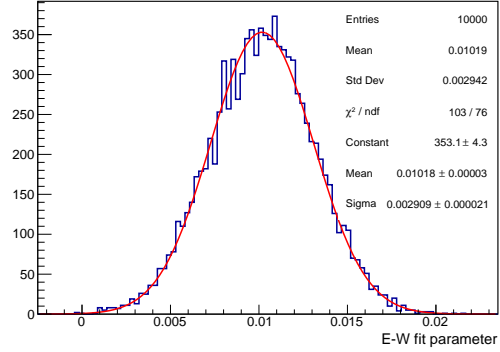


(b) Distribution of N-S fit parameter

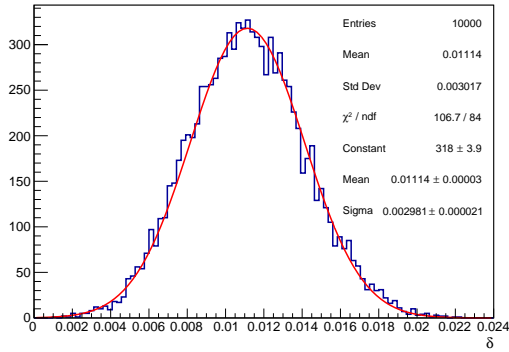
Figure 5.20: **(bottom)** Distribution of δ for absolute realistic maps. **(right column)** Distribution of the dipole fit parameters for relative realistic maps.



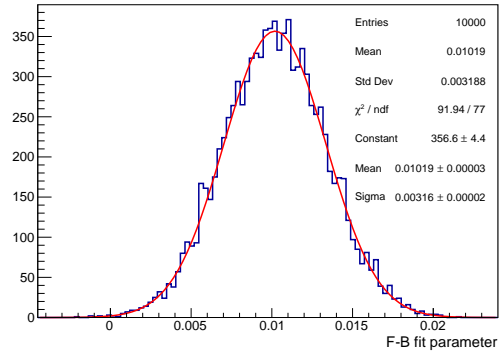
(a) Distribution of δ (E-W anisotropy)



(b) Distribution of E-W fit parameter



(c) Distribution of δ (F-B anisotropy)



(d) Distribution of F-B fit parameter

Figure 5.21: **(left column)** Distribution of δ for absolute realistic maps. **(right column)** Distribution of the dipole fit parameters for relative realistic maps.

These plots show that the overall compatibility between the distributions of mean values of the fit parameters and the δ parameters, suggesting that the two family of maps mostly provide the same information. However, tiny differences arise in the mean values and the lateral width of the distributions. Such differences may be the hint of a minor systematic that should be investigated in order to correctly assess the uncertainty in the final results. In this work, however, this has been neglected and the two methods have been considered as fully compatible

In the next section the δ distribution of the isotropic absolute realistic maps

will be used to obtain *DAMPE's* sensitivity to anisotropy measurements in function of both the energy and the exposition time.

5.3 Sensitivity of DAMPE as function of energy and time

In this section the sensitivity of the detector for anisotropy measurements will be evaluated, as function of the energy and the exposition time.

The sensitivity is calculated using the isotropic realistic simulated maps and applying the equation 4.27. The procedure has been applied on 10^4 statistically independent maps, for each value of energy and exposition time investigated. The sensitivity of the anisotropy measurements is then extrapolated from the distribution of the values of δ obtained for the 10^4 tries.

Table 5.1: Statistics of the simulated anisotropic maps

Energy bin (GeV)	Number of events
41.7 to 55.0	204505
55 to 72.4	115460
72.4 to 95.5	65847
95.5 to 125.9	37963
125.9 to 166.0	21416
166.0 to 218.8	12263
218.8 to 288.4	6928
288.4 to 380.2	3784
380.2 to 758.6	3705
758.6 to 1995.3	828

The table 5.1 shows the realistic statistics, for each energy bin, used to build the isotropic maps; the values taken from [7] represents the $e^+ + e^-$ data collected by *DAMPE* in the first 1.5 years of data acquisition.

The sensitivity is thus evaluated from the posterior distribution assuming a 68% and 95% confidence level.

Figure 5.22 shows the resulting upper limits at 95% CL up to 1995.3 GeV for the $e^+ + e^-$ measurements. Together with the upper limits obtained by Fermi-LAT [19] and the expected values of the models for the SNR Vela [19, 20] and the pulsar Geminga [19, 20]. The plot shows that at low energy the sensitivity is of the order of $6 \cdot 10^{-3}$, just considering 1.5 years; at high energy and considering 6 years of data, *DAMPE* results competitive with respect to other orbit experiments.

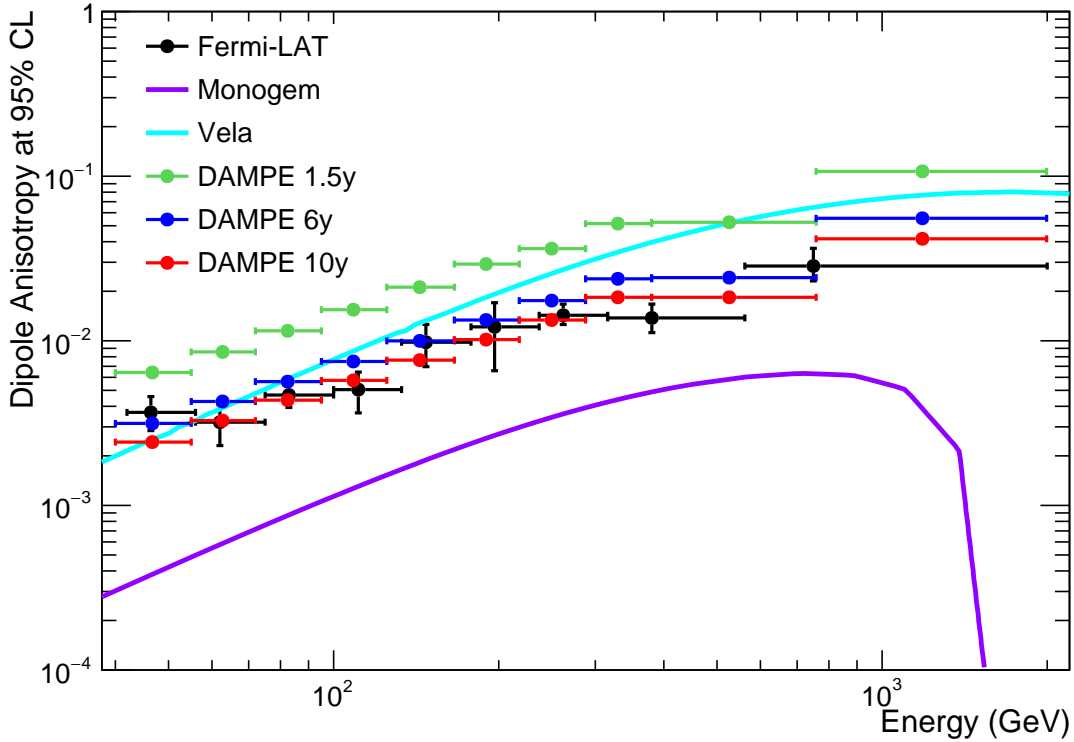


Figure 5.22: **red**: prediction of the upper limits at 95% CL up to 1995.3 GeV for the $e^+ + e^-$ measurement of the DAMPE experiment evaluated in this work. **black**: prediction of the upper limits at 95% CL for the $e^+ + e^-$ measurements of the Fermi-LAT experiment [19]. **cyan**: Vela SNR. **green**: Monogem pulsar. For DAMPE, different statistics have been considered: 1.5, 6 and 10 years.

In figure 5.22 the upper limits of Fermi-LAT have been obtained as the mean value of the different analysis methods results [19]. The error bars on the Y axis show the CL range for each energy bin.

An increase in the collected statistics (or, equivalently, the acquisition time) may result in an improvement of the dipole sensitivity, as shown in figure 5.22. This is also highlighted in figure 5.23, where the upper limits for 68% and 95% CL are shown as function of the mission duration and the improvement in the sensitivity scales as $1/\sqrt{N}$, where N is the number of the collected events.

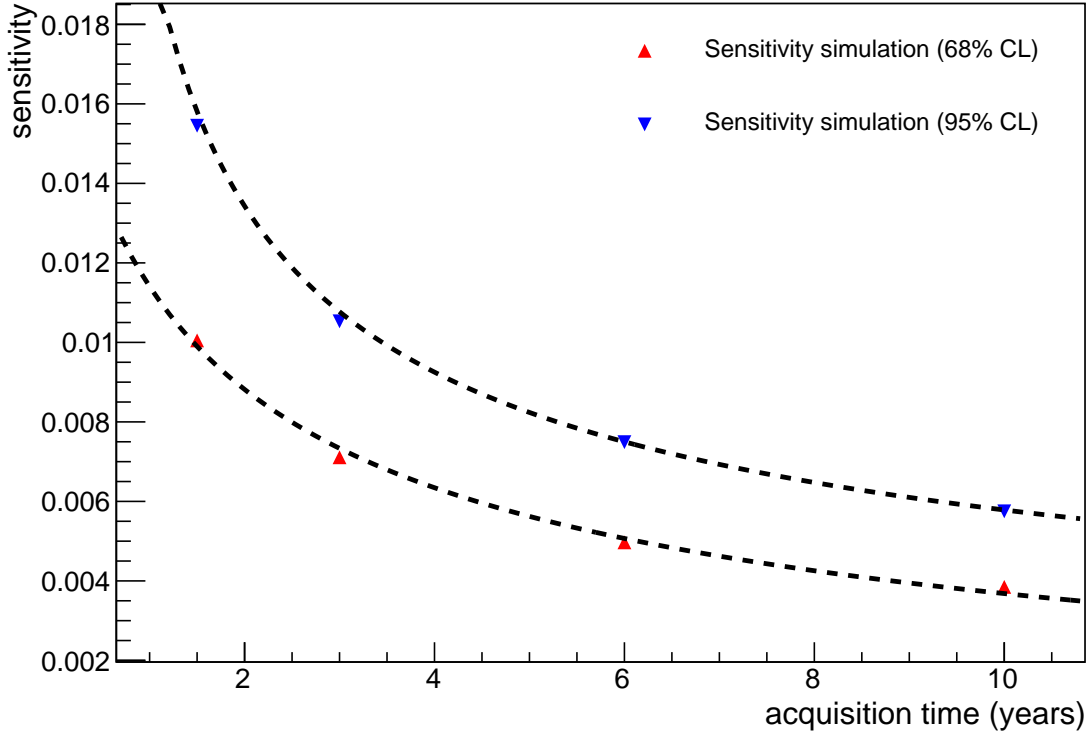


Figure 5.23: Simulation of the sensitivity to dipole anisotropy at 68% and 95% CL, in function of acquisition time (or, equivalently, in the triggered events) in the energy bin ranging from 95.5 to 125.9 GeV. Dashed lines represent the functions, scaling as $1/\sqrt{N}$, that fits the upper limits.

Figures 5.24 and 5.25 show the predictions of the upper limits at 95% CL up to 10 years of mission duration, for the $e^+ + e^-$ measurement of the DAMPE experiment and compared with the expected dipole anisotropy from Vela SNR and Monogem PWN, as already done in figure 5.23.

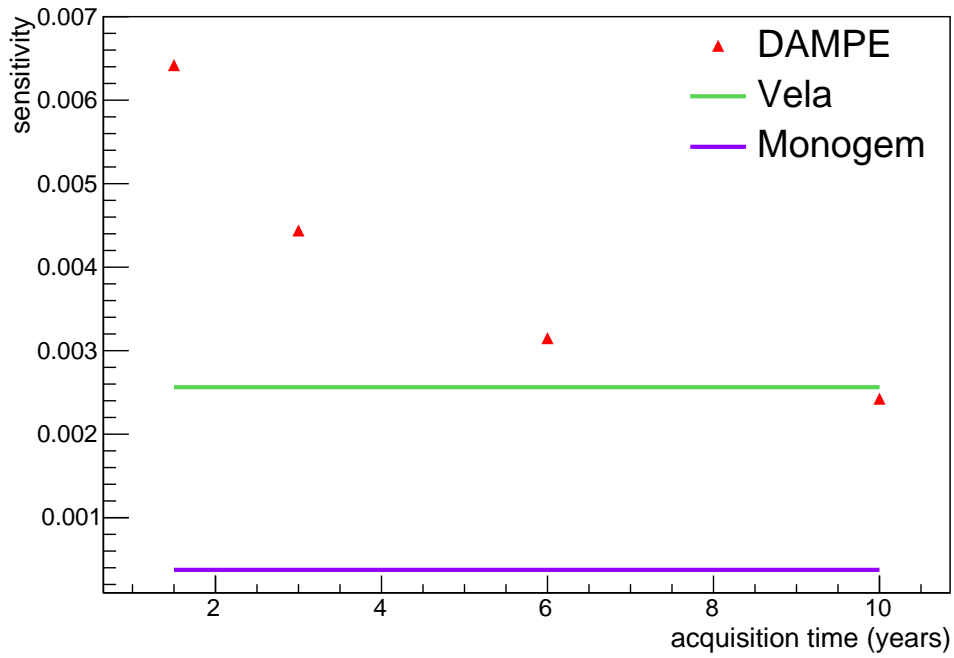


Figure 5.24: **red**: prediction of the upper limits at 95% CL up to 10 years of mission duration, for the $e^+ + e^-$ measurement of the DAMPE experiment in the energy bin from 41.7 to 55.0 GeV. **green**: Vela SNR. **purple**: Monogem pulsar

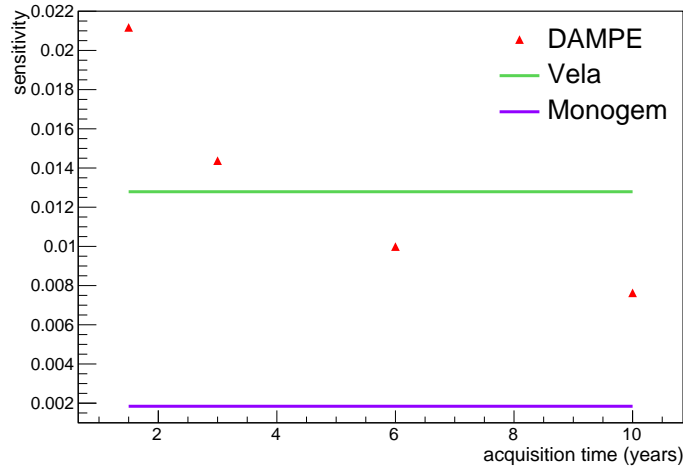
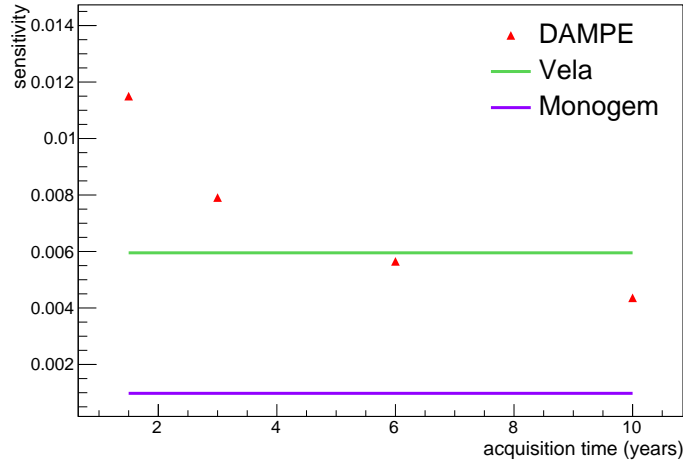


Figure 5.25: **(top)**: prediction of the upper limits at 95% CL up to 10 years of mission duration, for the $e^+ + e^-$ measurement of the DAMPE experiment in the energy bin from 72.4 to 95.5 GeV **(red)**. **(bottom)**: prediction of the upper limits at 95% CL up to 10 years of mission duration, for the $e^+ + e^-$ measurement of the DAMPE experiment in the energy bin from 125.9 to 166.0 GeV **(red)**. **green**: Vela SNR. **purple**: Monogem pulsar.

Depending on the energy range, the reference SNR model can be tested with longer mission duration, while the sensitivity of the measurement with DAMPE will not be enough to test the reference pulsar model. Of course, the limits will be useful to constrain the parameter space for many different similar models.

The HERD calorimetric cosmic ray detector mission, with a planned acceptance of $3 \text{ m}^2 \text{ sr}$ and planned to be operated from 2025 onboard the future Chinese Space Station, will improve the search sensitivities testing a parameter space completely out of range of the detectors currently operating in orbit. Thanks to its acceptance, HERD will permit to obtain highly competitive dipole anisotropy sensitivity already after a fraction of its planned mission time.

Chapter 6

Conclusions

Finally, the procedure has been applied to isotropic realistic maps, where no additional dipole level has been injected. The level of anisotropy extracted from the analysis of a large sample of isotropic realistic maps, that differ each other only by statistical fluctuation, provide information on the sensitivity of the search. The distribution of the fitted dipole anisotropy for a large sample of maps has been analyzed and a bayesian confidence limit has been set as function of the number of events in the sky maps.

The sensitivity of DAMPE to the dipole search has been quantified by the 95% CL upper limit on the dipole anisotropy measurement. It has been shown in this work that the upper limit depends on the collected statistics N as $1/\sqrt{N}$: this confirms that the level of sensitivity is dominated by statistical effects, as long as systematic uncertainties can be neglected in the procedure. The developed machinery has permitted to test the injected anisotropy dipoles, evaluating the sensibility of the detector. The dipole amplitude 95% CL upper limit for DAMPE after 1.5 years of data amounts to approximately 0.6% at 50 GeV, and increases up to approximately 20% at 200 GeV, considering the same statistics. Above this energy, the number of events in each bin is lower than 10k, and further studies have been needed to correctly assess the robustness of the procedure. With 6 years of data, the sensitivity of DAMPE is compatible with that of previous measurements from other missions for energies above 150 GeV; considering 4 years of statistics DAMPE can already set constraints to test models of nearby pulsars in this energy range. The DAMPE mission is expected to operate and collect data in space for at least 5 years since the start of the mission, and to correspondingly improve its dipole sensibilities by almost a factor of 2. However,

since most of current space detector are being operated for longer time than planned, due to the robustness of the detector technologies, and since the DAMPE detector has been operating without any major defiance since more than 2.5 years, the confidence that the mission duration could be extended is high. Consequently, the sensitivity to dipole anisotropies in the $(e^+ + e^-)$ channel using all the data collected by the end of the mission could further improve than what reported earlier. In the scenario where no anisotropy will be detected, a breakthrough advance in the field will require a detector with an acceptance at least 10 times larger than that of DAMPE.

The HERD calorimetric cosmic ray detector mission, with a planned acceptance of $3 \text{ m}^2 \text{ sr}$ and planned to be operated from 2025 onboard the future Chinese Space Station, will improve the search sensitivities testing a parameter space completely out of range of the detectors currently operating in orbit.

In conclusion, a procedure for measurement of dipole anisotropies has been developed in this work. The procedure has been tested and verified on Monte Carlo simulations of sky maps created taking into account the acceptance, the livetime and the time-dependent pointing direction of the detector. The sensitivity for search of dipole anisotropies in the $(e^+ + e^-)$ channel by DAMPE has been evaluated and compared with other detectors and expectation from known astrophysical sources. The procedure can be (and will be) finally applied on the sky data map created using $(e^+ + e^-)$ events collected by DAMPE to measure the level of anisotropy in that channel, or to provide an energy-dependent upper limit if no anisotropy will be detected.

Both scenarios will provide novel and important information in the indirect searches for Dark Matter activity in the galaxy: the results will be used to set constraints on the astrophysical models that are invoked to explain the rise of the positron fraction, towards the identification of the dominating nature (astrophysical sources or Dark Matter annihilation or decay) of the primary source of positrons and electrons needed to explain the excess of positrons observed in cosmic rays.

Appendices

Appendix A

Fermi Acceleration Mechanism

In this section we are going to widely describe some characteristics of the Fermi acceleration mechanisms, obtaining the power spectrum of the accelerated particles.

A.0.1 Fermi Acceleration Mechanism I

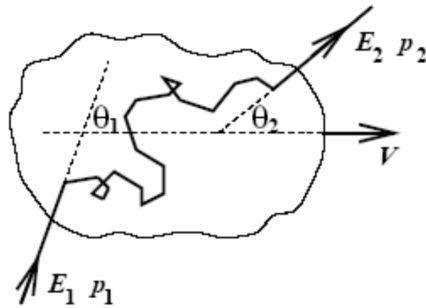


Figure A.1: Interaction between cosmic rays and a magnetic field inhomogeneities moving at velocity $V = \beta c$

Non-collisional scattering process could be described as an ultra-relativistic particle with energy E_1 and momentum p_1 collides with a magnetic field inhomogeneities (moving with non relativistic velocity $V = \beta c$) with an incidence angle θ_1 . Figure A.1 represents the entire process and also shows the final parameters of the scattering.

As fundamental assumption we consider all collisions, *internal* to the inhomogeneity, as elastic; in this case after the particles enters it keeps unchanged its energy.

What we propose to calculate is particle's mean energy increment. Thanks to Lorentz transformations is possible to switch from the lab reference frame to that integral with the moving magnetic inhomogeneity (whose variables are signed by an upper index), obtaining:

$$E'_1 \simeq \gamma(1 - \beta \cos \theta_1) \quad (\text{A.1})$$

Using Lorentz transformations again, remembering that thanks to elastic not-collisional scatterings with the magnetic field $E'_1 = E'_2$, escaping particles' final energy could be obtained as follows:

$$\begin{aligned} E_2 &= \gamma E'_2(1 + \beta \cos \theta'_2) = \gamma^2 E_1(1 - \beta \cos \theta_1)(1 + \beta \cos \theta'_2) \\ \frac{E_2}{E_1} &= \gamma^2(1 - \beta \cos \theta_1)(1 + \beta \cos \theta'_2) \end{aligned} \quad (\text{A.2})$$

The scattering probability between a particle (with relativistic initial velocity \vec{v}_i) and the magnetic inhomogeneity (with velocity \vec{V}) is proportional to the relative velocity:

$$\begin{aligned} P \propto |\vec{V} - \vec{v}_i| &\propto (\beta^2 + \beta_i^2 - 2\beta\beta_i \cos \theta_1)^{1/2} \\ &\simeq (1 - 2\beta \cos \theta_1)^{1/2} \simeq 1 - \beta \cos \theta_1 \end{aligned} \quad (\text{A.3})$$

To evaluate particle's *mean* energy gain we need to compute averages on both incoming and out-coming angles θ_1 and θ'_2 , as shown by equation A.2; thanks to the high number of scattering processes internal to the magnetic inhomogeneity, together with the random final particles' directions θ'_2 for each one of these, desired mean values are easily obtained:

$$\begin{aligned} \langle \cos \theta'_2 \rangle &= 0 \\ \langle \cos \theta_1 \rangle &\simeq \frac{\int_{-1}^1 (1 - \beta \cos \theta_1) \cos \theta_1 d(\cos \theta_1)}{\int_{-1}^1 (1 - \beta \cos \theta_1) d(\cos \theta_1)} = -\frac{\beta}{3} \end{aligned} \quad (\text{A.4})$$

The mean energy gain is so finally obtained as a second order expression on β , as the following equation explains:

$$\begin{aligned}
\left\langle \frac{E_2}{E_1} \right\rangle &\sim \gamma^2(1 - \beta \langle \cos \theta_1 \rangle) \\
&\simeq \frac{1}{1 - \beta^2} \left(1 + \frac{\beta^2}{3} \right) \simeq (1 + \beta^2) \left(1 + \frac{\beta^2}{3} \right) \\
&\simeq 1 + \frac{4}{3}\beta^2 + \mathcal{O}(\beta^4)
\end{aligned} \tag{A.5}$$

$$\left\langle \frac{\Delta E}{E} \right\rangle \simeq \frac{4}{3}\beta^2$$

Equation A.5 is of great importance and shows the limitation of the Fermi mechanism I, the β^2 dependence. This value, that's referred to the magnetic inhomogeneity motion, is of the order of just few percents, making this process particularly inefficient, except in the case of high particles' initial energy. Energy losses didn't take part of the whole discussion, further diminishing the efficiency of the mechanism. The original theory by Fermi considers the galactic disk particles' acceleration region; substituting CR typical escape times and β value we obtain a spectral index like 30, particularly distant from the experimental value. *This is enough to make this model incorrect.*

A.0.2 Fermi Acceleration Mechanism II

This a completely different process respect the previous one; in this case the acceleration mechanism is not anymore based on a magnetic field inhomogeneity but a plane shock wave, moving through the interstellar medium.

Hydrodynamic, or more in general magnetohydrodynamic, differently from other physical disciplines admits discontinuos solution for all the physical quantities describing a fluid status, like density, temperature and pressure. The process by which these quantities rapidly change their values is known as *shock*; here we usually have a plasma rapidly expanding at *supersonic* but not relativistic velocity through the interstellar medium, whose wavefront's kinetic energy is transformed to thermal energy of the particles next to the discontinuity (shock sources will be deeply analyzed in the next section). Thanks to this energy transformation process particles, confined in a narrow

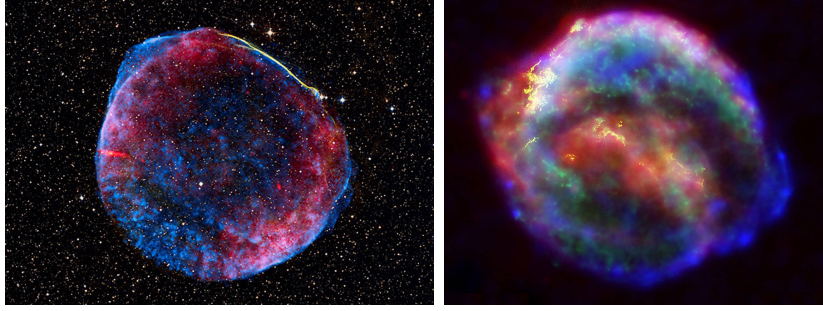


Figure A.2: Examples of shock waves by SN explosion

region next to discontinuity, increase their temperature, pressure and density as provided by *Rankine-Hugoniot* relations (RH); that's at the basis of the *Fermi acceleration mechanism of the second type*.

Is possible to describe the cosmic fluid as *downstream*, if just crossed by the shock moving at velocity U , or *upstream* in the other case. Particles are subject to diffusive processes by the local magnetic field when switching from one to another of these reference systems, transforming their velocity distributions to isotropic; each time this happens they gain a certain amount of energy. Considering the high number of times the shock is crossed, together with the high number of particles, the final energy of the system could be huge.

Considering an observer integral to the reference frame of the shock wavefront, he sees the shock approaching at velocity U , while backward the particles are leaving it at speed v_2 , easily obtained using *RH* conditions:

$$\rho_1 v_1 = \rho_2 v_2 \quad (\text{A.6})$$

Equation A.6, in case of supersonic hard shocks, could be written as follows:

$$\frac{\rho_1}{\rho_2} = \frac{c_p/c_v + 1}{c_p/c_v - 1} \quad (\text{A.7})$$

The specific heat at pressure and volume constant, c_p and c_v , inserted into equation A.7, could be easily calculated in case of monatomic and completely ionized gas, leading to $v_2 = 1/4v_1 = 1/4U$. This means that, switching now

to the reference frame integral with the upstream fluid, the downstream one is approaching the observer at speed $V = 3/4U$, as shown in the following figure.

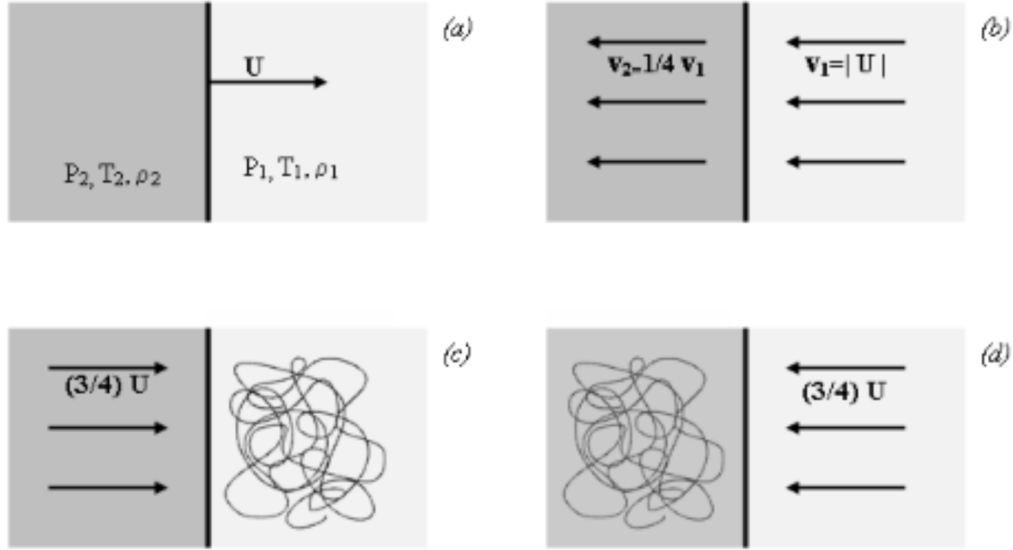


Figure A.3: (a) shock wavefront propagating at supersonic speed U , pressure, temperature and density of both upstream and downstream fluids are highlighted; (b) fluxes respect to the shock reference frame; (c) fluxes respect to the upstream fluid reference frame; (d) fluxes respect to the downstream fluid reference frame.

Considering thus the upstream fluid reference system, a particle crossing the shock toward the downstream one obtain an energy that we could write as:

$$E' = \gamma(E + p_x V) \quad (\text{A.8})$$

Writing equation A.8 γ resembles Lorentz's factor for the shock, whose unitary values is given its non-relativistic speed (contrary to what happens for particles), $p_x = p \cos \theta$ represents the momentum component normal to the discontinuity and, finally, V is downstream particles' speed.

Using what just said few lines above, we could obtain the energy variation:

$$\begin{aligned}\Delta E &= E' - E \sim pV \cos \theta = \frac{E}{c} V \cos \theta \\ \frac{\Delta E}{E} &\sim \frac{V}{c} \cos \theta = \frac{3U}{4c} \cos \theta = \frac{3}{4} \beta \cos \theta\end{aligned}\tag{A.9}$$

To obtain the mean energy gained by a particle we have to compute the angle average, with a procedure completely analogous to what previously done; this way just the final result will be provided:

$$\left\langle \frac{\Delta E}{E} \right\rangle \sim \beta\tag{A.10}$$

Respect to the first type acceleration mechanism, process efficiency increased!

To calculate the differential spectrum index, and comparing it to the observed one, we should before obtain particles' escape probability from the acceleration site. Using gas kinetic theory, the number of particles crossing the shock on both directions is $(1/4)Nc$, being N is their density. After crossing, they have a such probability to escape from the acceleration site via multiple collisions; the number of removed ones is so straightforward obtained as $NV = (1/4)NU$. The fraction of removed particles, by time unit, (and so the escape probability) is thus expressible as:

$$P = \frac{(1/4)NU}{(1/4)Nc} = \frac{U}{c}\tag{A.11}$$

Being the shock speed supersonic, but not relativistic, equation A.11 shows how the number of removed particles could be easily ignored. Applying both the escape probability (A.11) and the mean energy gain (A.10) into equation 1.13 we're able to obtain a spectrum index like 2.

$$dn(E) \propto E^{-2}dE\tag{A.12}$$

The whole process here described is particularly important and be used to efficiently describe CR spectrum up to to *knee* energies; not having infinite duration, infact, this process has an upper limit for the maximum reachable

energy. Observing particles with higher energies, however, does not undermine the model but simply highlights its limits and suggest the presence of possibly new kind of sources.

Appendix B

Estimate of Cold Dark Matter coupling with barionic matter

The standard cosmological model considers the cold dark matter (CDM)¹ a fundamental element for the formation of large structures, transforming the primordial universe in what we all today explore; it could be described as a non-relativistic and non-barionic weakly interactive matter (as better described in section 1.5).

Large scale structures, such as galaxies clusters or our solar system, are the result of the evolution of primordial density fluctuations; the cold dark matter, slowly moving inside isolated domains of the universe, permitted the creation of isolated more dense spots of matter², with typical density contrasts of $\delta\rho/\rho = \mathcal{O}(10^{-5})$. These small density contrasts will definitively grow during matter epoch, and when these one is decoupled from the radiation field.

$$\frac{\delta\rho}{\rho} \propto 1/z \tag{B.1}$$

Equation B.1 describes the evolution of the density primordial fluctuations,

¹Other models of dark matter were also considered, such as Hot Dark Matter (HDM) and Warm Dark Matter (WDM); thanks to new theoretical models and increasingly performing numerical simulations they were slowly abandoned in favor of the CDM one. Has been shown that cold dark matter could be able to produce large structures compatibles with the observed universe.

²In an hot dark matter scenario, all the density contrasts would be swept away because of HDM's rapid motion.

as function of the redshift z . All this process takes the name of *Bottom-Up structure formation*.

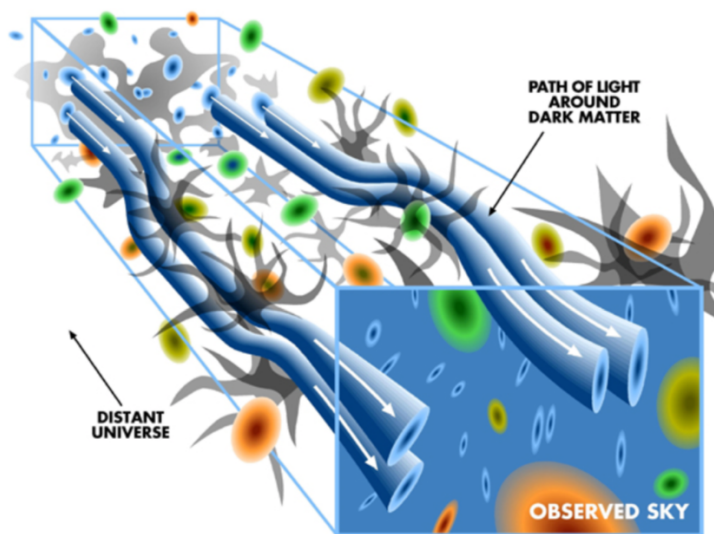


Figure B.1: Artistic representation of the *Cold Dark Matter* domains, as thickening points for barionic matter. This picture highlights CDM's gravitational effects on the radiation field.

As for all the particles, even for dark matter is possible to write the dynamic equation of its *freez-out*³:

$$\frac{x}{Y_{\chi}^{EQ}} \frac{dY_{\chi}}{dx} = \frac{\Gamma}{H} \left[\left(\frac{Y_{\chi}}{Y_{\chi}^{EQ}} \right)^2 - 1 \right] \quad (\text{B.2})$$

Equation B.2, where $x = m_{\chi}/T$ and $Y = n_{\chi}/s$, describes the evolution of WIMPs' density. For a given hypothesis on the WIMP mass m_{χ} and its interaction rate Γ is possible to proceed with the numerical integration of equation B.2 to found the freez-out temperature T_f , and so the value of x_f that fixes Y abundance at that moment.

³The *freeout* term is used to describe the situation where particle's interaction rate Γ is much lower respect to the Hubble parameter H , $\Gamma \ll H$.

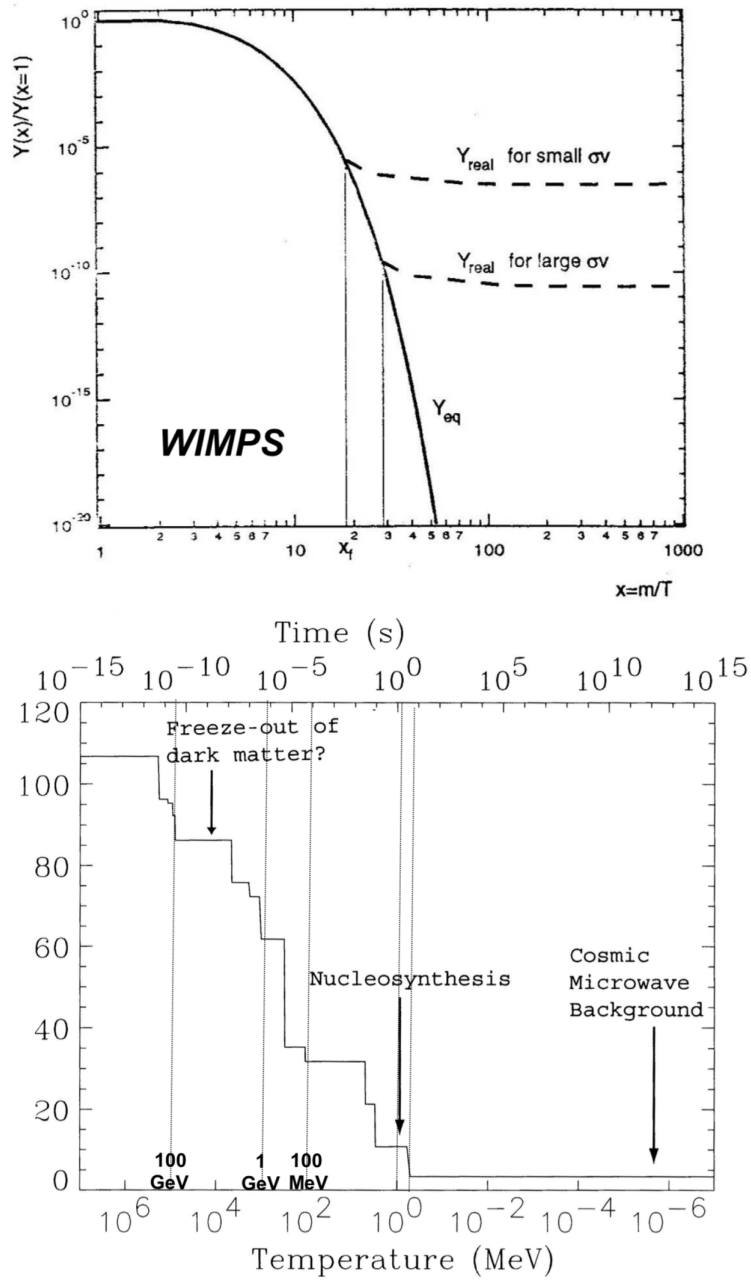


Figure B.2: **(top)** Graph representing different freez-out WIMPs abundances in function of their cross section. Bigger is the interaction rate and and later decoupling takes place. **(bottom)** CDM freezout, as function of energy and the relativistic degrees of freedom g .

For a cold dark matter particle, given its mass, more intense are its interactions and earlier the decoupling takes place.⁴

Qualitatively is possible to estimate the order of magnitude of the coupling constant between a cold dark matter candidate and a barionic particle.

Considering the current value of dark matter energy density Ω_χ , scaled for the critical density ρ_c :

$$\Omega_\chi = \frac{M_{\chi,0}n_{\chi,0}}{\rho_c}$$

$$\rho_c(t) = \frac{3H^2}{8\pi G} \implies \rho_c(t = \text{today}) = \frac{3H_0^2}{8\pi G} \quad (\text{B.3})$$

The current value of the critical density is $\rho_c = 1.88 \cdot 10^{-29} h^2 \text{gcm}^{-3}$ or, expressed in a more convenient way, $\rho_c = 10537.5 eV/c^2 h^2 \text{gcm}^{-3}$.

The dark matter freezout time, t_f , could be related to the actual time t_0 using the entropy conservation equation (B.4).

$$\left(\frac{n_\chi}{s}\right)_0 = \left(\frac{n_\chi}{s}\right)_f \quad (\text{B.4})$$

The entropy, at a certain redshift z , could be directly connected with the temperature value and the relativistic degrees of freedom g at that moment available, as equation B.5 expresses.

$$s \sim gT^3 \quad (\text{B.5})$$

Inserting equation B.5 into B.4 is possible to obtain the actual density of CDM particles:

$$n_\chi^0 = n_\chi \frac{s_0}{s} = n_\chi \frac{g_0}{g_f} \left(\frac{T_0}{T_f}\right)^3 \quad (\text{B.6})$$

The Hubble parameter H could be written as function of the temperature and Plank's mass m_{pl} , as follows:

$$H = 1.66 \sqrt{g_{eff}} \frac{T^2}{m_{pl}} \quad (\text{B.7})$$

⁴For an HDM particle the freez-out density is the equilibrium one, $Y_\chi(\text{inf}) = Y_\chi^{EQ}(x_f)$.

Writing equation B.7 g_{eff} represents the *effective* relativistic degree of freedom, that available given a certain energy $E = kT$. Using the freez-out condition $\Gamma = n_\chi \langle \sigma v \rangle \sim H$ we are able to obtain WIMPs' density at freez-out:

$$n_\chi \sim \frac{H}{\sigma v} = \frac{1.66 \sqrt{g_{eff}} (kT)^2}{\hbar c^2 m_{pl} \langle \sigma v \rangle} \quad (\text{B.8})$$

Substituting equation B.8 into B.3, we obtain:

$$\Omega_\chi h^2 = \frac{m_\chi}{\rho_\chi} \frac{1.66 \sqrt{g_{eff}} (kT_F)^2 g_0}{\hbar c^2 m_{pl} \langle \sigma v \rangle g_f} \left(\frac{T_0}{T_f} \right)^3 \quad (\text{B.9})$$

We now have to choose a reasonable value for the freez-out temperature T_f , or, in other words, a temperature at witch WIMPs could not be produced:

$$T_f = \frac{m_\chi}{20} \quad (\text{B.10})$$

Equation B.10 provides the requested value for the temperature; considering the measured value for the energy density of the dark matter $\Omega_\chi h^2 = 0.12$, we could use equation B.9 to obtain an estimate of CDM's interaction rate:

$$\langle \sigma v \rangle_{WIMPs} \approx \mathcal{O}(10^{-26} \text{cm}^2 \text{s}^{-1}) \quad (\text{B.11})$$

Is could be interesting the comparison between the obtained result of equation B.11 and the usual value for weak interaction:

$$\langle \sigma v \rangle_{weak} \propto \frac{\alpha^2}{(100 \text{GeV})^2} \sim 10^{-25} \text{cm}^3 \text{s}^{-1} \quad (\text{B.12})$$

The obtained results confirm what we said in the previous chapters (1,2) about WIMPs.

Appendix C

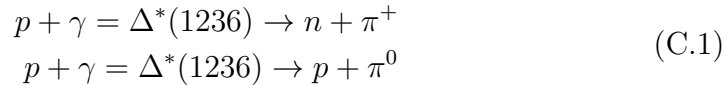
GZK cutoff

This physical process provides an estimate on the maximum traveled distance for protons, showing this is several orders of magnitude bigger respect to the electron and positron case.

It's based on anelastic scattering between high energy protons and CMB photons; cosmic microwave background radiation originated together with the universe itself during the Big Bang, thirteen billions of years ago. Still measurable, this radiation has a temperature equal to $2.7K$ and a characteristic density of 400 photons/cm^3 ; thermal information could be obtained by a precise measurement of radiation's spectrum, which has the typical black-body shape.

CMB detailed study, and its small temperature fluctuation principally, that we will not face in this thesis work, has permitted to obtain many important information regarding the standard cosmological model.

Scattering processes regarding protons and CMB can be written as follows:



The two processes (whose cross section is about $250\mu b$) shown in equation C.1 have a characteristic photo-production energy threshold of 300 MeV in the center of mass reference frame; this important value can be related to the photons' energy in the lab frame through a Lorentz transformation:

$$E_0^{FP} = \gamma(E_\gamma^{CMBR} + \frac{v_p}{c}E_\gamma^{CMBR}) = \gamma E_0^{CMBR}(1 + \frac{v_p}{c}) \approx 2\gamma E_\gamma^{CMBR} \quad (\text{C.2})$$

Writing equation C.2 protons have been supposed to be relativistic, which is completely true considering we're dealing with extremely high energy particles; energy value for CMB photons can be trivially obtained considering their frequency:

$$E_{\gamma}^{CMBR} = h\nu = 4.1 \cdot 10^{-15} eV \cdot s \cdot 160.2 \cdot 10^9 Hz = 6 \cdot 10^{-4} eV \quad (C.3)$$

Knowing the photoproduction threshold and the energy of the CMB photons, is possible to obtain protons' Lorentz parameter in the lab reference frame:

$$\gamma \approx \frac{E_0^{FP}}{2E_{\gamma}^{CMBR}} \approx 3 \cdot 10^{11} \quad (C.4)$$

Finally, once all the prerequisites quantities have been calculated, we can estimate protons' threshold energy for the scattering process E_0^{GZK} and their mean free path λ :

$$\begin{aligned} E_0^{GZK} &= \gamma(m_p c^2) \approx 3 \cdot 10^{20} eV \\ \lambda &= (\sigma_{p\gamma} n_{\sigma})^{-1} = 10^{25} cm = 3 Mpc \end{aligned} \quad (C.5)$$

If the energy of the proton is bigger than E_0^{GZK} the photoproduction process could start; assuming that in each interaction the proton loses 1/10 of its energy, and remembering the mean free path above calculated, is possible to estimate protons' maximum approaching distance at 30 Mpc .

Appendix D

BGO shower containment

In this section we are going to obtain the longitudinal containment of the BGO electromagnetic calorimeter.

Reading the BGO's characteristics from the PDG, its radiation length X_0 is $X_0 = 7.97 \text{ gcm}^{-2}$; knowing the density of the material $\rho = 7.13 \text{ gcm}^3$ the associated length L may be easily calculated, as $L = X_0\rho = 1.10 \text{ cm}$.

To properly calculate the longitudinal shower containment, an effective value Z_{eff} for the atomic number Z of the BGO material should be calculated:

$$Z_{eff} = \frac{1}{19}(83 \cdot 4 + 32 \cdot 3 + 8 \cdot 12) = 27.6 \quad (\text{D.1})$$

After the shower maximum, the particle production stops and both electrons and positrons having an energy below E_c (known as critical energy) will stop in a layer of $\sim 1X_0$, due to the ionization loss.

Once the Z_{eff} value has been calculated, the critical energy value could be easily obtained:

$$E_c = \frac{580 \text{ MeV}}{Z_{eff}} \sim 21 \text{ MeV} \quad (\text{D.2})$$

To describe the electromagnetic shower development is often used a variable $t = X/X_0$, the position on the calorimeter divided by the radiation length.

Is possible to obtain the maximum value of t for the shower, resembling the point where the number of particle $N(t)$ is maximum:

$$t_{max} = \ln\left(\frac{E}{E_c}\right) + C_{\gamma e} \sim \ln\left(\frac{10 \text{ TeV}}{21 \text{ MeV}}\right) - 0.5 = 12.6 \quad (\text{D.3})$$

Equation D.3 permits to obtain the value of the t parameter at the maximum of the shower development; $C_{\gamma e}$ is a parameter used to differentiate photon induced showers ($C_{\gamma e} = 0.5$) and electron induced ones ($C_{\gamma e} = -0.5$). In our case the great majority of the showers start by an electron, the result of the photo-conversion of a γ ray¹.

Is thus possible to compute the value of t for a 95% shower longitudinal containment, as follows:

$$t_{95\%} = t_{max} + 0.08Z_{eff} + 9.6 = 24.4 \quad (\text{D.4})$$

Using the $t_{95\%}$ calculated in equation D.4 is finally possible to obtain the requested thickness for the BGO calorimeter to contain the 95% of the shower:

$$h[cm] \sim \frac{24X_0}{\rho} = 27 \text{ cm} \quad (\text{D.5})$$

Remembering the real thickness of DAMPE's BGO eCAL, of 35 cm, is immediately possible to notice that the longitudinal containment of the shower is well above the 95% value.

In the same way, is possible to easily calculate the Molière radius, for the transversal containment:

$$R_M[cm] = \frac{21 \text{ MeV}}{E_c} L[cm] \sim L[cm] = 1.10 \text{ cm} \quad (\text{D.6})$$

Comparing the results of equation D.5 and D.6 is immediately evident that, considering the same percentage of containment, the transversal one requires a significantly lower amount of space.

¹Considering that the efficiency of the process is not unitary, some photon-induced are still present.

Appendix E

ToyMC simulation of DAMPE's geometrical acceptance

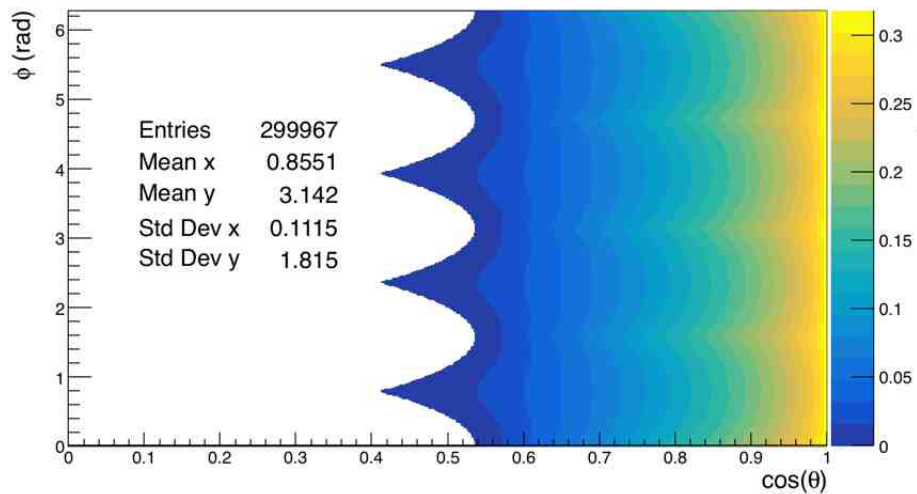


Figure E.1: 2D representation of the differential cross section, as function of $\cos(\theta)$ and ϕ .

Figure E.1 represents the two-dimensional differential acceptance, as function of $\cos(\theta)$ and ϕ , angles in the local reference frame describing the incoming

direction of a particle. This figure highlight periodic a series of periodic structures, due to the rectangular section of *DAMPE*'s BGO eCAL (as explained in section 4.2).

The cosmic rays have been generated according to a uniform distribution in $\cos^2(\theta)$ (for the polar angle θ) and ϕ (the azimuth coordinate) ¹, as reported in the Sullivan article.

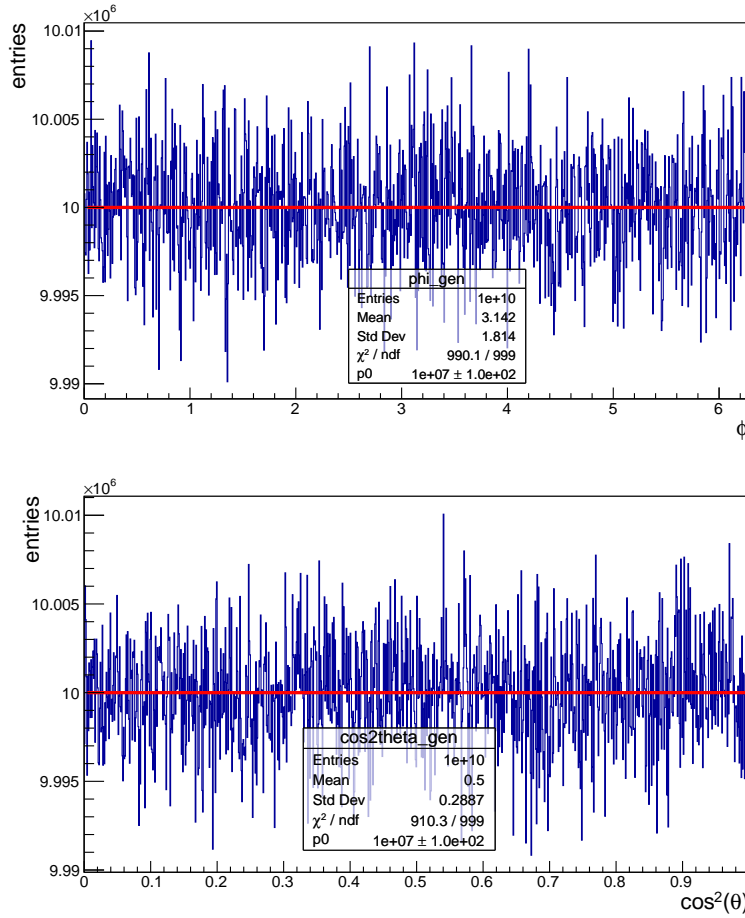


Figure E.2: **(top)** Uniform distribution of the azimuth coordinate ϕ . **(bottom)** Uniform distribution of $\cos^2(\theta)$, for the polar coordinate.

¹ θ and ϕ describe the incoming direction of the cosmic rays, in a reference frame fixed with the detector.

As a verify of the generation process, consider the distribution of the following distribution of the generated events:

$$\frac{dN_{gen}}{d\cos^2(\theta)} = k \quad (\text{E.1})$$

The k parameter may be obtained fitting the distribution with a *pol0* function, as reported in figure E.2 (bottom): $k = 1e + 07 \pm 1e + 02$.

Is possible to obtain the distribution of the generated events in function of the $\cos(\theta)$ variable, as follows:

$$\frac{dN_{gen}}{d\cos(\theta)} = \frac{dN_{gen}}{d\cos^2(\theta)} \frac{d\cos^2(\theta)}{d\cos(\theta)} = 2k\cos(\theta) \quad (\text{E.2})$$

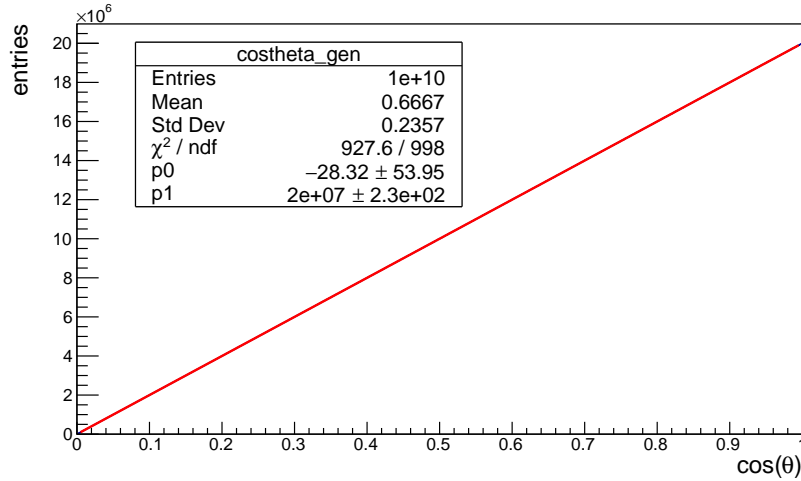


Figure E.3: Event distribution in function of $\cos(\theta)$.

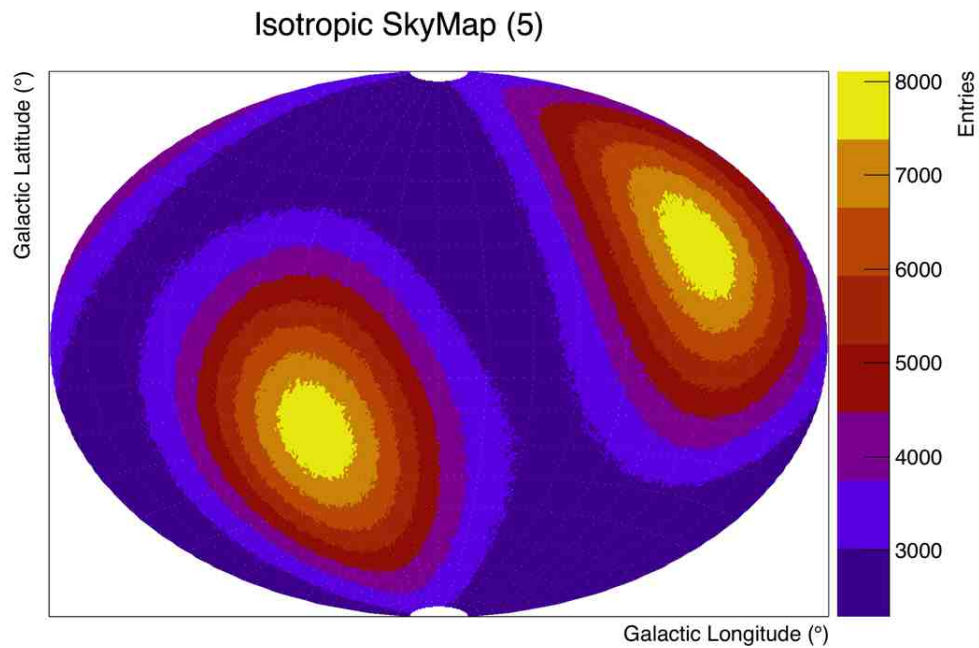
Considering the k value before obtained, the fit values of the distribution in figure E.3 result compatible with the expected ones.

Appendix F

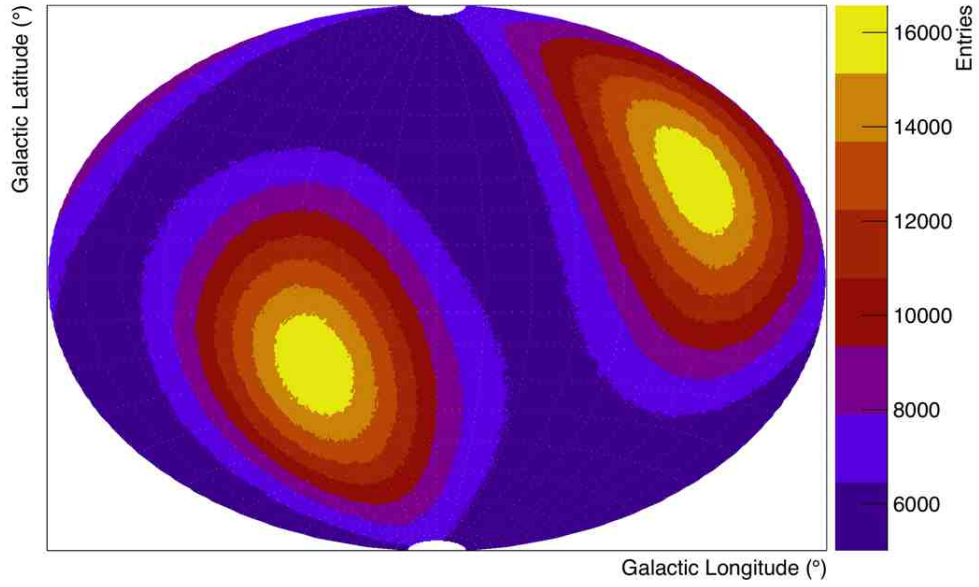
Reference isotropic maps

In this section are presented the reference isotropic maps for various k values (as written in graphs' titles).

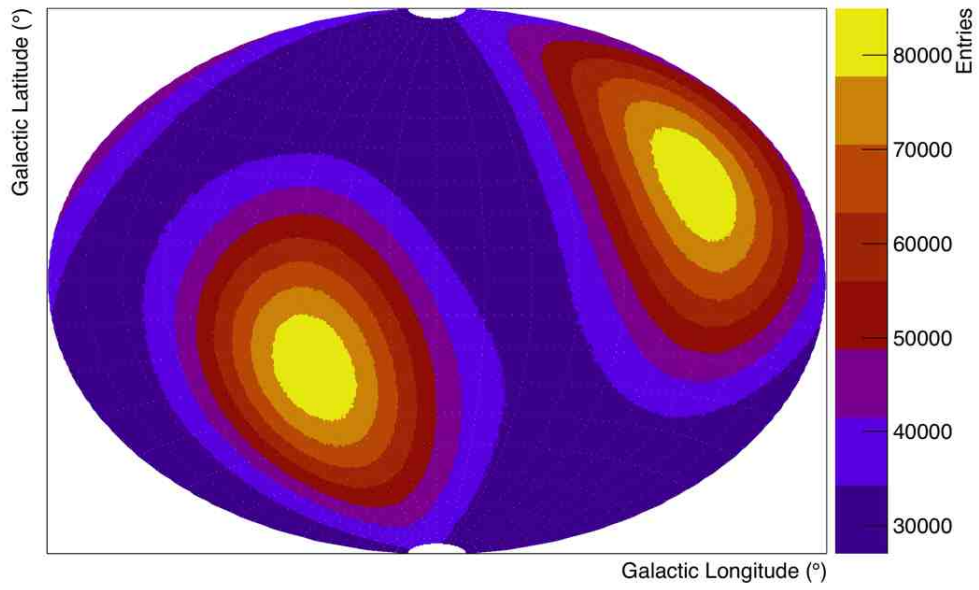
F.1 *k-fixed* maps



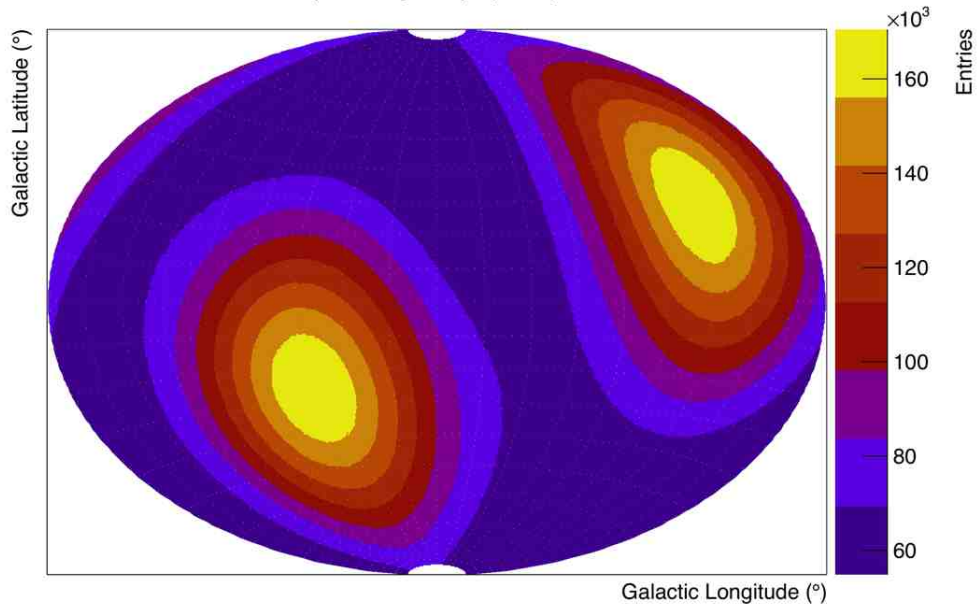
Isotropic SkyMap (10)



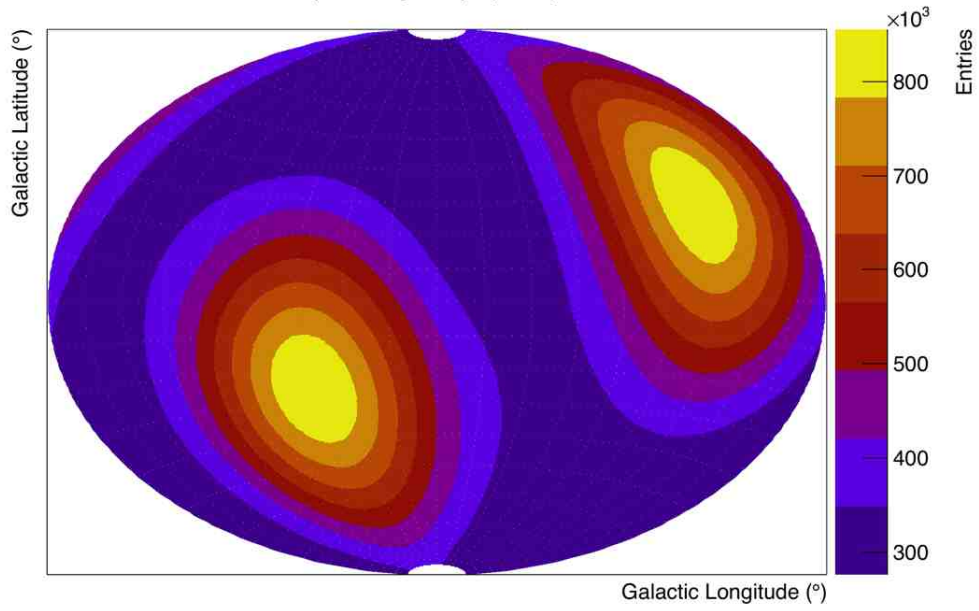
Isotropic SkyMap (50)

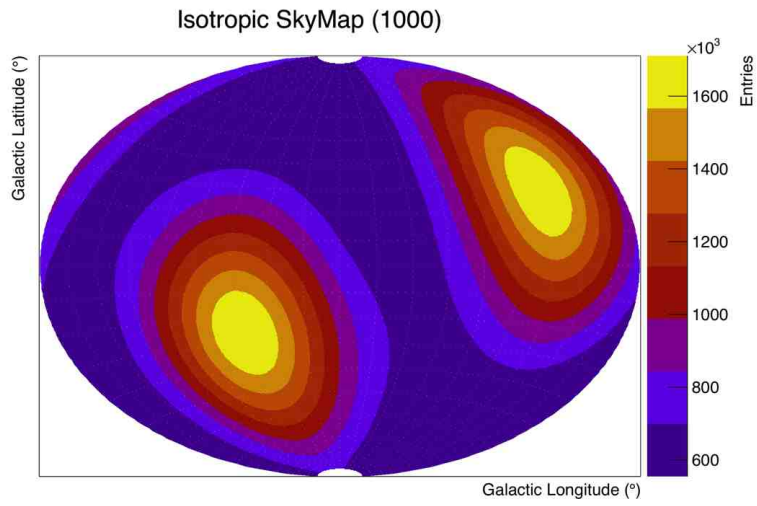


Isotropic SkyMap (100)

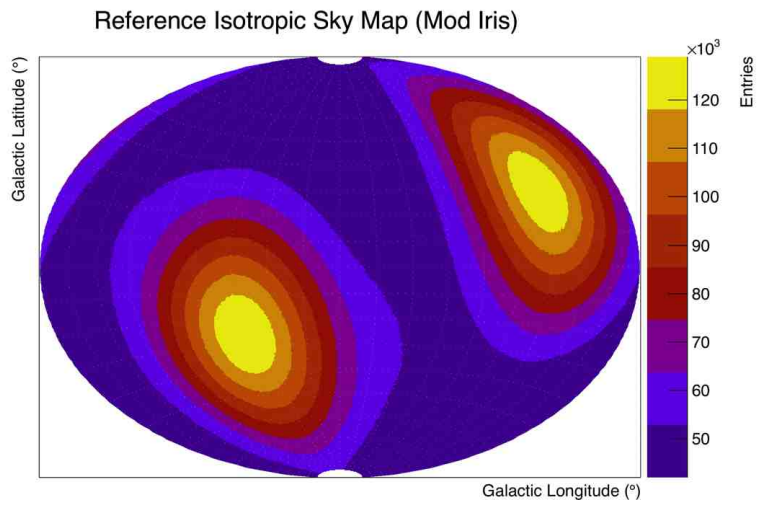


Isotropic SkyMap (500)





F.2 *rate-based* map



Appendix G

Data Maps

In this section will be presented some of the maps obtained through the injection technique, described in section 5.1. Different values of anisotropies has been tested: 10%, 1% and 1‰(respect to the isotropic template).

In the following pages are reported some of the most relevant maps, grouped for injected anisotropy percentage and fit model, including or not the detector acceptance.

For each of the fitting technique represented in the sketch in section 5.1 the following maps are produced:

- i Isotropic map (except for the relative case);
- ii Anisotropic $N-S$ map;
- iii Anisotropic $E-W$ map;
- iv Anisotropic $F-B$ map;
- v Anisotropic $N-S + E-W$;
- vi Anisotropic $N-S + F-B$;
- vii Anisotropic $E-W + F-B$;
- viii Anisotropic $N-S + E-W + F-B$.

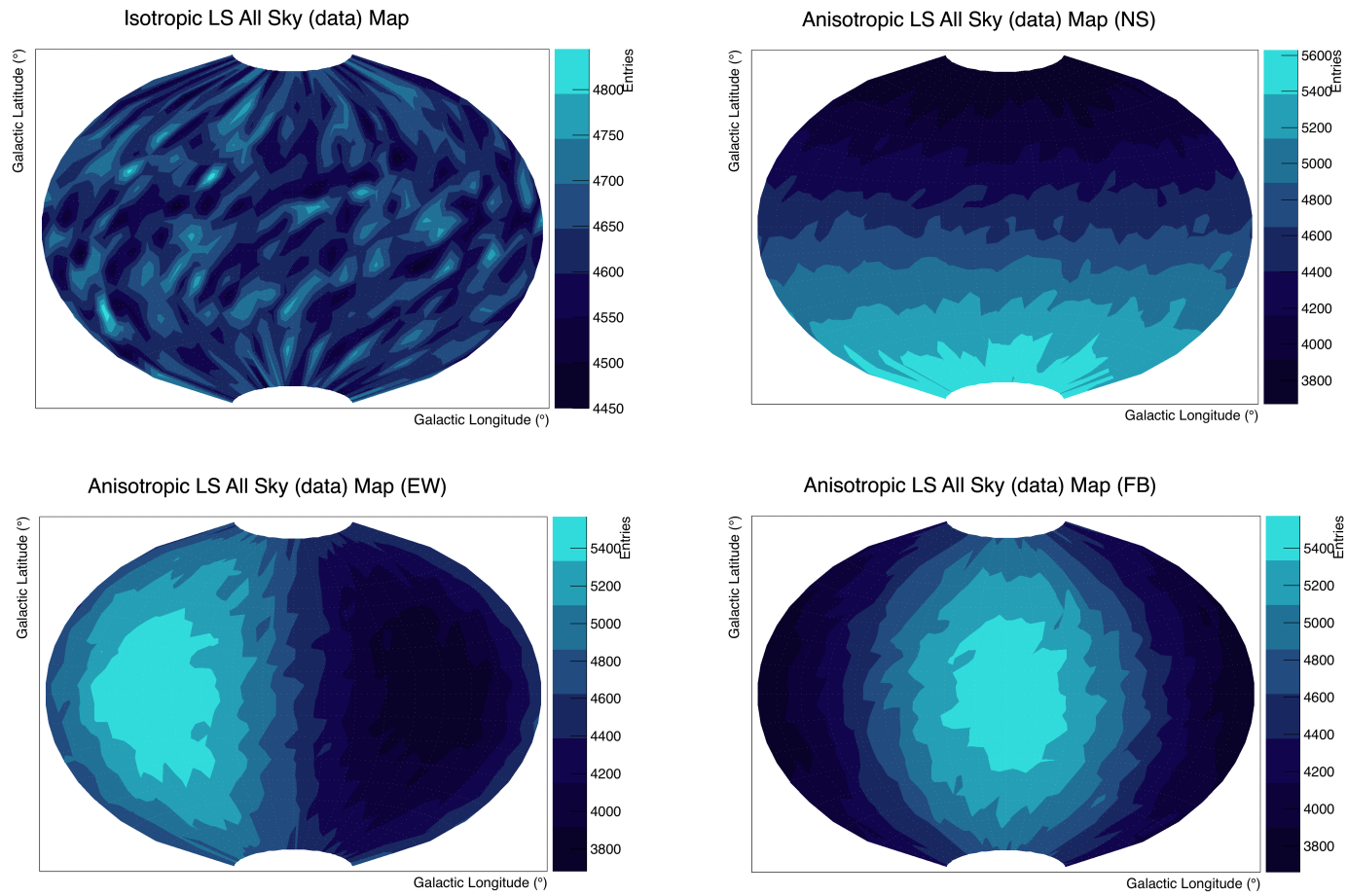


Figure G.1: *All-Sky* simulated data maps, 10% anisotropy injected

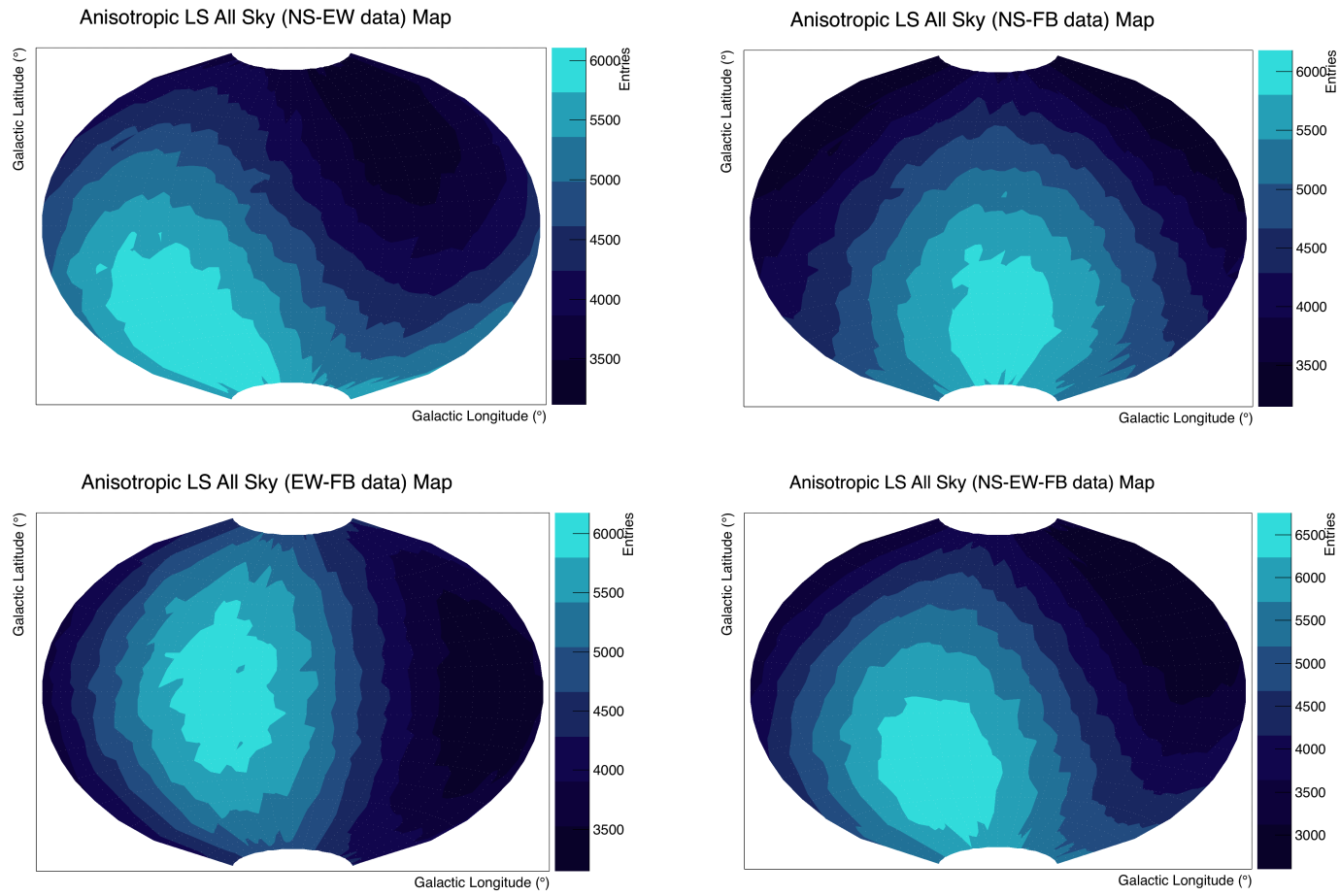


Figure G.2: *All-Sky* simulated data maps, 10% anisotropy injected

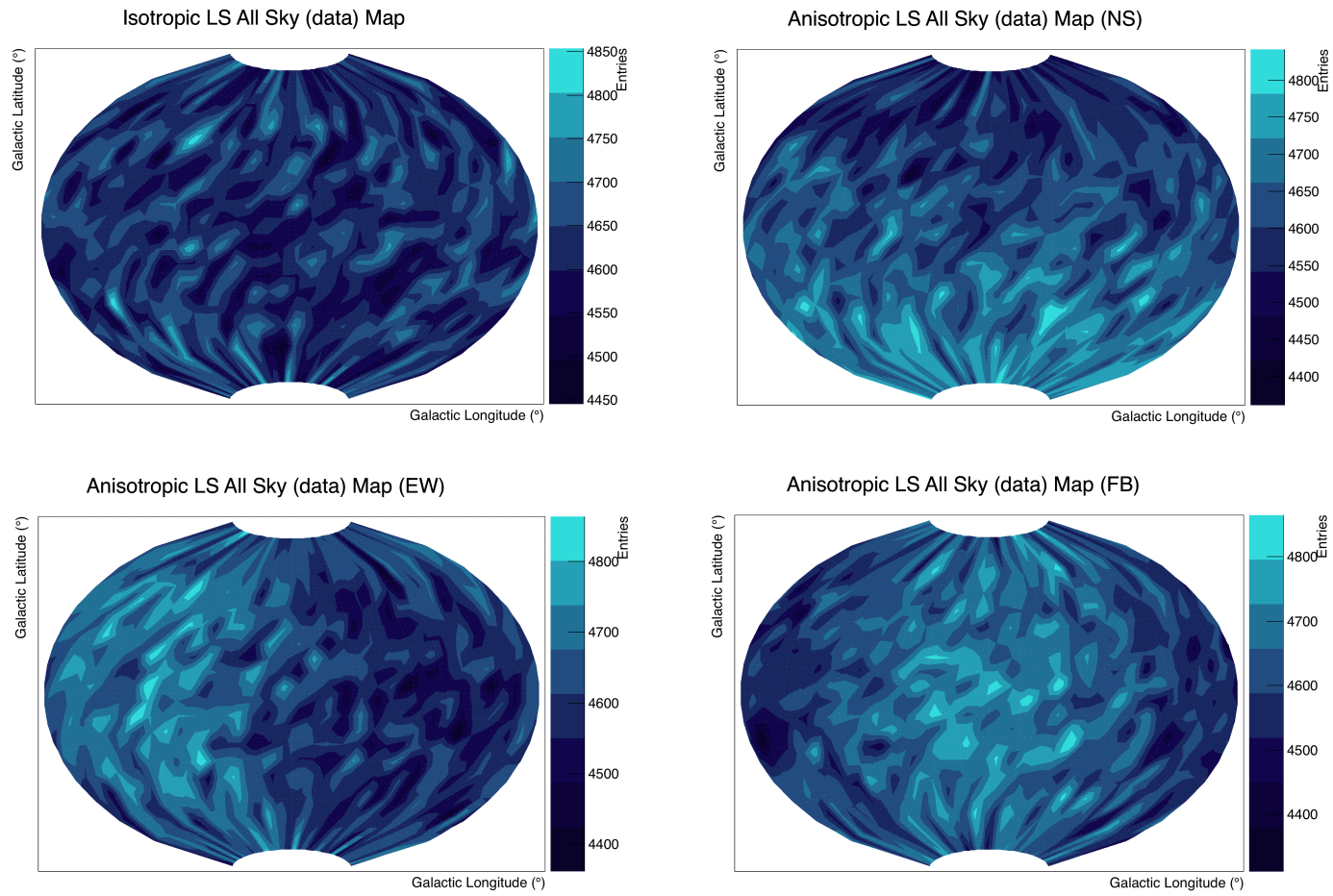


Figure G.3: *All-Sky* simulated data maps, 1% anisotropy injected

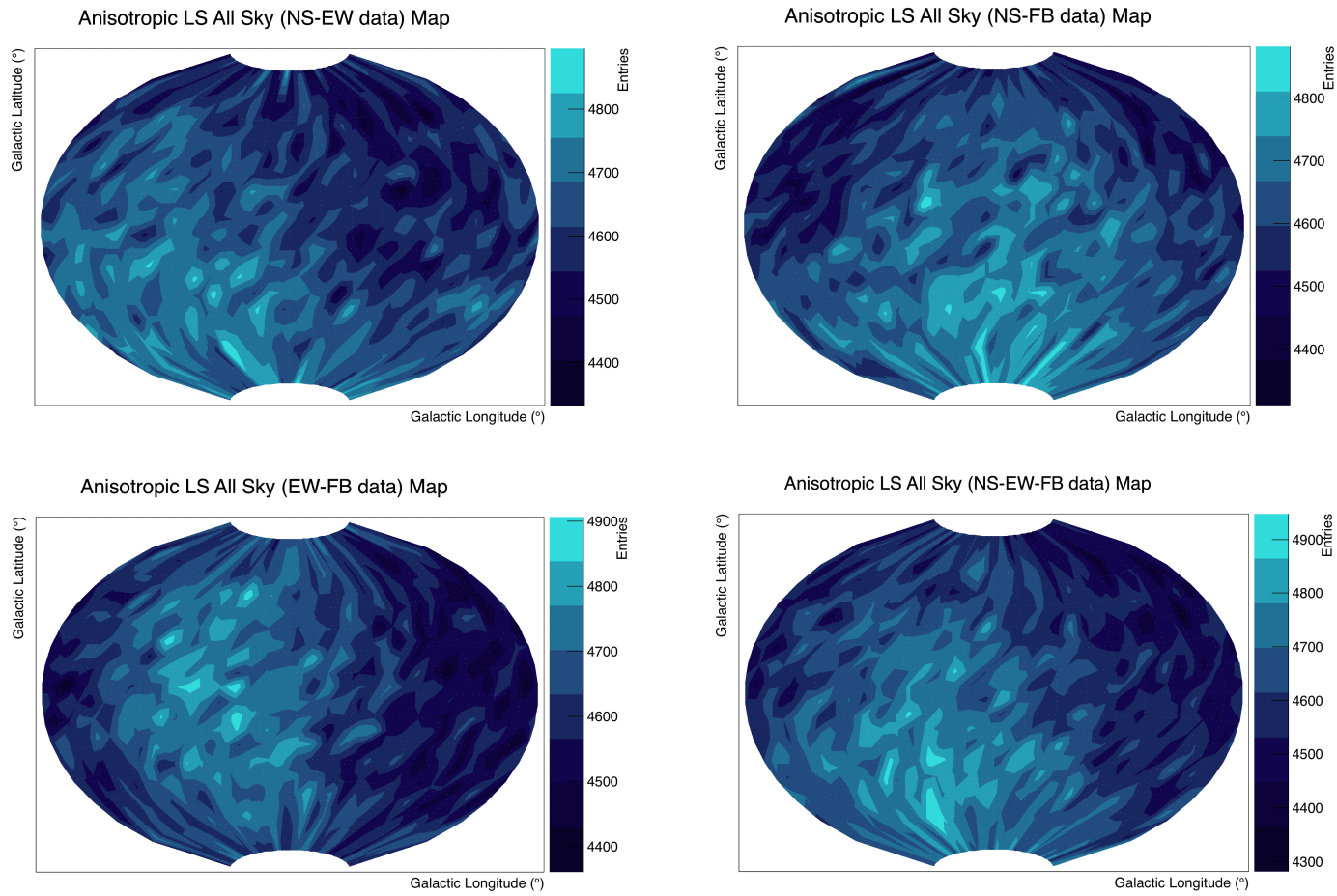


Figure G.4: *All-Sky* simulated data maps, 1% anisotropy injected

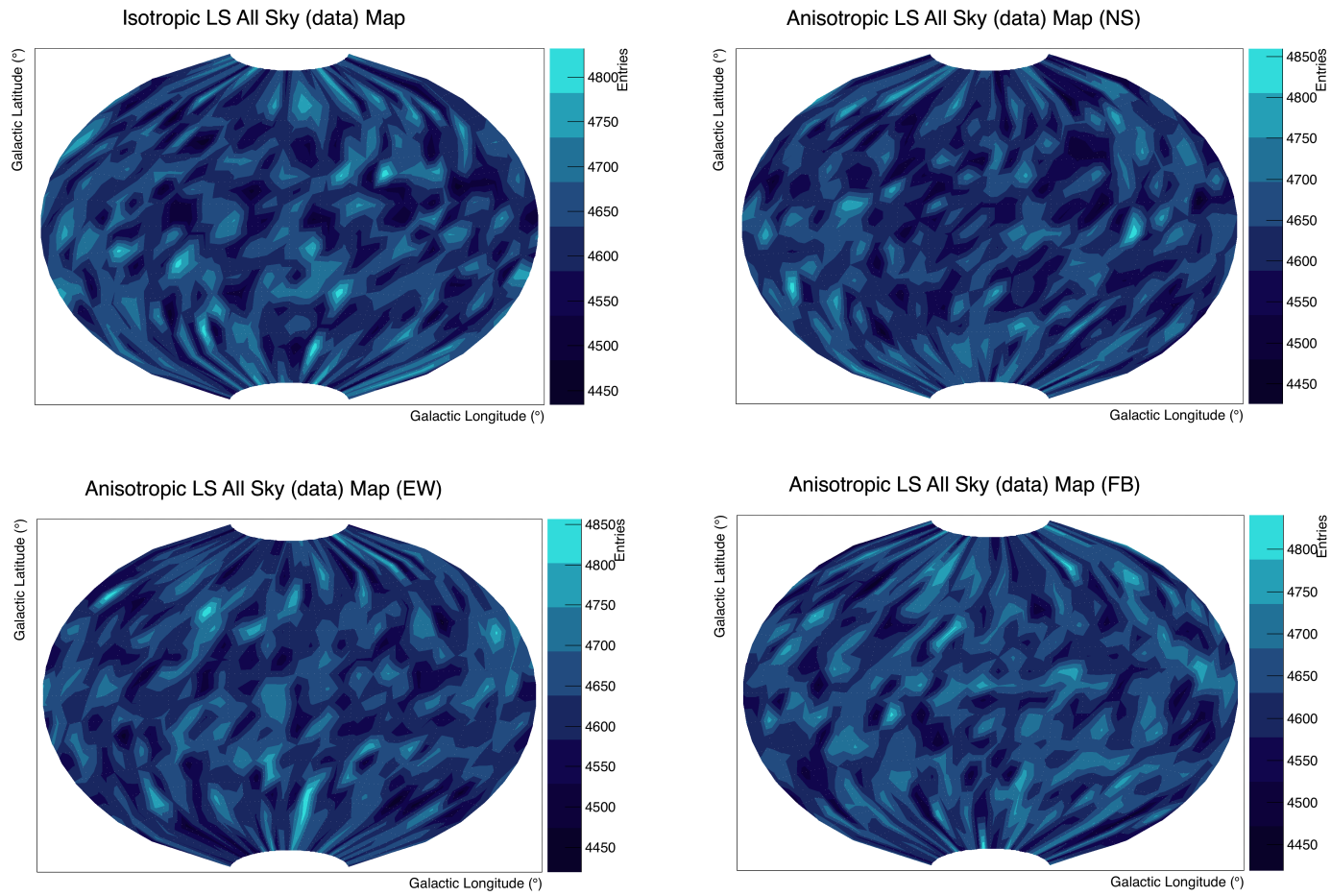


Figure G.5: *All-Sky* simulated data maps, 1‰ anisotropy injected

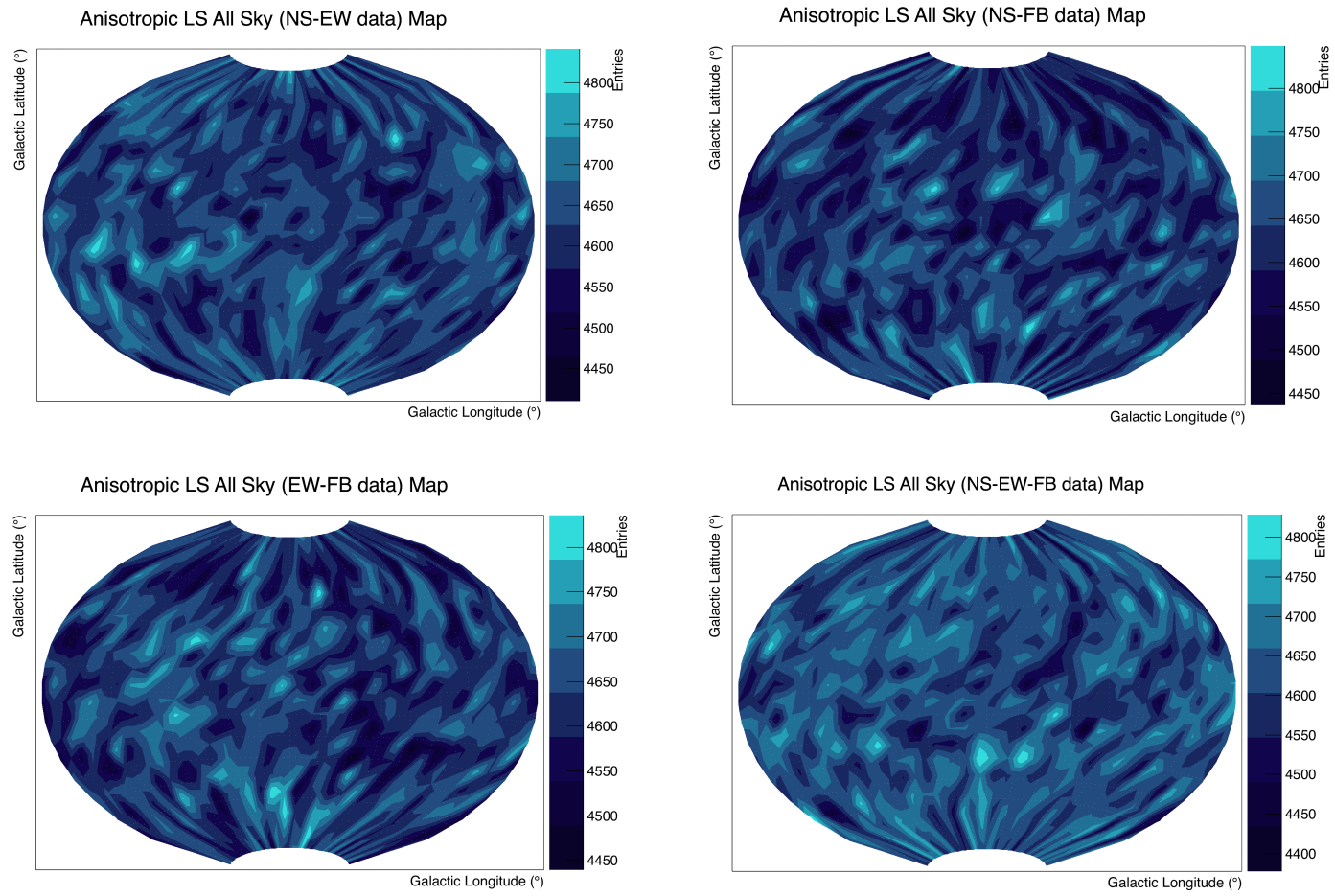


Figure G.6: *All-Sky* simulated data maps, 1‰ anisotropy injected

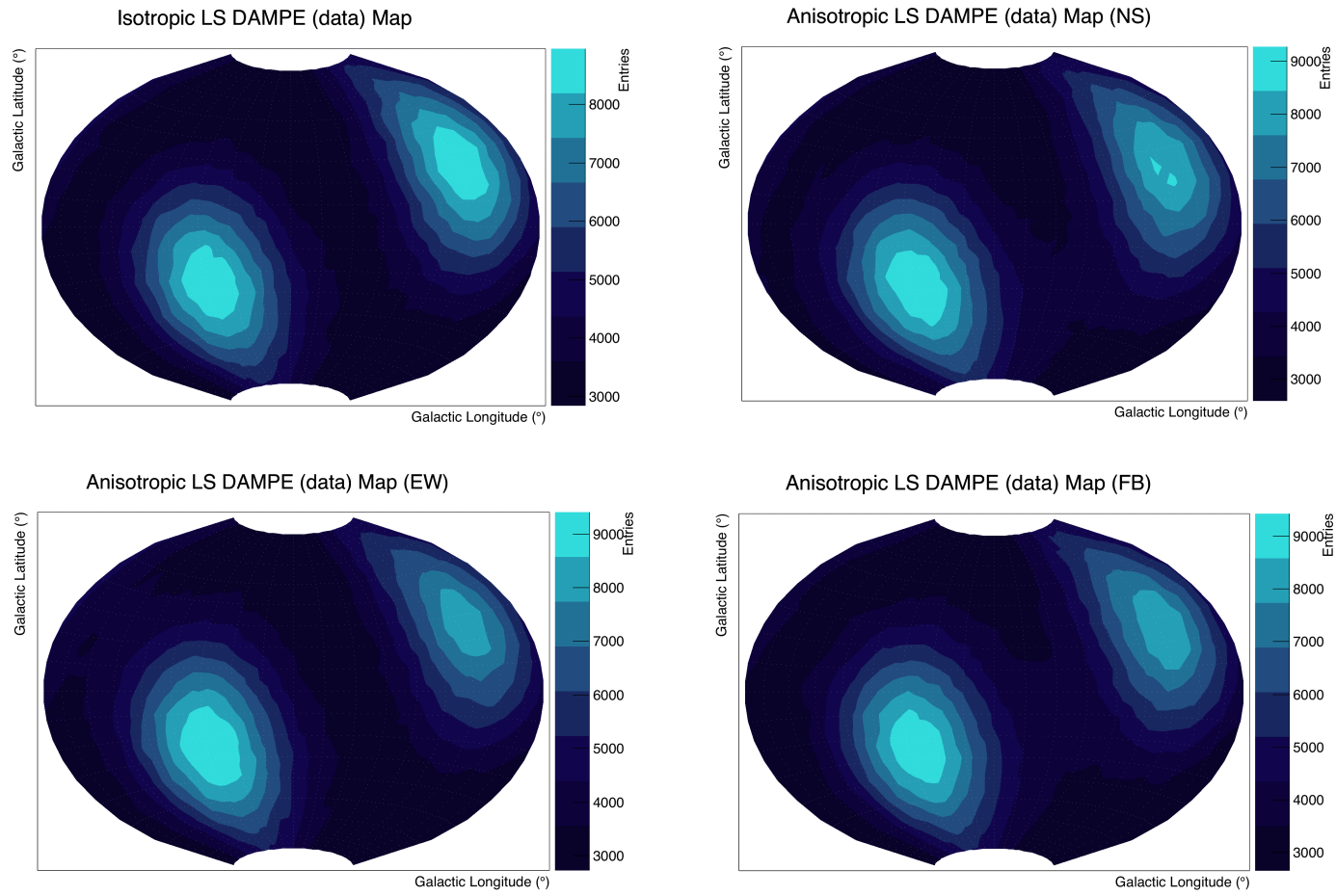


Figure G.7: *DAMPE's* simulated data maps, 10% anisotropy injected

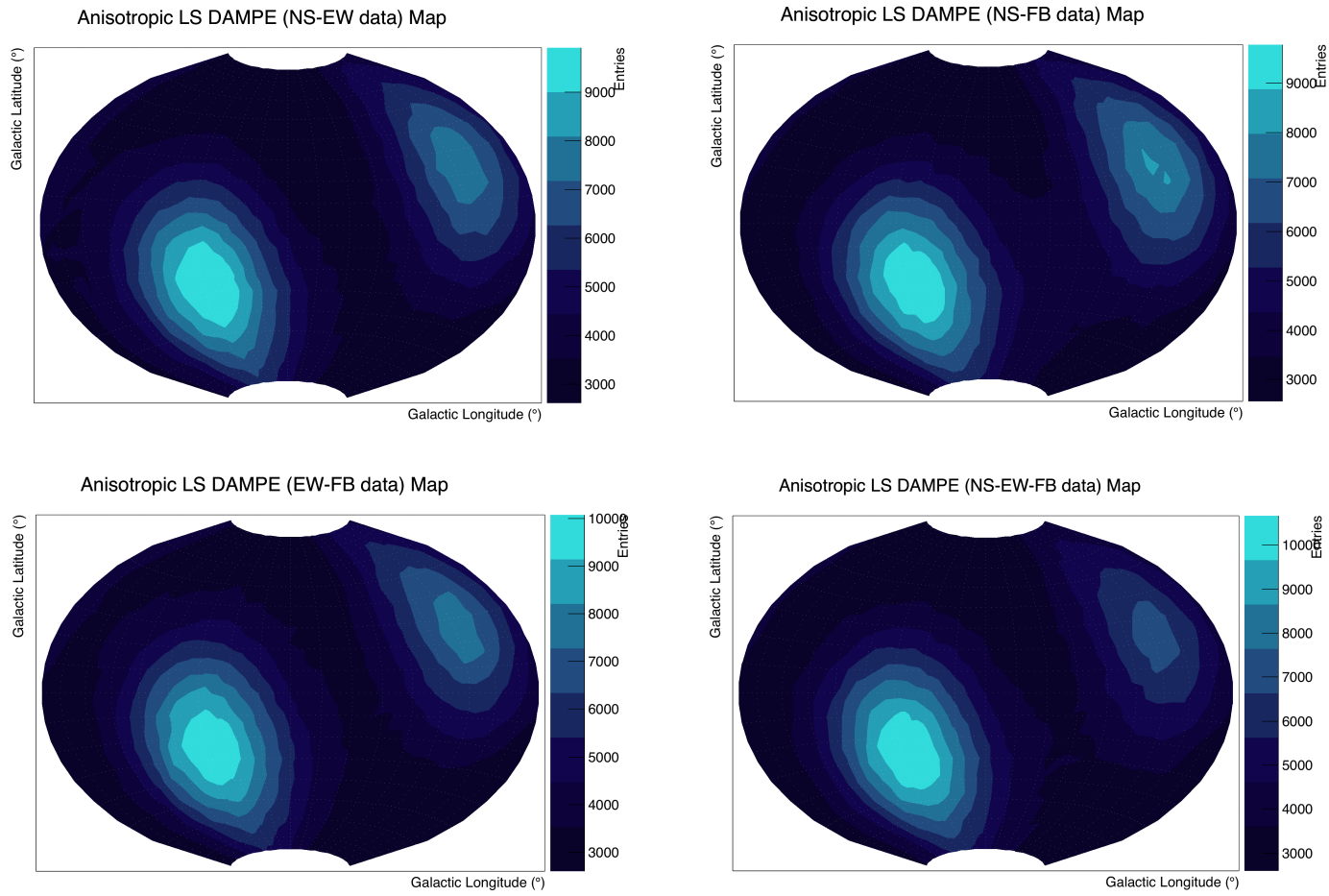


Figure G.8: *DAMPE*'s simulated data maps, 10% anisotropy injected

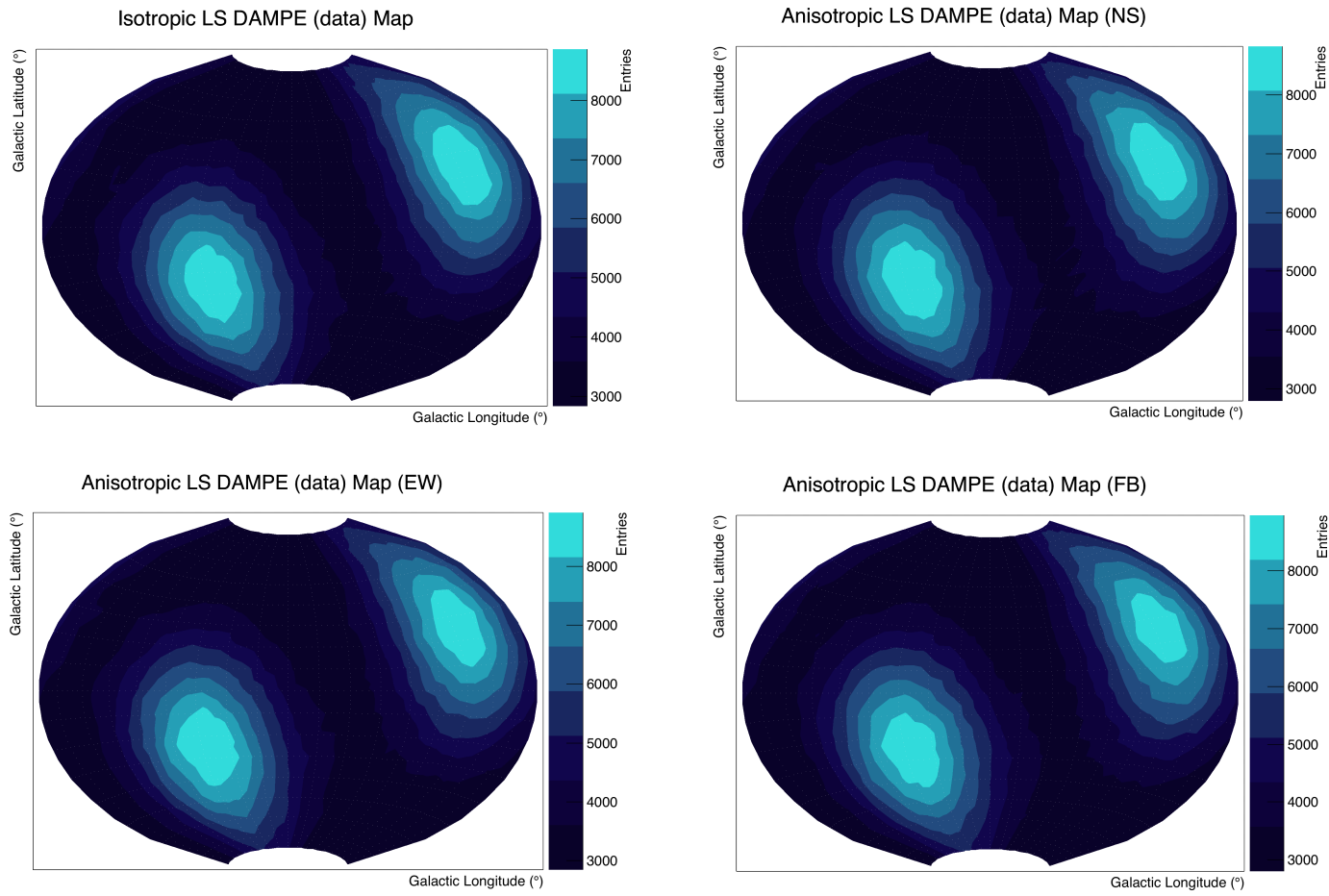


Figure G.9: *DAMPE*'s simulated data maps, 1% anisotropy injected

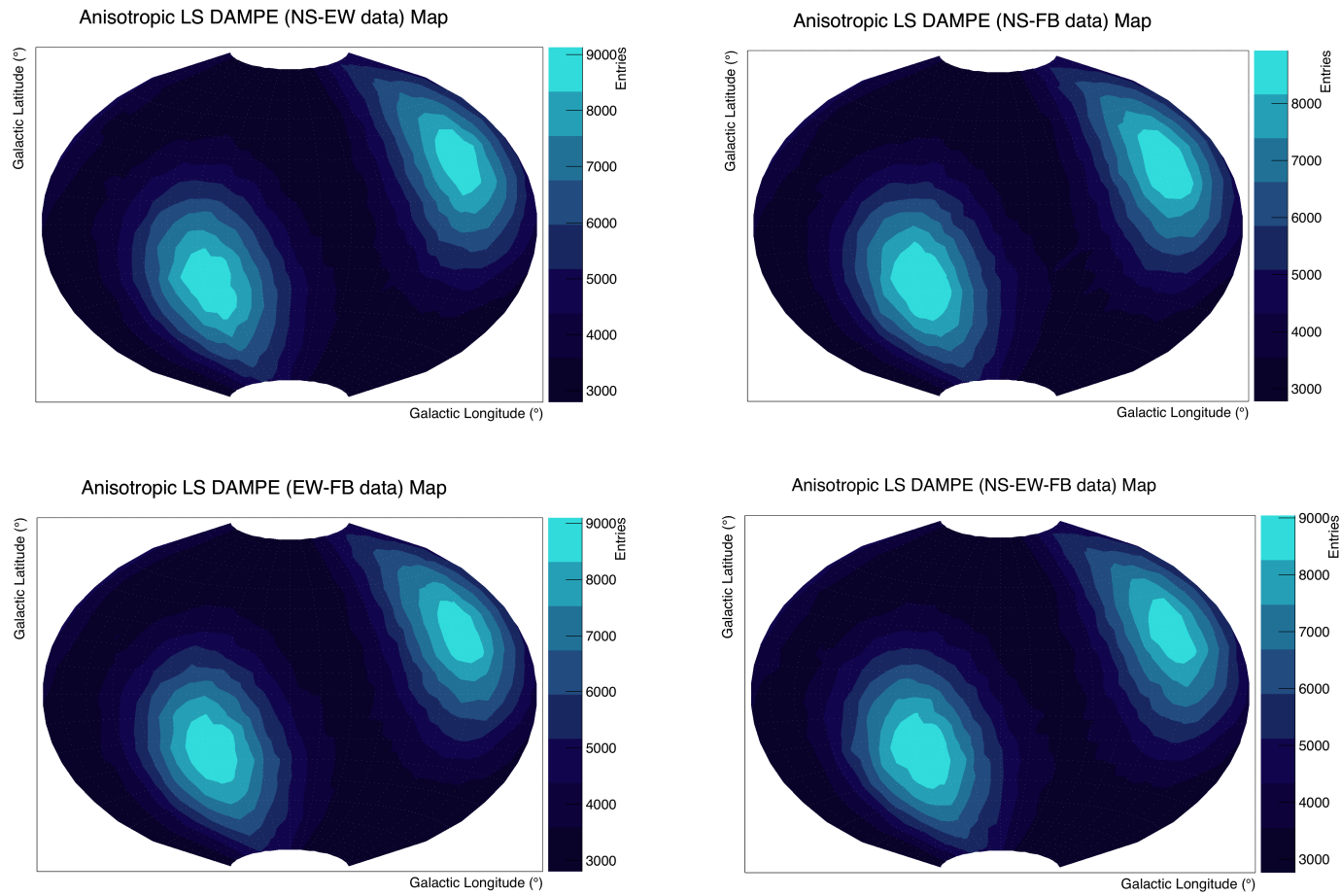


Figure G.10: *DAMPE's* simulated data maps, 1% anisotropy injected

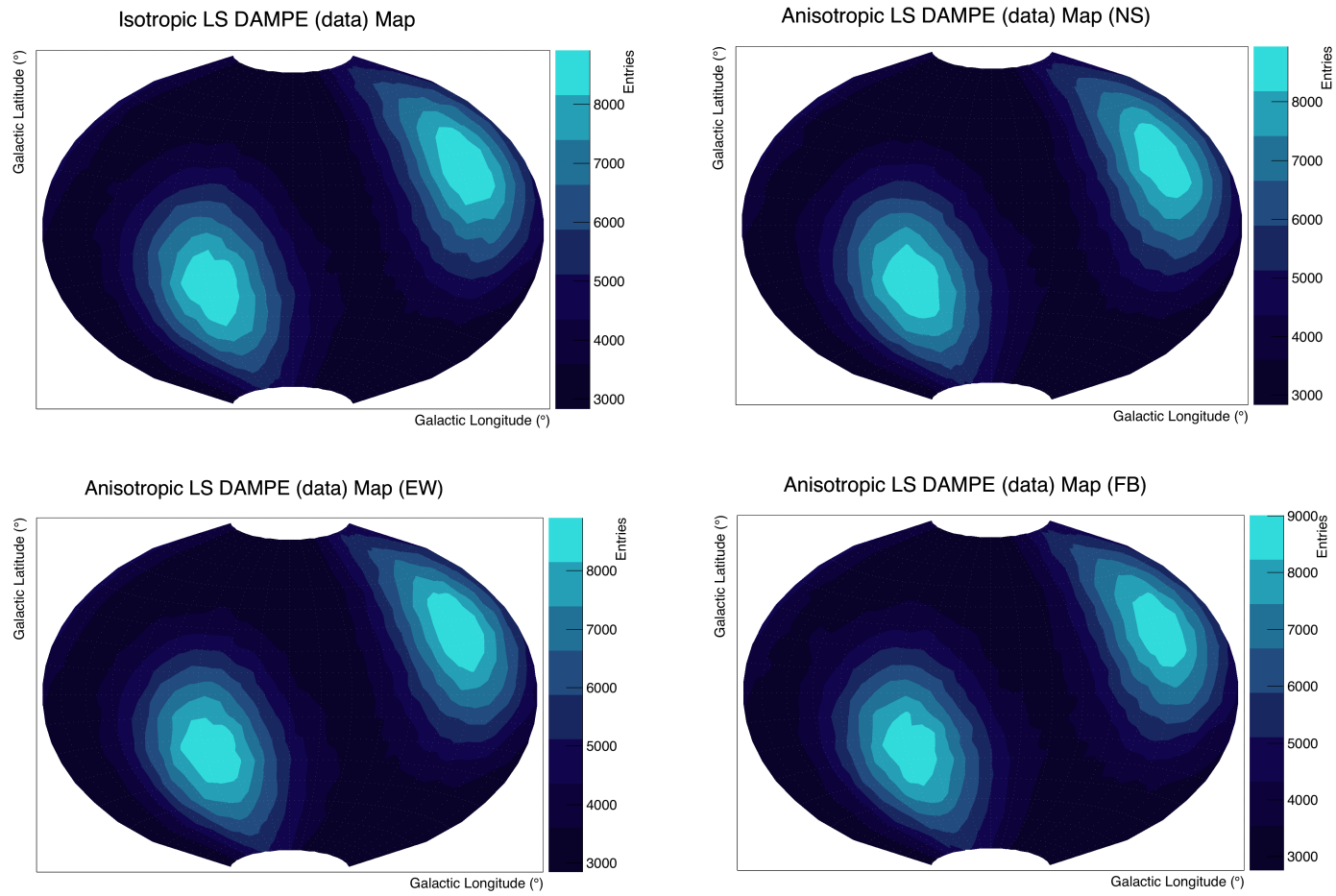


Figure G.11: *DAMPE*'s simulated data maps, 1‰ anisotropy injected

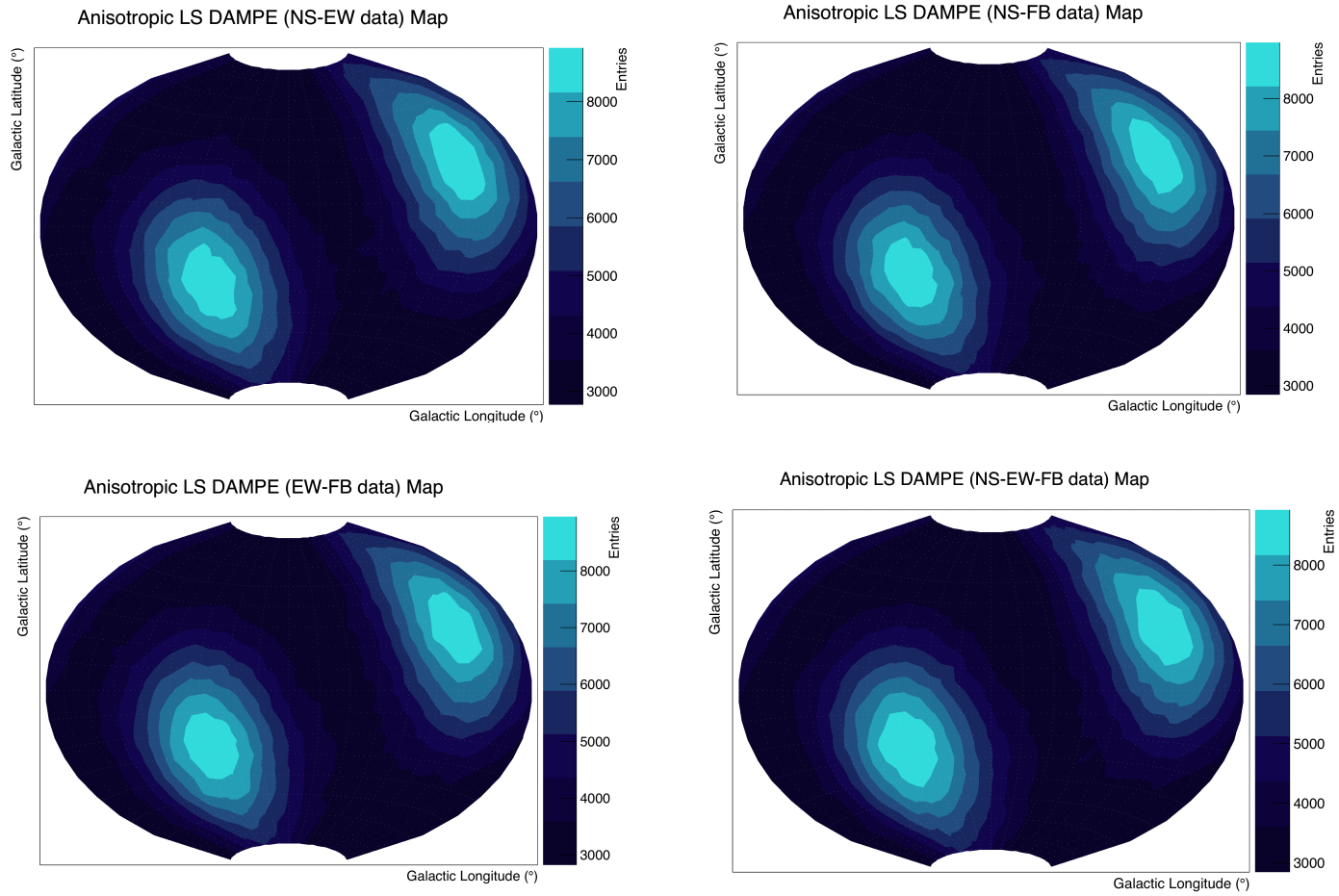


Figure G.12: *DAMPE*'s simulated data maps, 1‰ anisotropy injected

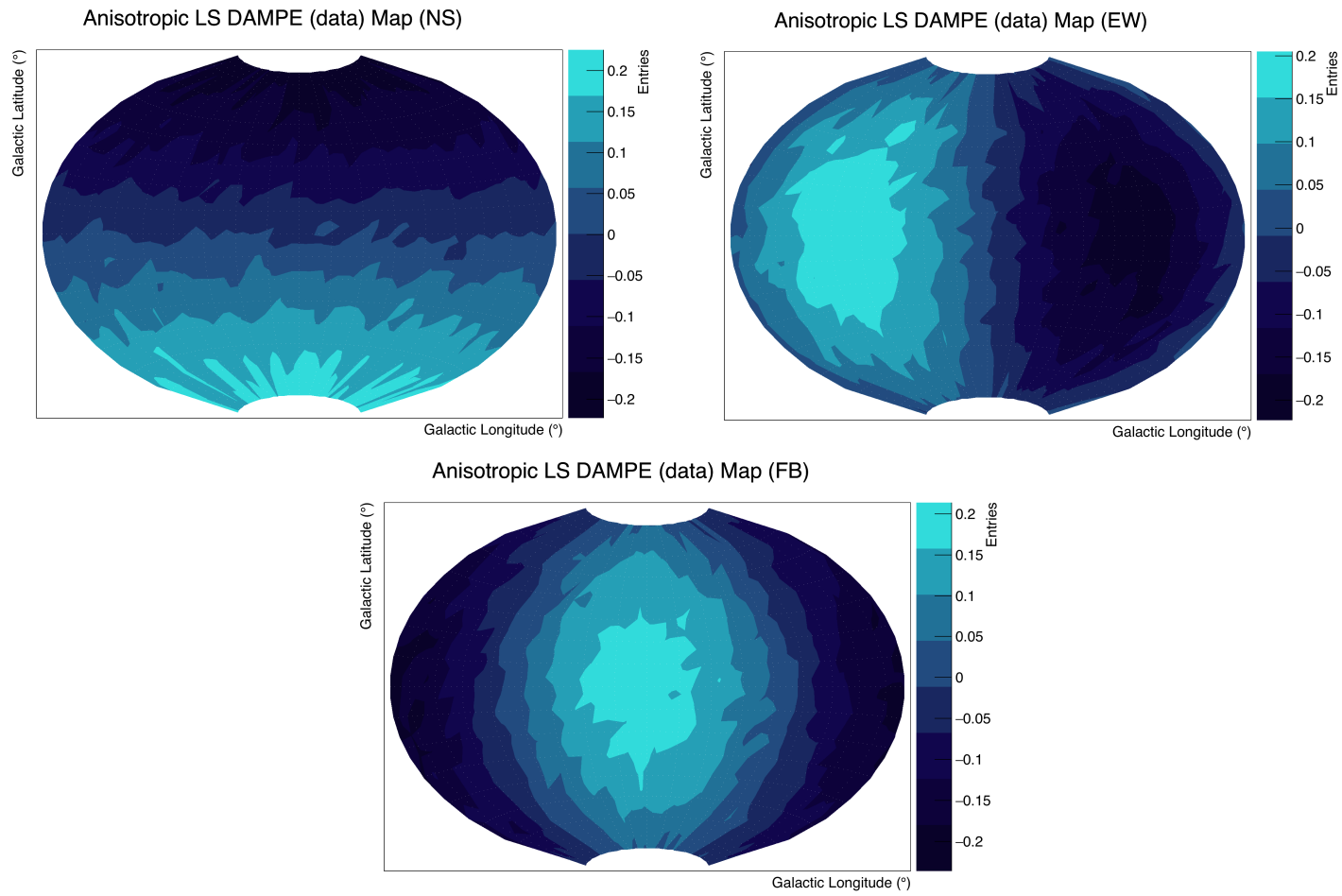


Figure G.13: *DAMPE's* simulated relative data maps, 10% anisotropy injected

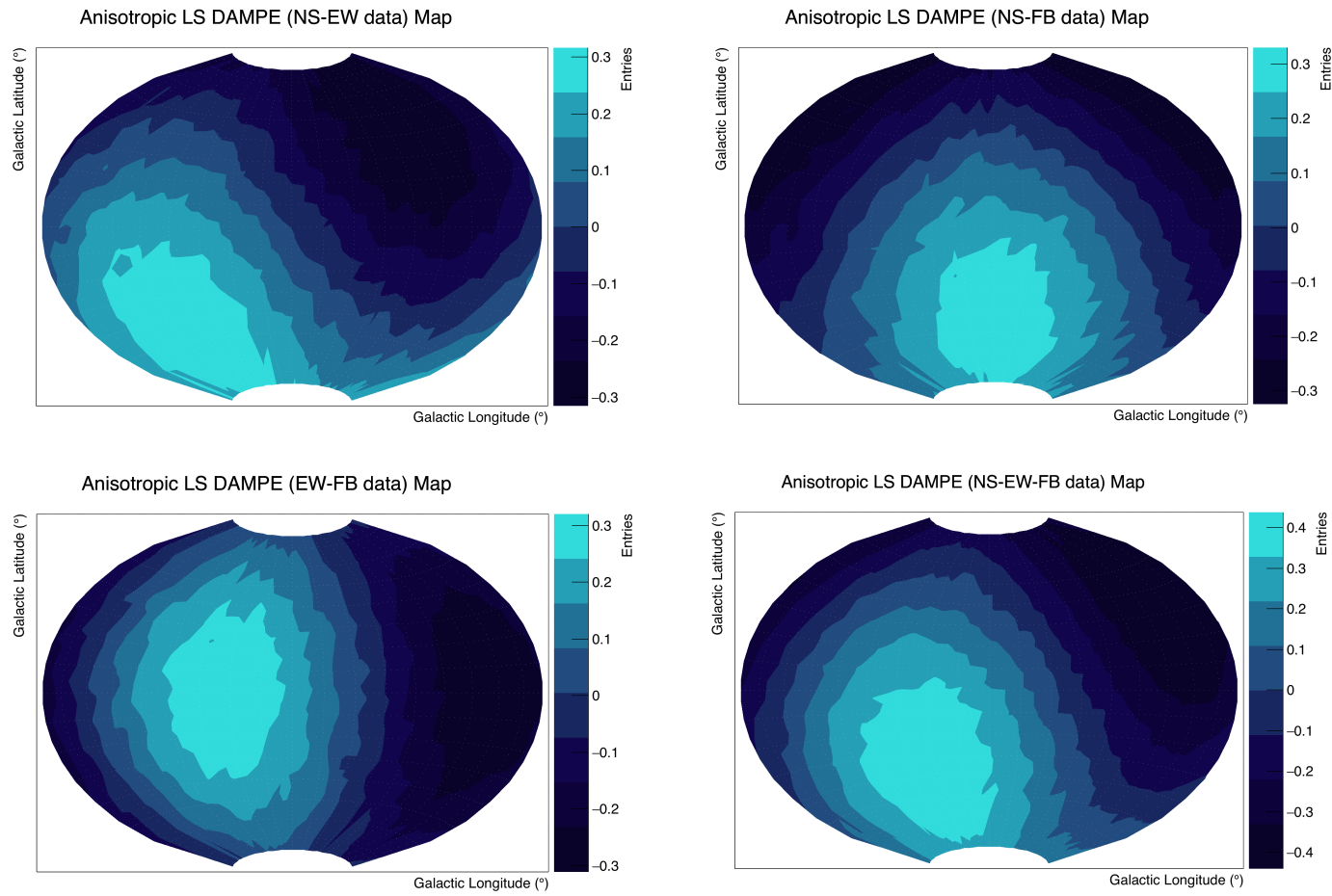


Figure G.14: *DAMPE*'s simulated relative data maps, 10% anisotropy injected

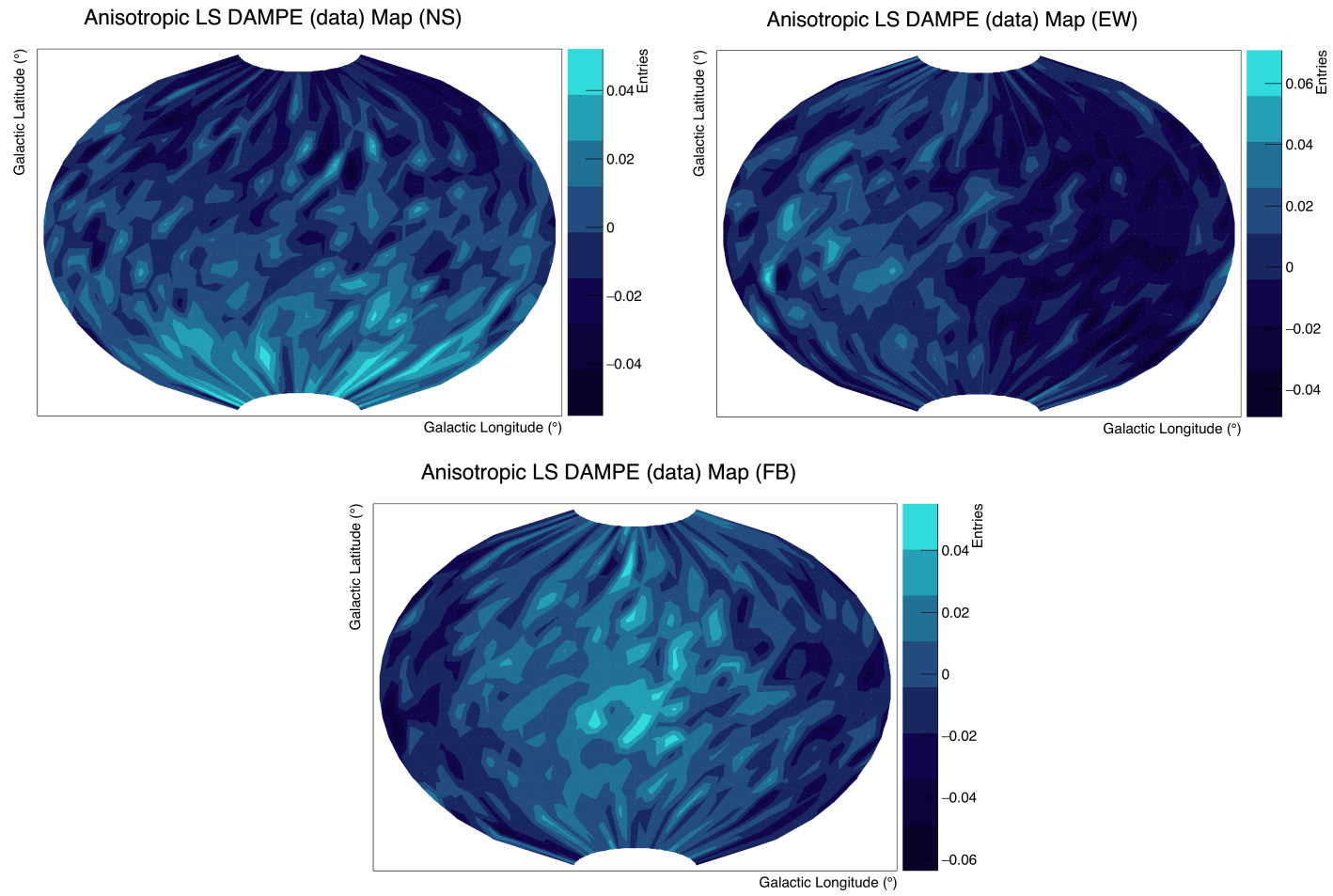


Figure G.15: *DAMPE's* simulated relative data maps, 1% anisotropy injected

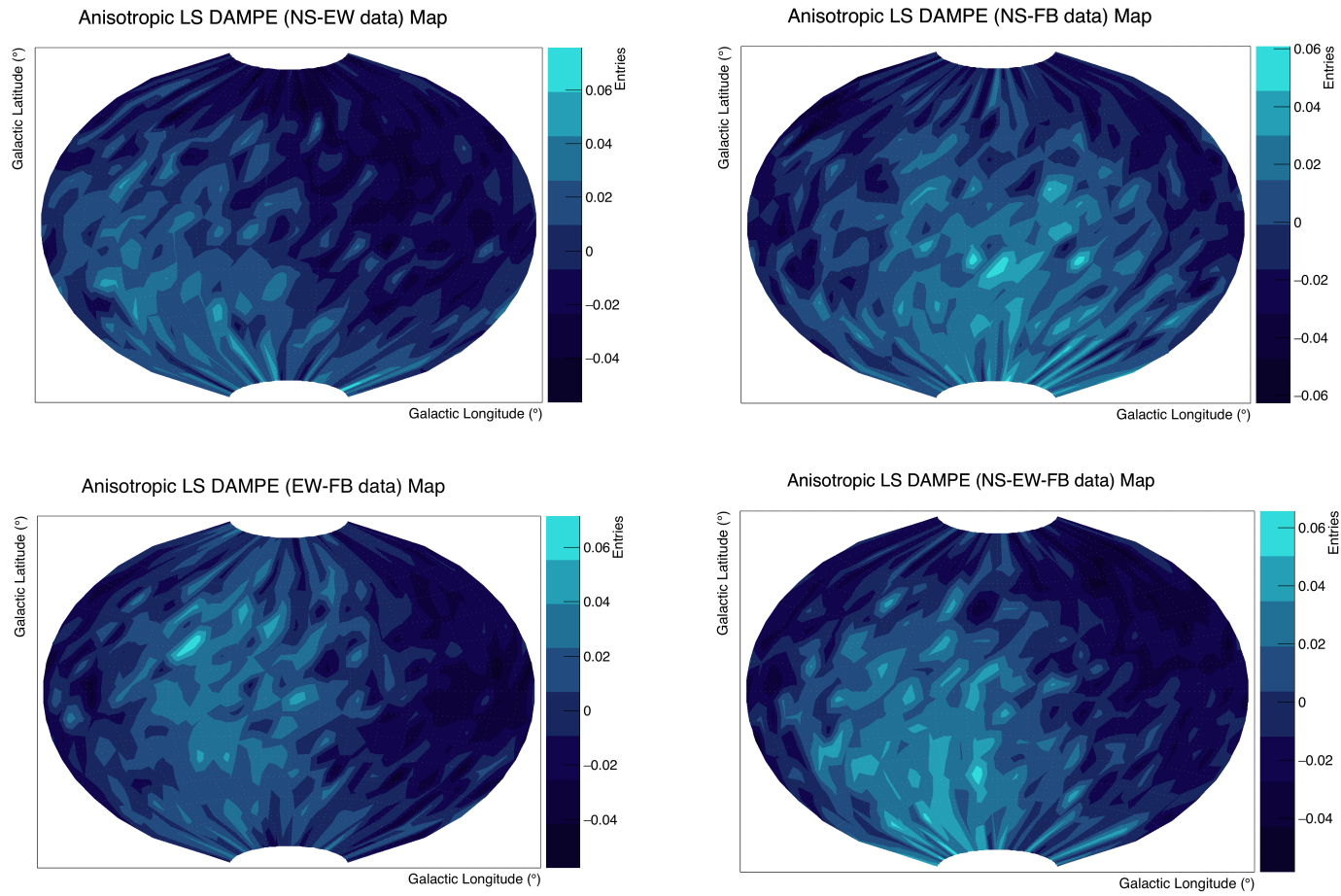


Figure G.16: *DAMPE*'s simulated relative data maps, 1% anisotropy injected

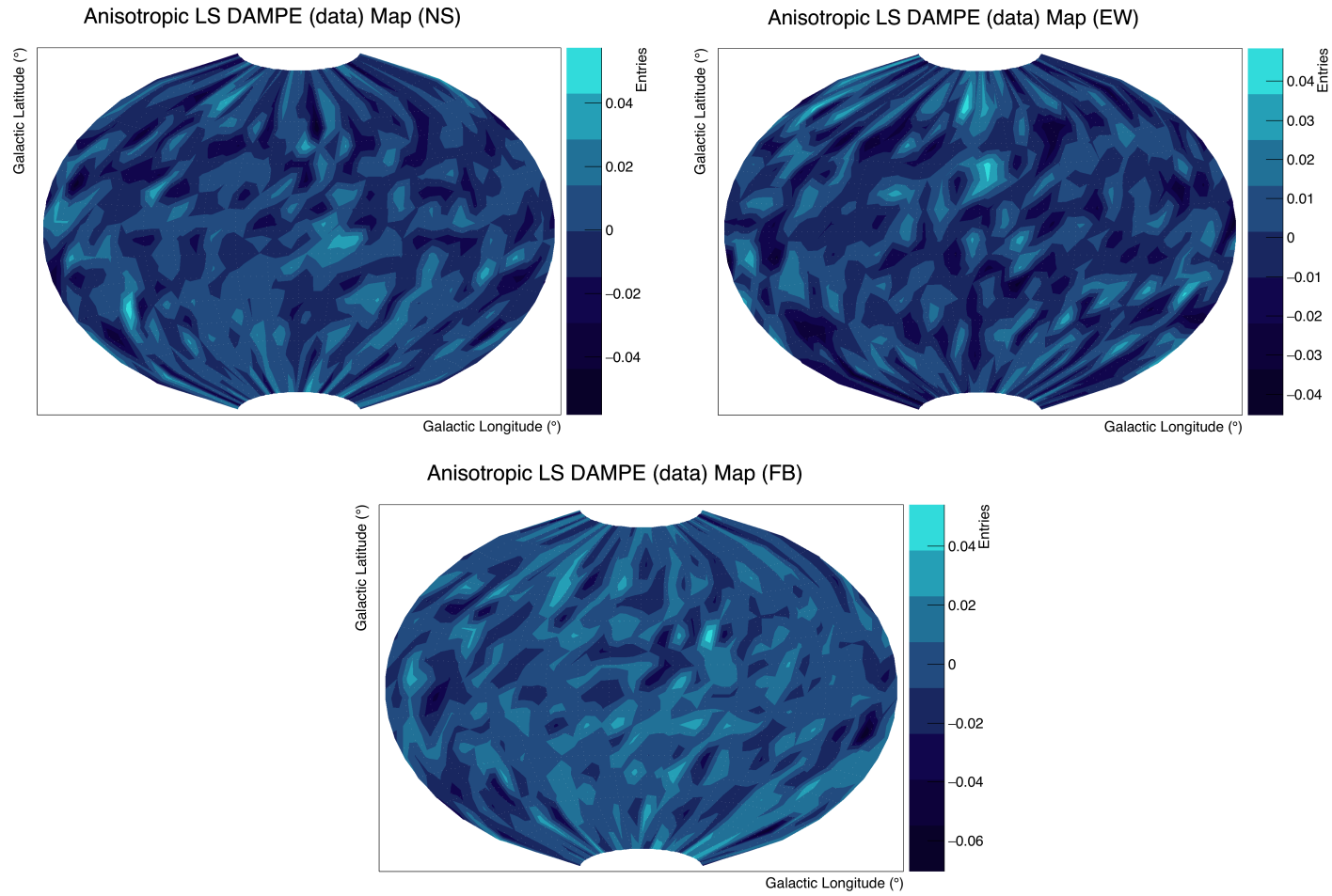


Figure G.17: *DAMPE*'s simulated relative data maps, 1‰ anisotropy injected

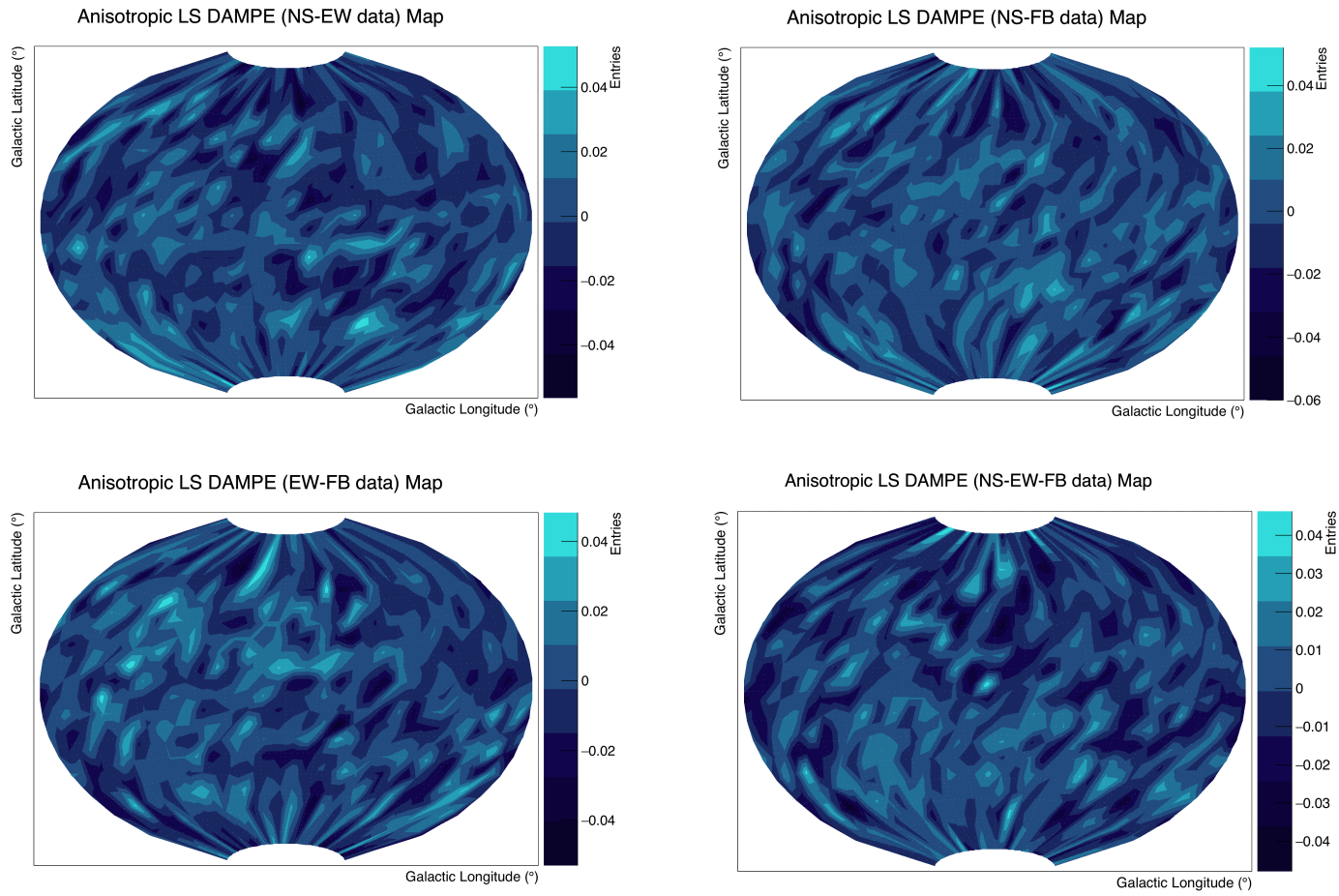


Figure G.18: *DAMPE*'s simulated relative data maps, 1‰ anisotropy injected

Bibliography

- [1] D. Schuckardt, *Limits on the dipole anisotropy in the flux of cosmic ray leptons with AMS-02*. PhD thesis, Institute for Experimental Nuclear Physics (IEKP), 2014.
- [2] M. Settimo, “Studio dei meccanismi di accelerazione dei raggi cosmici di alta energia,” Master’s thesis, Università degli Studi di Lecce, 2004.
- [3] M. S. Longair, *High Energy Astrophysics*, vol. 2. Cambridge University Press, 2 ed., 1994.
- [4] M. Ackermann, M. Ajello, W. B. Atwood, L. Baldini, J. Ballet, G. Barbiellini, D. Bastieri, K. Bechtol, R. Bellazzini, B. Berenji, and et al., “Searches for cosmic-ray electron anisotropies with the fermi large area telescope,” *Physical Review D*, vol. 82, Nov 2010.
- [5] M. Aguilar *et al.*, “First Result from the Alpha Magnetic Spectrometer on the International Space Station: Precision Measurement of the Positron Fraction in Primary Cosmic Rays of 0.5350 GeV,” *Phys. Rev. Lett.*, vol. 110, p. 141102, 2013.
- [6] S. Caroff, “High Statistics Measurement of the Positron Fraction in Primary Cosmic Rays with the Alpha Magnetic Spectrometer on the International Space Station,” in *25th European Cosmic Ray Symposium (ECRS 2016) Turin, Italy, September 04-09, 2016*, 2016.
- [7] D. Collaboration, G. Ambrosi, Q. An, R. Asfandiyarov, P. Azzarello, P. Bernardini, B. Bertucci, M. S. Cai, J. Chang, D. Y. Chen, H. F. Chen, J. L. Chen, W. Chen, M. Y. Cui, T. S. Cui, A. D’Amone, A. De Benedittis, I. De Mitri, M. Di Santo, J. N. Dong, T. K. Dong, Y. F. Dong, Z. X. Dong, G. Donvito, D. Droz, K. K. Duan, J. L. Duan, M. Duranti, D. D’Urso, R. R. Fan, Y. Z. Fan, F. Fang, C. Q. Feng, L. Feng,

- P. Fusco, V. Gallo, F. J. Gan, M. Gao, S. S. Gao, F. Gargano, S. Garrappa, K. Gong, Y. Z. Gong, D. Y. Guo, J. H. Guo, Y. M. Hu, G. S. Huang, Y. Y. Huang, M. Ionica, D. Jiang, W. Jiang, X. Jin, J. Kong, S. J. Lei, S. Li, X. Li, W. L. Li, Y. Li, Y. F. Liang, Y. M. Liang, N. H. Liao, H. Liu, J. Liu, S. B. Liu, W. Q. Liu, Y. Liu, F. Loparco, M. Ma, P. X. Ma, S. Y. Ma, T. Ma, X. Q. Ma, X. Y. Ma, G. Marsella, M. N. Mazziotta, D. Mo, X. Y. Niu, X. Y. Peng, W. X. Peng, R. Qiao, J. N. Rao, M. M. Salinas, G. Z. Shang, W. H. Shen, Z. Q. Shen, Z. T. Shen, J. X. Song, H. Su, M. Su, Z. Y. Sun, A. Surdo, X. J. Teng, X. B. Tian, A. Tykhonov, V. Vagelli, S. Vitillo, C. Wang, H. Wang, H. Y. Wang, J. Z. Wang, L. G. Wang, Q. Wang, S. Wang, X. H. Wang, X. L. Wang, Y. F. Wang, Y. P. Wang, Y. Z. Wang, S. C. Wen, Z. M. Wang, D. M. Wei, J. J. Wei, Y. F. Wei, D. Wu, J. Wu, L. B. Wu, S. S. Wu, X. Wu, K. Xi, Z. Q. Xia, Y. L. Xin, H. T. Xu, Z. L. Xu, Z. Z. Xu, G. F. Xue, H. B. Yang, P. Yang, Y. Q. Yang, Z. L. Yang, H. J. Yao, Y. H. Yu, Q. Yuan, C. Yue, J. J. Zang, C. Zhang, D. L. Zhang, F. Zhang, J. B. Zhang, J. Y. Zhang, J. Z. Zhang, L. Zhang, P. F. Zhang, S. X. Zhang, W. Z. Zhang, Y. Zhang, Y. J. Zhang, Y. Q. Zhang, Y. L. Zhang, Y. P. Zhang, Z. Zhang, Z. Y. Zhang, H. Zhao, H. Y. Zhao, X. F. Zhao, C. Y. Zhou, Y. Zhou, X. Zhu, Y. Zhu, and S. Zimmer, “Direct detection of a break in the teraelectronvolt cosmic-ray spectrum of electrons and positrons,” *Nature*, vol. 552, pp. 63 EP –, 11 2017.
- [8] Y. hua Yao, C. Jin, and X. chuan Chang, “Test of the 1.4 tev dampe electron excess with preliminary h.e.s.s. measurement,” *Nuclear Physics B*, vol. 934, pp. 396 – 407, 2018.
- [9] A. Archer *et al.*, “Measurement of Cosmic-ray Electrons at TeV Energies by VERITAS,” 2018.
- [10] K. Fang, X.-J. Bi, and P.-F. Yin, “Explanation of the knee-like feature in the dampe cosmic $e^- + e^+$ energy spectrum,” *The Astrophysical Journal*, vol. 854, p. 57, Feb 2018.
- [11] J. Lavalle, “Galactic electrons and positrons at the earth: New estimate of the primary and secondary fluxes,” in *Cosmic Rays for Particle and Astroparticle Physics - Proceedings of the 12th ICATPP Conference*, pp. 525–534, 06 2011.

- [12] F. Donato, “Antimatter and lepton in space: multi-disciplinary, multi-wavelength directions,” in *AMS Days*, 2018.
- [13] M. Di Mauro, S. Manconi, A. Vittino, F. Donato, N. Fornengo, L. Baldini, R. Bonino, N. Di Lalla, L. Latronico, S. Maldera, and et al., “Theoretical interpretation of pass 8 fermi-lat e^+e^- data,” *The Astrophysical Journal*, vol. 845, p. 107, Aug 2017.
- [14] D. Hooper, P. Blasi, and P. D. Serpico, “Pulsars as the sources of high energy cosmic ray positrons,” *Journal of Cosmology and Astroparticle Physics*, vol. 2009, pp. 025–025, Jan 2009.
- [15] M. Cirelli, “Status of Indirect (and Direct) Dark Matter searches,” 2015.
- [16] D. Campana, U. Giaccari, O. Adriani, G. C. Barbarino, G. A. Bazilevskaya, R. Bellotti, A. Bianco, M. Boezio, E. A. Bogomolov, L. Bonechi, M. Bongi, V. Bonvicini, S. Borisov, S. Bottai, A. Bruno, F. Cafagna, R. Carbone, P. Carlson, M. Casolino, G. Castellini, M. P. D. Pascale, C. D. Santis, N. D. Simone, V. D. Felice, V. Formato, A. M. Galper, L. Grishantseva, G. Jerse, A. V. Karelin, M. D. Kheymits, S. V. Koldashov, S. Y. Krutkov, A. N. Kvashnin, A. Leonov, V. Malakhov, V. Malvezzi, L. Marcelli, M. Martucci, A. G. Mayorov, W. Menn, V. V. Mikhailov, E. Mocchiutti, A. Monaco, N. Mori, R. Munini, N. Nikonov, G. Osteria, F. Palma, P. Papini, M. Pearce, P. Picozza, C. Pizzolotto, M. Ricci, S. B. Ricciarini, L. Rossetto, R. Sarkar, M. Simon, R. Sparvoli, P. Spillantini, Y. I. Stozhkov, A. Vacchi, E. Vannuccini, G. Vasilyev, S. A. Voronov, J. Wu, Y. T. Yurkin, G. Zampa, N. Zampa, and V. G. Zverev, “Search for cosmic ray electron-positron anisotropies with the pamel data,” *Journal of Physics: Conference Series*, vol. 409, no. 1, p. 012055, 2013.
- [17] I. Gebauer, “Methods for cosmic ray anisotropy searches with AMS-02,” *PoS*, vol. ICRC2015, p. 408, 2016.
- [18] G. La Vacca, “Search for Cosmic Ray Anisotropy with the Alpha Magnetic Spectrometer on the International Space Station,” in *25th European Cosmic Ray Symposium (ECRS 2016) Turin, Italy, September 04-09, 2016*, 2016.

- [19] S. Abdollahi, M. Ackermann, M. Ajello, A. Albert, W. B. Atwood, L. Baldini, G. Barbiellini, R. Bellazzini, E. Bissaldi, E. D. Bloom, and et al., “Search for cosmic-ray electron and positron anisotropies with seven years of fermi large area telescope data,” *Physical Review Letters*, vol. 118, Mar 2017.
- [20] S. Manconi, M. D. Mauro, and F. Donato, “Dipole anisotropy in cosmic electrons and positrons: inspection on local sources,” *Journal of Cosmology and Astroparticle Physics*, vol. 2017, pp. 006–006, Jan 2017.
- [21] J. Chang, G. Ambrosi, Q. An, R. Asfandiyarov, P. Azzarello, P. Bernardini, B. Bertucci, M. Cai, M. Caragiulo, D. Chen, and et al., “The dark matter particle explorer mission,” *Astroparticle Physics*, vol. 95, pp. 6–24, Oct 2017.
- [22] J. Sullivan, “Geometric factor and directional response of single and multi-element particle telescopes,” *Nuclear Instruments and Methods*, vol. 95, no. 1, pp. 5 – 11, 1971.
- [23] A. Cuoco, T. Linden, M. Mazziotta, J. Siegal-Gaskins, V. Vitale, and E. Komatsu, “Anisotropies in the diffuse gamma-ray background measured by the fermi-lat,” *Nuclear Instruments and Methods in Physics Research Section A: Accelerators, Spectrometers, Detectors and Associated Equipment*, vol. 692, pp. 127–131, Nov 2012.
- [24] K. M. Gorski, B. D. Wandelt, F. K. Hansen, E. Hivon, and A. J. Banday, “The healpix primer,” 1999.
- [25] S. N. Zhang, O. Adriani, S. Albergo, G. Ambrosi, Q. An, T. W. Bao, R. Battiston, X. J. Bi, Z. Cao, J. Y. Chai, and et al., “The high energy cosmic-radiation detection (herd) facility onboard china’s space station,” *Space Telescopes and Instrumentation 2014: Ultraviolet to Gamma Ray*, Jul 2014.

Acknowledgements

First of all my thanks to my tutors, Dr. Valerio Vagelli and Dr. Matteo Duranti, that made this work possible. Their passion and devotion on this project, together with their ability, patience and precious advice allowed to make this work something special.

A special thanks to Dr. Giovanni Ambrosi, for his continuous support during the various stages of this project.

Last, but not least, a great thank you to my special friends Gabriele di Bari and Mirco Tracoli, Ph.D. students in computer science at the University of Florence and Perugia, for their precious and essential help in the realization and improvement of the data analysis software.